NASA TECHNICAL REPORT

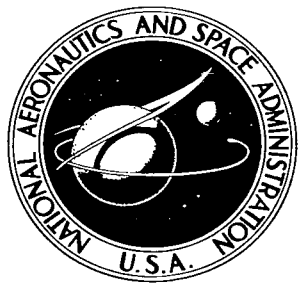

NASA TR R-223

NASA TR R-223

A PERFECT-GAS ANALYSIS OF THE EXPANSION TUNNEL, A MODIFICATION TO THE EXPANSION TUBE

by Robert L. Trimpi and Linwood B. Callis

Langley Research Center
Langley Station, Hampton, Va.

NATIONAL AERONAUTICS AND SPACE ADMINISTRATION • WASHINGTON, D. C. • APRIL 1965

A PERFECT-GAS ANALYSIS OF THE EXPANSION TUNNEL, A MODIFICATION TO THE EXPANSION TUBE

By Robert L. Trimpi and Linwood B. Callis

Langley Research Center
Langley Station, Hampton, Va.

NATIONAL AERONAUTICS AND SPACE ADMINISTRATION

For sale by the Office of Technical Services, Department of Commerce,
Washington, D.C. 20230 -- Price $4.00

CONTENTS

A PERFECT-GAS ANALYSIS OF THE EXPANSION TUNNEL, A MODIFICATION TO THE EXPANSION TUBE

By Robert L. Trimpi and Linwood B. Callis
Langley Research Center

SUMMARY

A perfect-gas analysis is presented for an apparatus consisting of a basic expansion tube at the downstream end of which a nozzle has been added. The resultant apparatus, named the expansion tunnel, is shown to have the following advantages when compared with the basic expansion tube: increased testing time, larger initial test-gas slug length, higher efficiency, and reduced secondary-diaphragm bursting problems. Principal disadvantages are requirement of an additional nozzle, and the requirement of a larger ratio between maximum and minimum pressures in an operating cycle. Authors conclude inherent advantages more than compensate for disadvantages.

INTRODUCTION

For the past few years scientists at the Langley Research Center have been investigating various modifications to the basic expansion tube described in reference 1. Effort has been concentrated on those variations which were more directly aimed at alleviation of the anticipated principal undesirable features of the expansion tube; namely, the short initial length of the test-gas slug before diaphragm rupture, the bursting of the secondary diaphragm, and the short test time. Both experimental and theoretical investigations have been conducted, and the latter include considerations of several modifications for both real and perfect gases. Most of the experimental results obtained to date in the pilot expansion tube at the Langley Research Center (unpublished) are for expansion-tube operation; these results appear encouraging.

This report will describe the perfect-gas analysis of the configuration that the authors believe holds the most promise for reducing the aforementioned drawbacks. This configuration, mentioned in references 1 and 2, is called an expansion tunnel and consists of a basic expansion tube to which at the downstream end a nozzle has been added. (See fig. 1.) Thus the test fluid is processed first by an unsteady expansion in the accelerating chamber and then by a steady expansion in the nozzle. A group at the Von Karman Laboratory of the Arnold Engineering Development Center has also been investigating both theoretically and experimentally a different configuration which has a nozzle located just after the secondary diaphragm. For such a configuration the fluid

is processed first by a steady expansion and subsequently by an unsteady expansion if the accelerating chamber is several orders of magnitude longer than the nozzle. If these length restrictions are not satisfied, the test gas is processed simultaneously by both steady and unsteady expansion waves with the result that the gas state at the test section continually varies with time. The relative prior occurrence of the unsteady expansion as compared with the steady expansion has an extremely important bearing on the subsequent characteristics of the apparatus. Consequently, even though both modifications contain nozzles, their operation and performances are very different.

The analysis herein is restricted to the perfect-gas assumption which permits the pertinent equations to be expressed in closed form. Such equations are valuable since important trends and influences can often be simply extracted and examined critically. A somewhat parallel real-gas analysis (unpublished to date) has also been executed. The real-gas analysis verifies the perfect-gas trends of this paper although the magnitudes of the variations naturally are not identical.

For the convenience of the reader an index to the figures is presented as table I.

SYMBOLS

A	quasi-one-dimensional-flow area
$\bar{A} = \frac{A_f}{A_e}$	
$\bar{A}_{geom}$	geometric nozzle area ratio measured normal (perpendicular) to axis
a	speed of sound
$C = \frac{d\bar{A}}{d\xi}$ $C' = \frac{d\bar{A}}{d\xi}$	for linear area nozzle and conical nozzle, respectively
c_v	driver-gas specific heat at constant volume
D	test-section (nozzle exit) diameter
d	accelerating-chamber diameter
d'	nozzle entrance diameter
E	driver-chamber energy (eq. (72))
$\bar{E}$	driver-chamber energy parameter

e	gas state before nozzle (fig. 1)
F	ratio of nozzle losses for linear radius and linear area nozzles (eq. (62))
f	gas state in test section
G, G_o, G^*	parameters defined in eqs. (79)
g	gas state (fig. 10)
H	total enthalpy
I_n, J_n	functions defined in eqs. (43) and (56)
i	initial state of driver gas before arc discharge
K_1, K_2	constants defined in eqs. (44) and (57)
$l_D, l_{S_1}, l_{S_2}, l_N, l_{S_R}$	lengths of driver, intermediate chamber, accelerating chamber, nozzle, and dump-tank sections of expansion tunnel (see fig. 1)
l_S	length of expansion chamber in shock tunnel
M	flow Mach number
M_f	test-section Mach number
M_{S_1}	primary-shock Mach number, U_{S_1}/a_1
m,n	points on wave diagram (fig. 1)
n	integer
P	Riemann parameter (eq. (9))
p	static pressure
$N_{Re,D}, N_{Re,d}$	Reynolds number based on test-section and accelerating-chamber diameters
T	absolute temperature
t	time
$\Delta t( )$	time increments (see figs. 1 and 13)
U_{S_1}	velocity of primary shock wave

$U_{S_{11}}$ velocity of secondary shock wave

$U_{S_{10}}$ velocity of tertiary shock wave

U_{S_R} velocity of reflected shock wave

u flow velocity

x distance in flow direction

z initial length of test gas slug in intermediate chamber (eq. (67))

$$\beta = \frac{\Omega(M_e)}{\Omega(M_f)}$$

$$\Gamma_1(M) = 1 + \frac{\gamma - 1}{2} M$$

$$\Gamma_2(M) = 1 + \frac{\gamma - 1}{2} M^2$$

γ ratio of specific heats

δ boundary-layer thickness

η overall efficiency, $\eta_o \eta_{l_N} \eta_{d'}$

η_o ideal efficiency

η_{l_N} nozzle time loss efficiency

$\eta_{d'}$ nozzle capture efficiency

θ flow angle

θ_w wall angle

μ viscosity

ξ nozzle coordinate in flow direction

ρ density

$$\Omega(M) = \Gamma_1(M)\left[\Gamma_2(M)\right]^{-1/2}$$

ω exponent in viscosity-temperature relation

Additional remarks regarding notation:

ⓘ denotes gas in state i in cycle

$( )_i$ subscript signifies quantity is to be evaluated in ith state

$( )_{ETun}$, $( )_{ET}$, $( )_{NRS}$ refers to expansion tunnel, expansion tube, or nonreflected shock tunnel, respectively

$( )^*$ refers to critical conditions when $\Delta t_{test} = 0$ (that is, nozzle time losses equal to Δt_2)

THEORY

A description of the expansion-tunnel components and operation is more easily explained with reference to figure 1 which shows a schematic of the tunnel and a distance-time or wave diagram of the operating cycle. The tunnel has five basic sections: driver chamber, intermediate chamber, accelerating chamber, nozzle, and dump tank. Three diaphragms separate the first four preceding sections. Thus, the expansion tunnel is an expansion tube to which has been added another diaphragm and a nozzle. The test fluid, which is initially in the intermediate chamber, is processed first from state ① to state ② by the primary shock wave, next to the state ⓔ by the unsteady upstream expansion wave, and finally to the test state ⓕ by passage through the nozzle.

A perfect-gas theory is developed to illustrate the important facets of the expansion tunnel. The assumption of strong shock waves is used for all shock waves. Approximate equations are also often given in terms of test-section Mach number and area ratio for the asymptotic limiting cases of large nozzle exit and entrance Mach numbers. Each phase of the cycle is treated by considering in turn the processes of the gas initially in the intermediate chamber, accelerating chamber, driver chamber, and so forth. Readers not interested in details of the derivations, flow processes, and so forth, can proceed to the section on "Discussion" wherein the main points are considered.

Test-Gas Processes

The test-gas processes are found by working backwards from the desired test-section conditions ⓕ through the intermediate states ⓔ and ② to the initial charging state ①. The test-gas value of γ is implied when γ is

used without a subscript. All curves shown in this report are for a test gas with $\gamma = 1.4$.

The states ⓔ and ⓕ are related by the familiar isentropic quasi-one-dimensional steady-flow equations (see ref. 3):

$$\bar{A} \equiv \frac{A_f}{A_e} = \frac{M_e}{M_f}\left[\frac{\Gamma_2(M_f)}{\Gamma_2(M_e)}\right]^{\frac{\gamma+1}{2(\gamma-1)}} \tag{1}$$

$$\frac{a_e}{a_f} = \left[\frac{\Gamma_2(M_f)}{\Gamma_2(M_e)}\right]^{1/2} \tag{2}$$

$$\frac{u_e}{u_f} = \frac{M_e}{M_f}\frac{a_e}{a_f} \tag{3}$$

$$\frac{p_e}{p_f} = \left(\frac{a_e}{a_f}\right)^{\frac{2\gamma}{\gamma-1}} \tag{4}$$

The variation with test-section Mach number M_f of the nondimensional parameters on the left-hand side of equations (1) to (4) for the perfect test gas ($\gamma = 1.4$) is given in figures 2(a) to 2(d). The area ratio $\bar{A}$ varies from the basic expansion tube value of unity to 1000. The curves are terminated by a short dashed line at the lower Mach number end when the expansion fan has completely vanished ($M_e = M_2 = 1.89$) and the apparatus is then operating as a nonreflected shock tunnel. (Of course, in a nonreflected tunnel one would test in gas initially in the accelerating chamber rather than in the intermediate chamber.)

The asymptotic approximations for equations (1) to (4) are obtained by assuming $M_f^2 \gg \frac{2}{\gamma - 1}$ and $M_e^2 \gg \frac{2}{\gamma - 1}$. Then from equation (1)

$$\bar{A} \approx \left(\frac{M_f}{M_e}\right)^{\frac{2}{\gamma-1}} \tag{1a}$$

and from equations (2), (3), and (4)

$$\frac{a_e}{a_f} \approx \frac{M_f}{M_e} \approx (\bar{A})^{\frac{\gamma-1}{2}} \tag{2a}$$

$$\frac{u_e}{u_f} \approx \frac{M_e}{M_f}\frac{a_e}{a_f} \approx 1 \tag{3a}$$

$$\frac{p_e}{p_f} \approx (\bar{A})^{\gamma} \tag{4a}$$

These approximations are indicated at the higher values of M_f in figure 2. Note (fig. 2(b)) that for $M_f \gtrsim 20$, the exact values of $\frac{u_e}{u_f} \gtrsim 0.9$; therefore, only a small percentage increase in velocity occurs in the nozzle.

Since the process from ① → ② → ⓔ is simply the expansion tube process of reference 1, the equations of that reference are applicable to the test gas by substitution of state ⓔ for state ⑤. However, a brief outline of the necessary steps is as follows: The strong shock assumptions $\left(\frac{p_2}{p_1} \gg 1\right)$ require that

$$\frac{u_2}{a_1} \approx \sqrt{\frac{2}{\gamma(\gamma + 1)}\frac{p_2}{p_1}} \tag{5}$$

$$\frac{a_2}{a_1} \approx \sqrt{\frac{\gamma - 1}{\gamma + 1}\frac{p_2}{p_1}} \approx \sqrt{\frac{\gamma(\gamma - 1)}{2}}\frac{u_2}{a_1} \tag{6}$$

$$M_2 \approx \sqrt{\frac{2}{\gamma(\gamma - 1)}} \tag{7}$$

$$M_{S_1} \equiv \frac{U_{S_1}}{a_1} \approx \sqrt{\frac{\gamma + 1}{2\gamma}\frac{p_2}{p_1}} \approx \frac{\gamma + 1}{2}\frac{u_2}{a_1} \tag{8}$$

(Eqs. (5) to (8) are identical to eqs. (3) to (6) of ref. 1.) The value of M_2 is approximately 1.89 for $\gamma = 1.4$. The Riemann parameter P is constant across the upstream wave (eq. (7) of ref. 1); thus,

$$P = \frac{2}{\gamma - 1}a_2 + u_2 = \frac{2}{\gamma - 1}a_e + u_e \tag{9}$$

Consequently,

$$\frac{a_2}{a_e} = \frac{\Gamma_1(M_e)}{\Gamma_1(M_2)} \tag{10}$$

$$\frac{p_2}{p_e} = \left[\frac{\Gamma_1(M_e)}{\Gamma_1(M_2)}\right]^{\frac{2\gamma}{\gamma-1}} \tag{11}$$

Combining equations (2) and (4) with equations (10) and (11) yields

$$\frac{a_2}{a_f} = \frac{a_2}{a_e}\frac{a_e}{a_f} = \frac{\Gamma_1(M_f)}{\Gamma_1(M_2)}\beta \tag{12}$$

$$\frac{p_2}{p_f} = \left(\frac{a_2}{a_f}\right)^{\frac{2\gamma}{\gamma-1}} = \left[\frac{\Gamma_1(M_f)}{\Gamma_1(M_2)}\beta\right]^{\frac{2\gamma}{\gamma-1}} \tag{13}$$

where

$$\left.\begin{aligned} \beta &\equiv \frac{\Omega(M_e)}{\Omega(M_f)} \\ \Omega(M) &\equiv \frac{\Gamma_1(M)}{\sqrt{\Gamma_2(M)}} \end{aligned}\right\} \tag{14}$$

Other pertinent parameters in state ② are then

$$\frac{u_2}{u_f} = \frac{M_2}{M_f}\frac{a_2}{a_f} = \frac{M_2}{M_f}\frac{\Gamma_1(M_f)}{\Gamma_1(M_2)}\beta \tag{15}$$

$$\frac{H_f}{H_2} = \frac{H_e}{H_2} = \left[\frac{\Omega(M_2)}{\Omega(M_e)}\right]^2 = \left[\frac{\Omega(M_2)}{\Omega(M_f)}\right]^2 \frac{1}{\beta^2} \tag{16}$$

Plots of equations (12), (13), (15), and (16) appear in figure 3. The values of a_2, u_2, p_2, and H_2 all are increased as $\overline{A}$ is increased for a

fixed M_f. An approximate expression for β with the restrictions $M_f^2 \gg \frac{2}{\gamma - 1}$, $M_e^2 \gg \frac{2}{\gamma - 1}$, and for M_e of the order of $\frac{2}{\gamma - 1}$ is

$$\beta \approx \frac{\Gamma_1(M_f) - 1}{\Gamma_1(M_f)}\left[1 + \frac{2}{\gamma - 1}\frac{1}{M_f}(\bar{A})^{\frac{\gamma-1}{2}}\right] \tag{17a}$$

$$\beta \approx \frac{1}{\Gamma_1(M_f)}\left[\frac{\gamma - 1}{2} M_f + (\bar{A})^{\frac{\gamma-1}{2}}\right] \tag{17b}$$

$$\beta \approx 1 + \frac{(\bar{A})^{\frac{\gamma-1}{2}} - 1}{\Gamma_1(M_f)} \tag{17c}$$

Both exact equations (14) and approximate equation (17) values for β are plotted in figures 4(a) and 4(b). The value of β is increased by increasing $\bar{A}$ or decreasing M_f and approaches unity only for small A. However, at $M = 50$ and $\bar{A} = 10^3$, β is reduced to approximately $1\frac{1}{4}$. The importance of the parameter β lies in the fact that it directly relates the requirements of the expansion tunnel to the expansion tube for a given M_f. (Note that in this report $M_2 \approx 1.89$ is constant for all apparatus.)

The amount that β exceeds unity is an indication of the loss when the final expansion process is steady (expansion tunnel) rather than completely unsteady (expansion tube). As a consequence of the reduced-enthalpy multiplication in the unsteady expansion $\left(\frac{H_f}{H_2} \propto \frac{1}{\beta^2}\right)$, it will be shown that not only must the initial charging pressure be increased $p_1 \propto \beta^{\frac{2}{\gamma-1}}$ but also the primary-shock Mach number $\left(M_{S_1} \propto \beta\right)$.

The primary-shock Mach number can be evaluated by combining equations (8), (12), and (15); thus,

$$M_{S_1}\left(\frac{a_1}{a_f}\right) \approx \frac{\gamma + 1}{2} M_2 \frac{\Gamma_1(M_f)}{\Gamma_1(M_2)} \beta \tag{18}$$

The initial charging pressure ratio p_1/p_f is easily obtained by application of the gas law and the limiting strong shock density ratio

$$\frac{p_1}{p_f}\left(\frac{a_f}{a_1}\right)^2 = \frac{\rho_1}{\rho_f} = \left(\frac{\rho_1}{\rho_2}\right)\left(\frac{\rho_2}{\rho_f}\right) \approx \frac{\gamma - 1}{\gamma + 1}\left[\frac{\Gamma_1(M_f)}{\Gamma_1(M_2)}\,\beta\right]^{\frac{2}{\gamma-1}} \tag{19}$$

Figures 5 and 6 are plots of equations (18) and (19). Figure 5 indicates almost a constant increase in U_{S_1}/a_f with $\bar{A}$ independent of M_f, whereas figure 6 shows a marked dependence of ρ_1/ρ_f on M_f, the relative penalty associated with increasing $\bar{A}$ declining with larger M_f.

Accelerating-Gas Processes

The cases of accelerating gases with specific heat ratios γ_{11} of both 1.4 and 1.67 are considered. The initial charging pressure p_{11} is first determined by application of the strong shock approximation for p_{21}/p_{11} together with equation (4) and the equalities $p_e = p_{21}$ and $u_e = u_{21}$:

$$\frac{p_{21}}{p_{11}} = \frac{\gamma_{11}(\gamma_{11} + 1)}{2}\left(\frac{u_e}{u_f}\right)^2 M_f{}^2\left(\frac{a_f}{a_{11}}\right)^2 \tag{20}$$

$$\frac{p_{11}}{p_f}\left(\frac{a_f}{a_{11}}\right)^2 = \frac{2}{\gamma_{11}(\gamma_{11} + 1)}\left(\frac{u_f}{u_e}\right)^2 \frac{1}{M_f{}^2}\left(\frac{a_e}{a_f}\right)^{\frac{2\gamma}{\gamma-1}} \tag{21}$$

An evaluation of the absolute pressure level as influenced by γ_{11} and $\bar{A}$ results from manipulation of equation (21) into the form of equation (21a):

$$\frac{p_{11}}{p_f}\left(\frac{a_f}{a_1}\right)^2 = \frac{2}{\gamma_{11}(\gamma_{11} + 1)}\left(\frac{u_f}{u_e}\right)^2 \frac{1}{M_f{}^2}\left(\frac{a_e}{a_f}\right)^{\frac{2\gamma}{\gamma-1}}\left(\frac{a_{11}}{a_1}\right)^2 \tag{21a}$$

and in approximate form

$$\frac{p_{11}}{p_f}\left(\frac{a_f}{a_1}\right)^2 \approx \frac{2}{\gamma_1}\frac{1}{\gamma_{11}+1}\frac{\bar{A}^{\gamma}}{M_f^2}\left(\frac{\text{Molecular weight of gas in state } (1)}{\text{Molecular weight of gas in state } (11)}\right) \qquad (21b)$$

In figure 7, equation (21a) is plotted for values of $\frac{a_{11}}{a_1} = \frac{144}{49}$ and $\gamma_{11} = 1.67$. This value of a_{11}/a_1 is representative for $T_1 = T_{11}$ with perfect air in region (1) and helium in region (11). Since for many testing purposes a_f and a_1 might be nearly equal, the ratio $\frac{p_{11}}{p_f}\left(\frac{a_f}{a_1}\right)^2$ is a direct measure of the charging pressure. The pressure level in region (11) increases rapidly with $\bar{A}$ (eq. 21(b) and fig. 7) and reduces the low vacuum pumping requirements for the intermediate chamber. If air were also used in region (11), the values of $\frac{p_{11}}{p_f}\left(\frac{a_f}{a_1}\right)^2$ would then be 0.154 times those of figure 7.

The secondary-shock speed follows from equation (8):

$$U_{S_{11}} = \frac{\gamma_{11}+1}{2}\frac{u_e}{u_f}u_f \qquad (22)$$

$$U_{S_{11}} \approx \frac{\gamma_{11}+1}{2}u_f \qquad (22a)$$

Dump-Tank Processes

The conditions in the dump tank are found by assuming a perfect nozzle start and that the dump tank has an area equal to that of the nozzle exit. Such a start requires that there be no upstream compressions generated by the passage of the secondary shock $U_{S_{11}}$ through the nozzle. (See ref. 4.) Thus, the state (10) must be selected so that after acceleration to the state (20) by the tertiary shock $U_{S_{10}}$, the following conditions are satisfied: $p_{20} = p_{30}$; $u_{20} = u_{30}$. State (30) is defined by the steady-flow nozzle expansion of state (21). The relations between states (21) and (30) are analogous to those between states (e) and (f) except that M_{21} is constant at $\sqrt{\frac{2}{\gamma_{11}(\gamma_{11}-1)}}$.

Thus with the strong shock assumption for $U_{S_{10}}$, the expression for the initial nozzle charge pressure is

$$\left.\begin{aligned} \frac{p_{10}}{p_f} &= \left(\frac{p_{10}}{p_{20}}\right)\left(\frac{p_{30}}{p_{21}}\right)\left(\frac{p_e}{p_f}\right) \\ \frac{p_{10}}{p_f}\left(\frac{a_f}{a_{10}}\right)^2 &= \frac{2}{\gamma_{10}\left(\gamma_{10}+1\right)}\frac{1}{M_f{}^2}\frac{\left(p_e/p_f\right)}{\left(u_e/u_f\right)^2}\frac{\left(p_{30}/p_{21}\right)}{\left(u_{30}/u_{21}\right)^2} \end{aligned}\right\} \tag{23}$$

The approximate values of u_{30}/u_{21} and p_{30}/p_{21} are

$$\frac{u_{30}}{u_{21}} \approx \sqrt{\frac{\gamma_{11}+1}{1+\frac{2}{\gamma_{11}-1}\frac{1}{M_{30}{}^2}}} \tag{24}$$

$$\frac{p_{21}}{p_{30}} \approx \left(\gamma_{11}+1\right)^{\frac{\gamma_{11}}{2}}\left(\bar{A}\right)^{\gamma_{11}} \tag{25}$$

where

$$M_{30} \approx \sqrt{\frac{2}{\gamma_{11}\left(\gamma_{11}-1\right)}}\left(\gamma_{11}+1\right)^{\frac{\gamma_{11}+1}{4}}\left(\bar{A}\right)^{\frac{\gamma_{11}-1}{2}} \tag{26}$$

Substitution of equations (3a), (4a), and (24) to (26) into equations (23) results in

$$\frac{p_{10}}{p_f}\left(\frac{a_f}{a_{10}}\right)^2 \approx \frac{2}{\gamma_{10}\left(\gamma_{10}+1\right)}\frac{1}{M_f{}^2}\left(\bar{A}\right)^{\gamma-\gamma_{11}}\frac{1+\frac{\gamma_{11}}{\frac{\gamma_{11}+1}{2}}\left(\bar{A}\right)^{1-\gamma_{11}}}{\left(\gamma_{11}+1\right)^{\frac{\gamma_{11}+2}{2}}} \tag{23a}$$

The nozzle charging pressure parameter $\frac{p_{10}}{p_f}\left(\frac{a_f}{a_{10}}\right)^2$ of equations (23) is plotted in figure 8 for $\gamma = 1.4$ with γ_{10} and γ_{11} equal to 1.4 and 1.67. As indicated by equation (23a), this pressure parameter is only a weak function of area ratio when $\gamma = \gamma_{11}$ and $\bar{A} \gg 1$. (See figs. 8(a) and 8(b).) Lower charging pressures are required for larger values of $\bar{A}$ when $\gamma \neq \gamma_{11}$.

A parameter illustrative of the absolute pressure level for the case of air as the test gas with helium or air for the other charging gases would be $\frac{p_{10}}{p_f}\left(\frac{a_f}{a_1}\right)^2$, which is found as

$$\frac{p_{10}}{p_f}\left(\frac{a_f}{a_1}\right)^2 = \frac{p_{10}}{p_f}\left(\frac{a_f}{a_{10}}\right)^2\left(\frac{a_{10}}{a_1}\right)^2 \tag{27}$$

This parameter is plotted in figure 9 for the ratios $\frac{a_{10}}{a_1} = 1.0$ for $\gamma = \gamma_{10}$ and $\frac{a_{10}}{a_1} = \frac{144}{49}$ for $\gamma_{10} = 1.667$. These sonic-speed ratios are appropriate for $T_1 = T_{10}$ with air or helium as the nozzle gas in state (10). The lower pressures (higher vacuums) are required for air in both states (10) and (11). The combination of helium in state (10) and air in state (11) permits higher initial p_{10} (for $M_f > 25$, $\bar{A} > 25$) than if helium were used in both states (10) and (11). The case of $\gamma_{10} = \frac{5}{3}$ and $\gamma_{11} = \frac{7}{5}$ requires a p_{10} reduction of about one order of magnitude between $\bar{A} = 1$ and $\bar{A} = 100$, and the value of $p_{10} \approx 5 \times 10^{-4}\, p_f$ at $\bar{A} \approx 10$.

The exact expression for the tertiary shock velocity $U_{S_{10}}$ (eq. (28)) may be put into a simpler approximate form by using the strong shock relation together with the assumption of a perfect initial nozzle start and equations (3a) and (24):

$$\frac{U_{S_{10}}}{u_f} = \frac{U_{S_{10}}}{u_{20}}\frac{u_{20}}{u_{30}}\frac{u_{30}}{u_{21}}\frac{u_e}{u_f} \tag{28}$$

$$\frac{U_{S_{10}}}{u_f} \approx \frac{\gamma_{10} + 1}{2} \sqrt{\frac{\gamma_{11} + 1}{1 + \frac{2}{\gamma_{11} - 1} \frac{1}{M_{30}^2}}} \tag{28a}$$

When the test gas flows through the nozzle from state (e) to state (f), the velocity $u_f \neq u_{30}$ and $p_f \neq p_{30}$; in fact, from equations (3a), (4a), (24), and (25)

$$\frac{u_{30}}{u_f} = \frac{u_{30}}{u_{21}} \frac{u_e}{u_f} \approx \sqrt{\frac{\gamma_{11} + 1}{1 + \frac{2}{\gamma_{11} - 1} \frac{1}{M_{30}^2}}} \tag{29}$$

$$\frac{p_{30}}{p_f} = \frac{p_{30}}{p_{21}} \frac{p_e}{p_f} \approx \left(\gamma_{11} + 1\right)^{-\frac{\gamma_{11}}{2}} (\bar{A})^{\gamma - \gamma_{11}} \tag{30}$$

Since for $\bar{A} \geq 1$, $M_{30} \geq M_{21} = \sqrt{\frac{2}{\gamma_{11}\left(\gamma_{11} - 1\right)}}$, it follows from equation (29) that $u_{30} > u_f$. Also, for $\gamma \leq \gamma_{11}$, $p_{30} < p_f$ from equation (30). Consequently, the unsteady wave system generated by the passage of the test-gas—accelerating-gas interface (between state (e) and state (21)) through the nozzle must attempt to adjust the states (f) and (30) to a common velocity and pressure. A schematic sketch and distance-time (wave) diagram of the processes leading to the establishment of the states (f) and (30) are shown in figures 10(a) and 10(b). For a perfect initial nozzle start, state (30) is identical to state (40). The pressure and velocity of states (f) and (30) (fig. 10(c)) must now be matched at a common point (g,50) by means of an upstream wave, state (f) → state (g) with $\frac{dp}{du} < 0$, and a downstream wave, state (30) → state (50) with $\frac{dp}{du} > 0$. These conditions are indicated for cases I, II, and III by the dashed lines in figure 10(c). If both adjusting waves are isentropic, the equation governing the wave strength p_g/p_f is

$$\frac{\gamma_{11} - 1}{\gamma - 1} \frac{M_{30}}{M_f} \frac{u_f}{u_e} \frac{u_{21}}{u_{30}} \left[1 + \frac{\gamma - 1}{2} M_f - \left(\frac{p_g}{p_f}\right)^{\frac{\gamma-1}{2\gamma}}\right] = -1 + \frac{\gamma_{11} - 1}{2} M_{30} + \left(\frac{p_f}{p_e} \frac{p_{21}}{p_{30}} \frac{p_g}{p_f}\right)^{\frac{\gamma_{11}-1}{2\gamma_{11}}} \tag{31}$$

Equation (28) is only dependent on γ, γ_{11}, M_f, and $\bar{A}$. Solutions of equation (31) showed that, in general, cases II and III of figure 10(c) applied with all reflections as expansion waves. Only for the condition $\gamma_{11} = \frac{5}{3}$ and $M_e \rightarrow M_2$ did the wave system of case I occur. Since for this condition the maximum pressure ratio p_{50}/p_{30} was only 1.6 for $\bar{A} = 10^3$ and $M_e = M_2$, the isentropic equation (31) is still a close approximation even for case I.

The wave strengths p_g/p_f for $\gamma = \gamma_{11} = 1.4$ are plotted in figure 11(a) and for $\gamma = 1.4$, $\gamma_{11} = \frac{5}{3}$ in figure 11(b). Note that $\frac{p_g}{p_f} \leqq 1$ so that upstream expansion waves are generated which will not disturb the expansion flow at the nozzle-exit model location. There are no solutions in figure 11(b) for the larger area ratios because for these cases no positive values of p_f will satisfy equation (28); that is, case III of figure 10(c) falls below the p-axis. Physical considerations naturally limit p_g and p_{50} to zero; therefore, the wave system for these cases creates a perfect vacuum which grows in extent with time since $u_g < u_{50}$ at $p = 0$. This high-vacuum-producing mechanism may offer interesting possibilities for other experiments.

One more wave interaction must be considered in the dump tank, namely the end reflection of the shock wave with a velocity of $U_{S_{10}}$. If it is assumed that the wave is unaffected by any overtaking waves and that the state (20) is the state into which the reflected shock wave with velocity U_{S_R} will advance, the following equation applies:

$$\left|\frac{U_{S_R}}{a_{10}}\right| = \sqrt{\frac{\gamma_{10} - 1}{2\gamma_{10}}} \frac{2\frac{p_{20}}{p_{10}} + \frac{2}{\gamma_{10} - 1}}{\sqrt{1 + \frac{\gamma_{10} + 1}{\gamma_{10} - 1}\frac{p_{20}}{p_{10}}}} \tag{32}$$

If the strong shock approximations are used, equation (32) simplifies to

$$\left.\begin{aligned} \left|U_{S_R}\right| &= (\gamma_{10} - 1)u_{20} = \frac{2(\gamma_{10} - 1)}{\gamma_{10} + 1} U_{S_{10}} \\ \left|U_{S_R}\right| &\approx (\gamma_{10} - 1)\sqrt{\frac{\gamma_{11} + 1}{1 + \frac{2}{\gamma_{11} - 1}\frac{1}{M_{30}^2}}}\, u_f \end{aligned}\right\} \tag{32a}$$

Also under the strong-shock assumption, the pressure after the reflected shock p_{RS} is

$$\frac{p_{RS}}{p_{20}} = \frac{3\gamma_{10} - 1}{\gamma_{10} - 1} \tag{33}$$

$$\frac{p_{RS}}{p_f} = \frac{p_{RS}}{p_{20}} \frac{p_{20}}{p_{10}} \frac{p_{10}}{p_f} \tag{34}$$

Substituting approximate equations (23a) and (28a) into equation (34) yields the large-area-ratio asymptotic expression

$$\left.\begin{aligned} &\frac{p_{RS}}{p_f} \approx \frac{3\gamma_{10} - 1}{\gamma_{10} - 1}(\gamma_{11} + 1)^{-\frac{\gamma_{11}}{2}} \bar{A}^{\gamma - \gamma_{11}} \\ &\frac{p_{RS}}{p_f} \approx 4.34 \qquad \left(\gamma = \gamma_{10} = \gamma_{11} = 1.4\right) \\ &\frac{p_{RS}}{p_f} \approx 3.25 \qquad \left(\gamma = \gamma_{11} = 1.4;\ \gamma_{10} = 1.67\right) \\ &\frac{p_{RS}}{p_f} \approx 2.66(\bar{A})^{-0.27} \qquad \left(\gamma = 1.4;\ \gamma_{10} = \gamma_{11} = 1.67\right) \end{aligned}\right\} \tag{34a}$$

Consequently, p_{RS} is of the same order as p_f and will be (for large area ratios) essentially independent of $\bar{A}$ if $\gamma_{11} = \gamma$, whereas p_{RS} will decrease with increasing $\bar{A}$ for $\gamma_{11} > \gamma$. Solutions of the exact equation (34) are not shown but follow the trend described for large M_f. However, as M_f decreases, p_{RS}/p_f increases somewhat.

Driver-Gas Processes

The driver-gas pressure level is evaluated by first finding the ratio p_4/p_3 across the driver-gas unsteady flow expansion:

$$\frac{p_4}{p_3} = \left(\frac{a_4}{a_3}\right)^{\frac{2\gamma_4}{\gamma_4 - 1}} = \left(1 - \frac{\gamma_4 - 1}{2} M_2 \frac{a_2}{a_f} \frac{a_f}{a_1} \frac{a_1}{a_4}\right)^{-\frac{2\gamma_4}{\gamma_4 - 1}} \tag{35}$$

The ratio of driver-gas pressure to test-gas pressure results from combining equations (12), (13), and (35):

$$\frac{p_4}{p_f} = \frac{p_4}{p_3}\frac{p_2}{p_f} = \left[1 - \frac{\gamma_4 - 1}{2} M_2 \frac{a_1}{a_4}\frac{a_f}{a_1}\beta \frac{\Gamma_1(M_f)}{\Gamma_1(M_2)}\right]^{-\frac{2\gamma_4}{\gamma_4 - 1}} \left[\frac{\Gamma_1(M_f)}{\Gamma_1(M_2)}\beta\right]^{\frac{2\gamma}{\gamma-1}} \tag{36}$$

The ratio of driver-gas pressures required for expansion-tunnel operation to that for expansion-tube operation $\left(\frac{A_4}{A_e} = 1\right)$, for the case of identical test-section conditions, is then

$$\frac{(p_4)_{ETun}}{(p_4)_{ET}} = \beta^{\frac{2\gamma}{\gamma-1}} \left[\frac{1 - \frac{\gamma_4 - 1}{2} M_2 \frac{\Gamma_1(M_f)}{\Gamma_1(M_2)}\frac{a_f}{a_4}}{1 - \frac{\gamma_4 - 1}{2} M_2 \frac{\Gamma_1(M_f)}{\Gamma_1(M_2)}\frac{a_f}{a_4}\beta}\right]^{\frac{2\gamma_4}{\gamma_4 - 1}} \tag{37}$$

$$\frac{(p_4)_{ETun}}{(p_4)_{ET}} = \beta^{\frac{2\gamma}{\gamma-1}} \left[\frac{1 - \frac{\gamma_4 - 1}{2}\left(\frac{u_2}{a_4}\right)_{ET}}{1 - \frac{\gamma_4 - 1}{2}\left(\frac{u_2}{a_4}\right)_{ETun}}\right]^{\frac{2\gamma_4}{\gamma_4 - 1}} \tag{37a}$$

If a driver gas with a very high speed of sound is used so that $\frac{u_2}{a_4} \ll 1$, the expression in brackets approaches unity. If, in addition, the approximation (17c) is used for β, the driver-gas pressure ratio becomes

$$\frac{(p_4)_{ETun}}{(p_4)_{ET}} \approx \beta^{\frac{2\gamma}{\gamma-1}} \tag{38}$$

$$\frac{(p_4)_{ETun}}{(p_4)_{ET}} \approx 1 + \frac{2\gamma}{\gamma - 1}\frac{(\bar{A})^{\frac{\gamma-1}{2}} - 1}{\Gamma_1(M_f)} + \frac{\gamma(\gamma + 1)}{(\gamma - 1)^2}\left[\frac{(\bar{A})^{\frac{\gamma-1}{2}} - 1}{\Gamma_1(M_f)}\right]^2 + \cdots \tag{38a}$$

If the assumption is added that $M_f \gg \frac{2}{\gamma - 1}$,

$$\frac{(p_4)_{ETun}}{(p_4)_{ET}} \approx 1 + \frac{4\gamma}{(\gamma - 1)^2} \frac{(\bar{A})^{\frac{\gamma-1}{2}} - 1}{M_f} + \frac{4\gamma(\gamma + 1)}{(\gamma - 1)^4} \frac{\left[(\bar{A})^{\frac{\gamma-1}{2}} - 1\right]^2}{M_f^2} + \cdots \tag{38b}$$

Driver-gas pressure ratios from equation (36) are plotted in figure 12 for the case of $\gamma_4 = \frac{5}{3}$, $\frac{a_4}{a_f} = \frac{144}{49}\sqrt{\frac{T_4}{T_f}}$, with values of $\frac{T_4}{T_f} = 10$, 25, and 50. The increase in driver-gas pressure with increasing nozzle area ratios is evident together with a decrease in p_4 as $a_4(T_4)$ increases. Such a trend was expected from shock-tunnel experience. The decreasing difference between tunnel and tube pressures as M_f increases is also apparent, a trend predicted simply by the approximation equations (38). At large M_f, $\left(p_4/p_f\right)$ for $\bar{A} = 10^3$ is about ten times $\left(p_4/p_f\right)$ for $\bar{A} = 1$.

LENGTHS OF COMPONENT SECTIONS AND TESTING TIMES

Accelerating Chamber

The accelerating chamber length l_{S_2} is the fundamental one in the apparatus since it determines the testing time. Let Δt_2 be defined as the time interval at the nozzle entrance between the arrival of the test gas and the trailing edge of the upstream expansion fan; that is, it is the time for which the state ⓔ exists at the nozzle entrance (figs. 1 and 13) and would be the test time for a zero-length nozzle. The nondimensional equation for Δt_2 is

$$\frac{a_f \Delta t_2}{l_{S_2}} = \frac{1}{M_e(M_e - 1)}\left(\frac{a_f}{a_e}\right) \tag{39}$$

or in an approximate form by substituting equations (1a) and (2a):

$$\frac{a_f \Delta t_2}{l_{S_2}} \approx \frac{1}{M_f^2}(\bar{A})^{\frac{\gamma-1}{2}}\left[1 - \frac{(\bar{A})^{\frac{\gamma-1}{2}}}{M_f}\right]^{-1} \tag{39a}$$

The test time parameter $\frac{a_f \Delta t_2}{l_{S_2}}$ of equation (39) is plotted in figure 14. Note that for a given M_f significant gains in Δt_2 are obtainable by the tunnel mode of operation; equation (39a) indicates gains roughly proportional to $(\bar{A})^{\frac{\gamma-1}{2}}$.

Also shown in figure 14 is the nonreflected shock tunnel testing time together with ticks indicating the values of $\bar{A}$ required to attain M_f by a steady nozzle expansion. The strong-shock approximations require:

$$\left(\frac{a_f \Delta t_2}{l_{S_1}}\right)_{NRS} \approx \frac{\gamma - 1}{\sqrt{\gamma + 1}} \frac{1}{M_f} \tag{40}$$

$$\left.\begin{aligned} \bar{A}_{NRS} &\approx \sqrt{\frac{2}{\gamma(\gamma - 1)}} \left(\frac{\gamma}{2} \frac{\gamma - 1}{\gamma + 1}\right)^{\frac{\gamma+1}{2(\gamma-1)}} M_f^{\frac{2}{\gamma-1}} \\ \bar{A}_{NRS} &\approx 0.003 M_f^{5} \qquad (\gamma = 1.4) \end{aligned}\right\} \tag{41}$$

The length l_{S_1} is used for the shock tunnel since there are no l_{S_2} lengths required.

The zero-nozzle-length expansion-tunnel test times are much shorter than those for the nonreflected shock tunnel, although the latter, of course, must have a much larger area ratio nozzle for the same M_f. The effect of nonzero nozzle length will be discussed subsequently.

Nozzle

In order to specify the nozzle length l_N, consideration must be given to the time lost in starting and stopping the nozzle. An analysis of this problem for expansion-tunnel operation will be based on the perfect start approach. (See ref 4.) Expressions for the nozzle-time losses will be found for nozzles in which the local area ratio varies with both the first and second power of distance (linear area ratio and conical nozzles).

The notations used are Δt_{flow}, Δt_+, and Δt_- for the times required for a transversal of the nozzle by a fluid particle, a downstream characteristic wave (which travels with local velocity $u + a$), and an upstream characteristic wave (which travels with local velocity $u - a$), respectively. The following expressions are valid for the times shown in figure 13:

For a nozzle where $A(\xi) = A_e(1 + C\xi)$

$$\frac{a_f \Delta t_{flow}}{l_N} = \frac{a_f}{l_N} \int_0^{l_N} \frac{d\xi}{u(\xi)} = \int_0^1 \frac{a_f}{a(\xi)} \frac{d\,\frac{\xi}{l_N}}{M(\xi)} \tag{42}$$

$$\frac{a_f \Delta t_{flow}}{l_N} = K_1\left(\bar{A}, M_f\right)\left(I_1 - I_3\right) \tag{42a}$$

where

$$I_n\left(M_e, M_f\right) \equiv \int_{M_e}^{M_f} \frac{\left[\Gamma_2(M)\right]^{\frac{1}{\gamma-1}}}{M^n}\, dM \tag{43}$$

$$K_1\left(\bar{A}, M_f\right) \equiv \frac{M_f}{\left(1 - \bar{A}^{-1}\right)\left[\Gamma_2\left(M_f\right)\right]^{\frac{\gamma}{\gamma-1}}} \tag{44}$$

Also

$$\frac{a_f \Delta t_+}{l_N} = \int_0^1 \frac{a_f}{a\left(\frac{\xi}{l_N}\right)} \frac{d\left(\frac{\xi}{l_N}\right)}{M\left(\frac{\xi}{l_N}\right) + 1} \tag{45}$$

$$\frac{a_f \Delta t_+}{l_N} = K_1\left(\bar{A}, M_f\right)\left(I_1 - I_2\right) \tag{45a}$$

$$\frac{a_f \Delta t_-}{l_N} = \int_0^1 \frac{a_f}{a\left(\frac{\xi}{l_N}\right)} \frac{d\left(\frac{\xi}{l_N}\right)}{M\left(\frac{\xi}{l_N}\right) - 1} \tag{46}$$

$$\frac{a_f \Delta t_-}{l_N} = K_1\left(\bar{A}, M_f\right)\left(I_1 + I_2\right) \tag{46a}$$

The nozzle "starting loss" is herein defined as the testing time lost (at the nozzle exit) due to the starting process and is equal to the difference between the times $t_x - t_w$ (see fig. 13):

$$\left.\begin{aligned} \Delta t_{start} &\equiv t_x - t_w \\ \Delta t_{start} &= -\left(t_y - t_x\right) + \left(t_y - t_w\right) \end{aligned}\right\} \tag{47}$$

$$\Delta t_{start} = \Delta t_- - \Delta t_{flow} \tag{47a}$$

$$\frac{a_f \Delta t_{start}}{l_N} = K_1\left(\bar{A}, M_f\right)\left(I_2 + I_3\right) \tag{48}$$

Similarly, the nozzle "stopping loss" is defined as the test time lost (at the nozzle exit) because the downstream characteristic disturbance which signals the arrival of the expansion-fan trailing edge at the nozzle entrance precedes the fluid through the nozzle:

$$\left.\begin{aligned} \Delta t_{stop} &\equiv t_y' - t_z' \\ \Delta t_{stop} &= \left(t_y' - t_x'\right) - \left(t_z' - t_x'\right) \end{aligned}\right\} \tag{49}$$

$$\Delta t_{stop} = \Delta t_{flow} - \Delta t_+ \tag{49a}$$

$$\frac{a_f \Delta t_{stop}}{l_N} = K_1\left(\bar{A}, M_f\right)\left(I_2 - I_3\right) \tag{50}$$

The total loss in test time due to the finite nozzle length is then the sum of the starting and stopping losses:

$$\frac{a_f \Delta t_{loss}}{l_N} = 2K_1\left(\bar{A}, M_f\right) I_2 \tag{51}$$

Corresponding equations for a conical nozzle, where $A(\xi) = A_e(1 + C'\xi)^2$, are as follows:

$$\frac{a_f \Delta t_{flow}}{l_N} = K_2\left(\bar{A}, M_f\right)\left(J_{1/2} - J_{5/2}\right) \tag{52}$$

$$\frac{a_f \Delta t_+}{l_N} = K_2\left(J_{1/2} - J_{3/2}\right) \tag{53}$$

$$\frac{a_f \Delta t_-}{l_N} = K_2\left(J_{1/2} + J_{3/2}\right) \tag{54}$$

$$\frac{a_f \Delta t_{loss}}{l_N} = 2K_2\left(\bar{A}, M_f\right) J_{3/2} \tag{55}$$

where

$$J_n\left(M_e, M_f\right) \equiv \int_{M_e}^{M_f} \frac{\left[\Gamma_2(M)\right]^{\frac{3-\gamma}{4(\gamma-1)}}}{M^n}\, dM \tag{56}$$

$$K_2\left(\bar{A}, M_f\right) \equiv \frac{\sqrt{M_f}}{2\left(1 - \bar{A}^{-\frac{1}{2}}\right)\left[\Gamma_2\left(M_f\right)\right]^{\frac{3\gamma-1}{4(\gamma-1)}}} \tag{57}$$

Curves of $I_n\left(1, M_f\right)$ and $J_n\left(1, M_f\right)$ are plotted in figure 15 for $\gamma = 1.4$ and $\gamma = 5/3$. An arbitrary lower limit for M_e of unity has been used in these plots; however, the value for any specified limits is simply the difference of the values at $M = M_f$ and $M = M_e$. For the case where $\left[M\left(\frac{\xi}{l_N}\right)\right]^2 \gg \frac{2}{\gamma - 1}$, approximations to the indefinite integral for I_n and J_n are

$$I_n(M) \approx \left(\frac{\gamma - 1}{2}\right)^{\frac{1}{\gamma-1}} \frac{M^{\frac{\gamma+1}{\gamma-1} - n}}{\frac{\gamma + 1}{\gamma - 1} - n} \tag{58}$$

$$J_n(M) \approx \left(\frac{\gamma - 1}{2}\right)^{\frac{3-\gamma}{4(\gamma-1)}} \frac{M^{\frac{\gamma+1}{2(\gamma-1)} - n}}{\frac{\gamma + 1}{2(\gamma - 1)} - n} \tag{59}$$

These approximations are shown as the dashed curves in figure 15. It is evident that such approximations would be very good for evaluating the finite integral when M_f and M_e are not small.

In order to evaluate the fraction of the time Δt_2 lost in the nozzle processes, a nozzle loss parameter is introduced and defined as $\left(\frac{\Delta t_{loss}}{\Delta t_2}\right)_{ETun}\left(\frac{l_{S_2}}{l_N}\right)$. This parameter is plotted for the linear-area nozzle in figure 16 together with the approximate equation:

$$\left(\frac{\Delta t_{loss}}{\Delta t_2}\right)_{ETun}\left(\frac{l_{S_2}}{l_N}\right) \approx \frac{4}{3 - \gamma} \frac{1}{(\bar{A})^{\frac{\gamma-1}{2}}}\left[1 - \frac{(\bar{A})^{\frac{\gamma-1}{2}}}{M_f}\right]\left[\frac{1 - (\bar{A})^{-\frac{3-\gamma}{2}}}{1 - (\bar{A})^{-1}}\right] \tag{60}$$

$$\left(\frac{\Delta t_{loss}}{\Delta t_2}\right)_{ETun}\left(\frac{l_{S_2}}{l_N}\right) \approx \frac{4}{3 - \gamma} \frac{M_e - 1}{M_f}\left[\frac{1 - (\bar{A})^{-\frac{3-\gamma}{2}}}{1 - (\bar{A})^{-1}}\right] \tag{60a}$$

Equation (60) retains orders in the reciprocal of $\bar{A}$ which have been previously neglected. This retention is necessary to gain accuracy for this case.

The nozzle losses are not excessive for $l_N < l_{S_2}$. In fact, for large $\bar{A}$, the nozzle length can actually exceed the accelerating-chamber length before the test time vanished (that is, $\Delta t_{loss} = \Delta t_2$). The reason that the $\bar{A} = 1$ curve does not have $\Delta t_{loss} \equiv 0$ is that by definition the test time is bounded by the upstream and downstream characteristics from the nozzle entrance (fig. 13). Consequently, for $\bar{A} = 1$ and $M_f \gg 1$, the nozzle loss parameter approaches two.

The comparable loss parameter for the nonreflected shock tunnel is also plotted in figure 16 by using the following approximation:

$$\left(\frac{\Delta t_{loss}}{\Delta t_2}\right)_{NRS}\left(\frac{l_N}{l_{S_1}}\right)^{-1} \approx \frac{4}{3-\gamma}\frac{\sqrt{\gamma+1}}{\gamma-1}\frac{1}{M_f} \tag{61}$$

The values of $\bar{A}$ of the shock tunnel are indicated by ticks on the curve.

At a given value of M_f and for the same ratio of l_N/l_S, these curves indicate that $\Delta t_{loss}/\Delta t_2$ is greater for the expansion tunnel than for the shock tunnel. However, to obtain high M_f, the value of $\bar{A}$ becomes extremely large in the nonreflected shock tunnel (for example, at $M_f = 50$, $\bar{A}_{NRS} \approx 10^6$) so that for a given nozzle wall slope the shock-tunnel nozzle length l_N might be much larger than that of the expansion tunnel. A further consideration of this problem can be found in the "Discussion" part of this paper.

The ratio of nozzle loss times for expansion-tunnel nozzles, the radii of which vary linearly with distance, to the loss times for those nozzles with a linear area variation is for the same M_f, l_N, and $\bar{A}$

$$\frac{(\Delta t_{loss})_{linear\ radius}}{(\Delta t_{loss})_{linear\ area}} = \frac{K_2 J_{3/2}}{K_1 I_2} \approx F(\bar{A}) \tag{62}$$

where

$$F(\bar{A}) = \frac{3-\gamma}{2(2-\gamma)}\frac{1-(\bar{A})^{-\frac{2-\gamma}{2}}}{1-(\bar{A})^{-\frac{3-\gamma}{2}}}\left(1+\bar{A}^{-1/2}\right) \tag{62a}$$

$$F(\bar{A}) = \frac{4}{3}\frac{1-(\bar{A})^{-0.3}}{1-(\bar{A})^{-0.8}}\left[1+(\bar{A})^{-0.5}\right] \qquad (\gamma = 1.4) \tag{62b}$$

For $M_f > 20$ and $\bar{A} > 10$, the approximation values of equation (62b) which are plotted in figure 17 are within 3 percent of those of equation (62), $\left(\frac{K_2 J_{3/2}}{K_1 I_2}\right)$. The nozzle losses in the linear-radius nozzle (conical nozzle) are thus slightly in excess of the linear-area nozzle and approach a limit of 4/3 as $\bar{A}$ approaches ∞.

Another aspect of the nozzle starting process which was considered was the nozzle-length requirement to ensure that the accelerating gas flow had been completely established in the nozzle before the test gas reached the nozzle exit. This criterion prohibits any interference between the nozzle starting processes of the two gases. It was found that this requirement was satisfied as long as l_N was no greater than approximately one-half l_{S_2} for $\bar{A} > 10$ and for values of γ_{11} equal to both 1.4 and 1.67.

Intermediate Chamber

The intermediate chamber length l_{S_1} is determined so that the reflection generated at the intersection of the leading edge of the expansion fan with the driver-gas—test-gas interface (between ③ and ②) will arrive at the nozzle entrance simultaneously with the trailing edge of the expansion fan. (See fig. 1.) The governing equation is

$$\frac{l_{S_1}}{l_{S_2}} = \frac{\gamma + 1}{\gamma - 1} \frac{1}{M_e - 1} \left[\frac{\Gamma_1(M_2)}{\Gamma_1(M_e)} \right]^{\frac{3-\gamma}{2(\gamma-1)}} \tag{63}$$

and this ratio of l_{S_1}/l_{S_2} is plotted in figure 18. For a given value of $\bar{A}$ and l_{S_2}, the length l_{S_1} decreases rapidly with increasing M (approximately as M^{-3} for large M). And at a constant (large) value of M, the ratio l_{S_1}/l_{S_2} increases nearly as $A^{0.6}$. Thus, expansion-tunnel operation requires longer intermediate chambers than those for an expansion tube with equal l_{S_2}. In the extreme case of large $\bar{A}$ and low M_f, the lengths l_{S_1} and l_{S_2} are of the same order; however, for high M_f and large $\bar{A}$, l_{S_1} is only a few percent of l_{S_2}.

Dump-Tank Length

An approximation to the dump-tank length l_{S_R} may be found by introducing the following simplifying assumptions: (a) the nozzle length is zero; (b) the shock velocities $U_{S_{10}}$ and U_{S_R} are constant during shock-wave traversal of the dump tank; and (c) the total traversal time of these shocks is equal to the time interval between the arrival at the nozzle of the shock wave $U_{S_{11}}$ and the trailing edge of the expansion fan. Thus

$$l_{S_R}\left(\frac{1}{U_{S_{10}}} + \frac{1}{\left|U_{S_R}\right|}\right) = \left(\Delta t_1 + \Delta t_2\right) - \frac{l_{S_2}}{U_{S_{11}}} \tag{64}$$

which can be operated on by substituting equations (3), (28), (32), and (39) plus the relation

$$\Delta t_1 = u_e^{-1} l_{S_2}$$

to yield

$$\frac{l_{S_R}}{l_{S_2}} \approx \frac{\left(\gamma_{10} - 1\right)\left(\gamma_{10} + 1\right)}{3\gamma_{10} - 1}\left(\frac{\gamma_{11} - 1}{\gamma_{11} + 1} + \frac{1}{M_e - 1}\right)\left(\frac{\gamma_{11} + 1}{1 + \frac{2}{\gamma_{11} - 1}\frac{1}{M_{30}^2}}\right)^{1/2} \tag{65}$$

The variation of l_{S_R} with M_f is shown in figure 19(a) for $\gamma_{10} = \frac{5}{3}$ and $\gamma_{11} = \frac{7}{5}$ and in figure 19(b) for $\gamma_{10} = \gamma_{11} = \frac{5}{3}$. Larger values of l_{S_R} are required with increasing $\bar{A}$, but the percentage increase is small for large M_f. Also the values of l_{S_R} are smaller when $\gamma_{11} = \frac{7}{5}$ rather than $\frac{5}{3}$. Not shown are plots for $\gamma_{10} = \gamma_{11} = \frac{7}{5}$, but these values are approximately two-thirds those for $\gamma_{10} = \frac{5}{3}$, $\gamma_{11} = \frac{7}{5}$ (fig. 19(a)).

Driver-Chamber Length

The driver cross-sectional area is assumed to be equal to that of the intermediate and expansion chambers. The driver length is determined so that the reflection of the driver rarefaction wave off the end plate will pass through the point m (fig. 1) where the entropy discontinuity between ③ and ② intersects the leading edge of the main expansion fan. For these conditions

$$\frac{l_D}{l_{S_1}} = \frac{a_4}{U_{S_1}}\frac{\Delta t_i}{\Delta t_o} \tag{66}$$

$$\frac{l_D}{l_{S_1}} \approx \frac{1}{\gamma + 1} \frac{1}{M_2} \frac{a_4}{a_f} \left(\frac{a_3}{a_4}\right)^{\frac{\gamma_4+1}{2(\gamma_4-1)}} \frac{\left[\Gamma_1(M_2)\right]^2}{\Gamma_1(M_e)} \left[\frac{\Gamma_2(M_e)}{\Gamma_2(M_f)}\right]^{1/2} \tag{66a}$$

$$\frac{l_D}{l_{S_1}} \approx \frac{1}{\gamma + 1} \frac{1}{M_2} \frac{a_4}{a_f} \left[1 - \frac{\gamma_4 - 1}{2} M_2 \frac{\Gamma_1(M_f)}{\Gamma_1(M_2)} \beta \frac{a_f}{a_4}\right]^{\frac{\gamma_4+1}{2(\gamma_4-1)}} \frac{\left[\Gamma_1(M_2)\right]^2}{\Gamma_1(M_f)} \frac{1}{\beta} \tag{66b}$$

From figures 20 which are drawn for values of a_4/a_f equal to those of figures 12, it is evident that l_D/l_{S_1} decreases with increasing $\bar{A}$. Consequently, in terms of matching the driver and intermediate chambers, the expansion tunnel is less restrictive on driver length. However, since l_{S_1}/l_{S_2} increases with $\bar{A}$ (fig. 18), the net result is an increase in l_D/l_{S_2} with $\bar{A}$ as illustrated in figure 21 for the intermediate value of $\frac{a_4}{a_f} = 5\left(\frac{144}{49}\right)$. The driver lengths in the expansion tunnel are thus significantly larger than those of the expansion tube; for example, at $M_f = 50$, $\frac{(l_D)_{ETun}}{(l_D)_{ET}}$ is approximately 10 at $\bar{A} = 100$ and approximately 25 at $\bar{A} = 1000$. However, even at $\bar{A} = 1000$, $l_D \approx 0.01 l_{S_2}$ for $M_f = 50$.

DISCUSSION

Diaphragm Bursting

Secondary diaphragm.- Reference 1 pointed out the criticalness of the secondary-diaphragm burst because of the fact that only an extremely small part of the gas initially in the intermediate chamber is actually used for testing. If the extent of this gas in state ① is designated as z, from continuity

$$z = \frac{\rho_f}{\rho_1} \bar{A} u_f \Delta t_2 \tag{67}$$

and by substitution, equation (67) becomes

$$\frac{z}{l_{S_2}} = \frac{\gamma + 1}{\gamma - 1}\frac{1}{M_f}\left[\frac{\bar{\Gamma}_1(M_2)}{\Gamma_1(M_f)}\frac{1}{\beta}\right]^{\frac{2}{\gamma-1}}\left[1 - \frac{(\bar{A})^{\frac{\gamma-1}{2}}}{M_f}\right]^{-1}(\bar{A})^{\frac{\gamma+1}{2}} \tag{68}$$

$$\frac{z}{l_{S_2}} \approx \frac{\gamma + 1}{\gamma - 1}\frac{1}{M_f}\left[\frac{\Gamma_1(M_2)}{\frac{\gamma - 1}{2}M_f + (\bar{A})^{\frac{\gamma-1}{2}}}\right]^{\frac{2}{\gamma-1}}\left[1 - \frac{(\bar{A})^{\frac{\gamma-1}{2}}}{M_f}\right]^{-1}(\bar{A})^{\frac{\gamma+1}{2}} \tag{68a}$$

Thus, for equal values of l_{S_2} and test conditions (f), the ratio of the length z for the expansion tunnel to that for the expansion tube is

$$\frac{(z)_{ETun}}{(z)_{ET}} \approx (\bar{A})^{\frac{\gamma+1}{2}}\left[\frac{\Gamma_1(M_f)}{\frac{\gamma - 1}{2}M_f + (\bar{A})^{\frac{\gamma-1}{2}}}\right]^{\frac{2}{\gamma-1}}\frac{M_f - 1}{M_f - (\bar{A})^{\frac{\gamma-1}{2}}} \tag{69}$$

The relation of equation (67) is plotted in figure 22 for $l_N = 0$ and shows order-of-magnitude gains in z/l_{S_2} with increasing $\bar{A}$. The primary part of this gain is attributable to simply the fact that to store the same mass of "test slug" in a reduced cross-sectional area requires a longer length if the initial charge densities were the same. The other contribution to the net gain is a result of the increased test-slug mass due to increased testing time more than compensating for the increase with $\bar{A}$ of the initial charge density ρ_1. For $M_e \gg \frac{2}{\gamma - 1}$, the gain is proportional to $(\bar{A})^{\frac{\gamma+1}{2}}$ (eq. (69)) at a given M_f.

The secondary-diaphragm bursting problem is alleviated even further when diaphragm opening time is considered. If the diaphragm is assumed to be near its rupture stress at pressure p_1, for a given material the opening time is proportional to the tab radius divided by the square root of the primary shock pressure ratio p_2/p_1. The fluid mass passing the diaphragm station during opening is thus included in a length proportional to $u_2 d\left(\frac{p_2}{p_1}\right)^{-\frac{1}{2}} \propto a_1 d$. An indication of the secondary diaphragm problem is then the ratio z/d with

larger values of z/d desired. For the same test-section conditions (f), test-section size, and accelerating-chamber length l_{s_2}, the ratios of z/d are found from equation (69) to be

$$\frac{(z/d)_{ETun}}{(z/d)_{ET}} \approx (\bar{A})^{\frac{\gamma+2}{2}} \qquad \left(M_e \gg \frac{2}{\gamma - 1}\right) \tag{70}$$

For $\bar{A} \approx 100$ and $\bar{A} \approx 1000$, the ratios of equation (70) are approximately 2.5×10^3 and 1.25×10^5, respectively, and illustrate the large gains in alleviation of the secondary-diaphragm problem for the expansion tunnel.

The length z_{test} will be slightly smaller than z_2 (that is, $z_{test} = z_2 \frac{\Delta t_{test}}{\Delta t_2}$) due to the nozzle losses. However, the diaphragm bursting affects the downstream part of the test gas, and this gas is also that used in the nozzle starting process. Consequently, an imperfect diaphragm burst influences first that part of the gas considered expendable in starting the nozzle of the expansion tunnel.

Although the secondary-diaphragm bursting problem can be drastically reduced for large A, the problem is not eliminated. If the diaphragm is assumed to shatter and the resultant fragments then require acceleration to the local free-stream velocity, simple approximations show that the momentum of these fragments is not negligible compared with the momentum of the test-gas slug (that is, the mass of the test gas slug $\rho_1 z A_e$ is not orders of magnitude greater than the diaphragm mass). An experimental study (ref. 5) using poly[ethylene terephthelate] and cellophane diaphragms for $M_{s_1} \approx 3$ considers this opening problem. Since the pressure ratio across the incident and/or reflected shock waves increases with M_{s_1}, the problem for shock speeds pertinent to expansion-tunnel operation is not as severe as at $M_{s_1} \approx 3$. If the diaphragm petals are restrained so that they fold back against the wall rather than proceeding downstream, there is a possibility that the momentum lost from the stream may be reduced. Another possibility is the use of electrodynamic forces to assist the diaphragm opening.

Primary diaphragm.- The primary-diaphragm rupture problem should be mitigated by increasing $\bar{A}$ because of the smaller diameter diaphragm cross section. If the diaphragm is stressed to rupture at a certain percentage of p_4, the opening time is proportional to the diameter and will decrease with increasing $\bar{A}$ for given test-section sizes and conditions.

Tertiary diaphragm.- A third diaphragm, not present for expansion-tube operation, is located at the nozzle entrance of the expansion tunnel. However, this diaphragm does not require a perfect rupture since the accelerating gas from l_{S_2} as well as the initial part of the gas from l_{S_1} used to start the nozzle both pass the diaphragm station prior to the arrival of the gas comprising the test slug.

Driver Analysis

The driver pressure ratio p_4/p_f (fig. 12) and driver length ratio l_D/l_{S_2} (fig. 21) increase with $\bar{A}$. However, these ratios are not a true measure of the efficiency of the apparatus since for a given test-section size, the driver cross-sectional area decreases in proportion to $\bar{A}^{-1/2}$ and also for a given test time Δt_2, the length l_{S_2} decreases as $\bar{A}$ increases. A pertinent parameter which considers all these effects is the energy parameter $\bar{E}$ which is proportional to the energy required in the driver per unit test-section area, test time ($l_N = 0$), and static pressure:

$$\bar{E} \equiv \frac{E}{A_f p_f a_f \Delta t_2} \tag{71}$$

$$\bar{E} = \frac{1}{\gamma_4 - 1} \frac{p_4}{p_f} \left(1 - \frac{T_i}{T_4}\right) \frac{l_D}{l_{S_2}} \left(\bar{A} \frac{a_f \Delta t_2}{l_{S_2}}\right)^{-1} \tag{71a}$$

where

$$E = \left(\rho c_v T\right)_4 \left(1 - \frac{T_i}{T_4}\right) A_e l_D \tag{72}$$

and T_i is the initial temperature before energy addition in the driver.

Figure 23 shows the dependency of $\bar{E}$ on both M_f and $\bar{A}$ for $\gamma_4 = \frac{5}{3}$ and values of $\frac{T_4}{T_i} = \frac{T_4}{T_f}$ equal to those of figures 12 and 20. Lower values of $\bar{E}$ result as $\bar{A}$ increases at a given M_f and T_4/T_f; and the reductions become more pronounced as T_4/T_f increases. More efficient operation appears to occur for the higher T_4/T_f value at the same M_f and $\bar{A}$. Thus, when the expansion tunnel is compared with the expansion tube on the nondimensional

energy basis $\overline{E}$, the advantages of the expansion-tunnel mode of operation are very significant. This energy reduction is an important consideration for arc drivers which use capacitor bank discharges, inductive storage systems, and so forth.

Efficiency

The ideal efficiency of the expansion tunnel is defined as

$$\left.\begin{aligned} \eta_o &\equiv \frac{\text{Test-section energy}}{\text{Driver energy}} \\ \eta_o &= \frac{\left(\frac{1}{2}\,u_f^2\right)\left(\rho_f u_f A_f \Delta t_2\right)}{E} = \frac{\gamma}{2}\,\frac{M_f^3}{\overline{E}} \end{aligned}\right\} \qquad (73)$$

This efficiency is "ideal" because there are no nozzle starting losses, no scoop-off losses, and so forth considered. Figure 24 shows that although η_o decreases with M_f for fixed $\overline{A}$, it increases very significantly with $\overline{A}$ for a given M_f. For $\frac{T_4}{T_f} = 25$ and $M_f = 50$, η_o equals 0.003 for $\overline{A} = 1$, 0.025 for $\overline{A} = 100$, and 0.053 for $\overline{A} = 1000$.

If the physical dimensions of the nozzle are such that $\frac{D}{d} < \sqrt{\overline{A}}$, the nozzle entrance section must be designed to capture only that part of the gas in the accelerating chamber enclosed within a stream tube of diameter d'. (See sketch (a).)

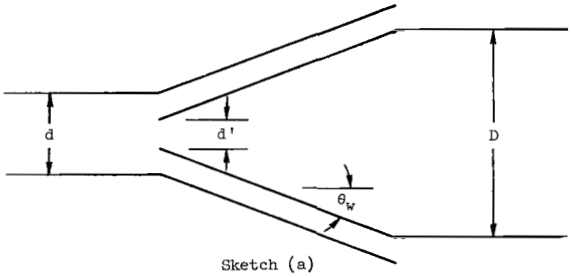

Sketch (a)

Consequently, the overall efficiency which is the product of the ideal efficiency, the nozzle starting efficiency, and the nozzle capture efficiency is

$$\left.\begin{aligned} \eta &= \eta_o \eta_{l_N} \eta_{d'} \\ \eta &= \eta_o \frac{\Delta t_{test}}{\Delta t_2} \left(\frac{d'}{d}\right)^2 \qquad \left(\frac{d'}{d} \leq 1\right) \end{aligned}\right\} \tag{74}$$

Viscous Effects

Another problem pointed out in reference 1 was the viscous effect in the accelerating chamber. One measure of the effect of viscosity is the Reynolds number based on diameter. The ratio of $N_{Re,d}$ in the accelerating chamber to $N_{Re,D}$ of the test section (which is also the Reynolds number ratio for the accelerating chambers of an expansion tunnel to that of an expansion tube for the same A_f and M_f) is

$$\left.\begin{aligned} \frac{\left(N_{Re,d}\right)_{\text{accelerating chamber}}}{\left(N_{Re,D}\right)_{\text{test section}}} &= \frac{\rho_e u_e d}{\mu_e} \frac{\mu_f}{\rho_f u_f D} \\ \text{and for } \mu \propto T^{\omega} \qquad \frac{\left(N_{Re,d}\right)_{\text{accelerating chamber}}}{\left(N_{Re,D}\right)_{\text{test section}}} &\approx (\bar{A})^{\frac{1}{2} - (\gamma-1)\omega} \frac{d}{d'} \end{aligned}\right\} \tag{75}$$

where

$$\bar{A} = \left(\frac{D}{d'}\right)^2$$

Equation (75) is plotted in figure 25 for $\omega = \frac{3}{4}$, which is a typical value for air. This figure shows small gains in the Reynolds number ratio with increasing $\bar{A}$ when $d' = d$.

Another measure of the effect of viscosity is the ratio of δ/d where δ is the boundary-layer thickness which would develop in a length l_{s_2} on a semi-infinite flat plate with an external flow equal to the flow conditions ⓔ or ⓕ; thus,

$$\frac{\delta}{d} \propto \left(\frac{l_{S_2}}{d} \frac{\mu_e}{\rho_e u_e d} \right)^{1/2} \tag{76}$$

Thus, an expansion tunnel and an expansion tube which both have the same test-section diameter D can be compared by substituting equations (2a), (39), and (75) into equation (76):

$$\frac{\left(\frac{\delta}{d}\right)_{ETun}}{\left(\frac{\delta}{D}\right)_{ET}} \approx \left[\frac{1 - M_e^{-1}}{1 - M_f^{-1}} (\bar{A})^{(\gamma-1)\left(\omega - \frac{1}{2}\right)} \frac{(\Delta t_2)_{ETun}}{(\Delta t_2)_{ET}} \left(\frac{d'}{d}\right)^2 \right]^{1/2} \tag{77}$$

and for $M_e \gg 1$, $M_f \gg 1$, and equal Δt_2,

$$\frac{\left(\frac{\delta}{d}\right)_{ETun}}{\left(\frac{\delta}{D}\right)_{ET}} \approx (\bar{A})^{\frac{\gamma-1}{2}\left(\omega - \frac{1}{2}\right)} \left(\frac{d'}{d}\right) \tag{77a}$$

In contrast to equation (75) the ratio of equation (77a) indicates a slight penalty for the expansion tunnel when judged on this basis. (See fig. 25.) Even though the diameter is reduced drastically $\left(\propto \bar{A}^{-1/2}\right)$, the unit Reynolds number is increased and the length l_{S_2} is reduced sufficiently to produce, when $d' = d$, only a small change in the δ/d ratio which is proportional to $\bar{A}^{0.05}$.

For the limiting case of $\bar{A} \gg 1$, $M_e \gg 1$, and $M_f \gg 1$, equation (76) may be put into the alternate forms:

$$\frac{\delta}{d} \propto \sqrt{\frac{l_{S_2}}{d^2} \frac{\mu_f}{\rho_f u_f}} \left(\frac{d'}{D}\right)^{1-(\gamma-1)\omega} \tag{76a}$$

$$\frac{\delta}{d} \propto \sqrt{\frac{\Delta t_2}{d^2} \frac{M_f \mu_f}{\rho_f}} \left(\frac{d'}{D}\right)^{1-(\gamma-1)\left(\omega - \frac{1}{2}\right)} \tag{76b}$$

For a given condition (f) and the same values of d, D, and either l_{S_2} or Δt_2, significant reductions in δ/d result by reducing d' (increasing $\bar{A}$). For $\gamma = 1.4$ and $\omega = 3/4$, δ/d is proportional to the 0.7 and 0.9 power of d'/d in equations (76a) and (76b), respectively. Any reduction in δ/d

resulting from decreasing d'/d is obtained at the expense of reduced nozzle capture efficiency and requires an increase in driver pressure and energy. This penalty may only be critical at maximum facility performance since excess driver capability would be available at "off-design" conditions. One must also consider the danger of transition to turbulent flow as d'/d is decreased since the Reynolds number $\frac{\rho_e u_e d}{\mu_e}$ increases. If transition occurred, the asset of a decreasing laminar ratio of δ/d with decreasing d'/d would become a turbulent liability.

Thus in regard to the viscous effects, there do not appear to be either large gains or penalties for the expansion tunnel compared with the expansion tube for $d' = d$. However, for $d' < d$, there is a possible alleviation of the viscous effects at the expense of performance capability.

Low Vacuum Considerations

Accelerating chamber.- The pressure level p_{11}/p_f in the accelerating chamber increases with $\bar{A}$ (fig. 7) and consequently reduces the low pressure requirements in this section. This reduction offers significant gains in another practical aspect for the expansion tunnel over the expansion tube. The low values of p_{11}/p_f for $\bar{A} = 1$ at high M_f may restrict the gas in state (11) to helium or hydrogen which have high sound speeds. (See ref. 1.) However, for the expansion tunnel, the level of p_{11}/p_f is raised sufficiently so that the same gas can be used both for the test gas in state (1) and the accelerating gas in state (11). Thus any diffusion of the accelerating gas back into the test gas across the interface between (e) and (21) would be particles of the same molecular species which, through collisions, should soon reach the ambient temperature of the test gas. Thus the diffusion contamination problem could be curtailed.

Another advantage of using the same gas in states (1) and (11) would be that the gas in the boundary layer on a model would consist of the correct test gas particles even before arrival of the test gas itself. Consequently, the boundary layer could probably equilibrate more rapidly to the new test gas flow condition than if it initially contained a foreign gas in state (11).

Dump tank.- For the boundary conditions of a "perfect start" for the accelerating gas, the nozzle charging pressures p_{10}/p_f required drop significantly with $\bar{A}$. (See figs. 8 and 9 and eq. (23).) However, it may be possible to raise the pressure above the p_{10} values shown and accept an initial imperfect start because the perfect start conditions produce pressures and velocities which generate upstream expansion waves in the dump tank when the accelerating-gas—test-gas interface arrives. Thus an increase in p_{10} might be tolerated with a reduced-strength dump-tank expansion wave. It is not known whether the

pressure could be raised to the point where this expansion wave had zero strength $\left(p_g = p_f\right)$ without slowing down the accelerating-gas nozzle start by an unacceptable amount.

A further consideration of the pressure p_{10} is that it does not have to meet an exact value but only an upper limit. Thus, in contrast to the expansion tube where the lowest charging pressure must be closely regulated since it determines the strength of the primary expansion wave and hence the test conditions, for the expansion tunnel only an upper limit need be set at this lowest pressure p_{10}. This condition is very desirable from an operating viewpoint.

Effect of Nozzle Configurations

General effect.- The nozzle design for expansion-tunnel operation is significantly different from that in conventional wind tunnels or shock tunnels because the entrance Mach number M_e is very large. The boundary condition of both large entrance and test-section Mach numbers requires relatively long nozzles. For example, if $M_e = 10$, the flow along the nozzle center line does not even start to expand until the distance downstream of the nozzle entrance is equal to 10 accelerating chamber radii.

If a variation in test-section Mach number is to be obtained simultaneously with no flow inclination or velocity gradient in the test section, contoured nozzles are required for all combinations of M_e and M_f. Each such nozzle would have to be corrected for viscous effects which produce both a nonuniform entrance velocity profile as well as a nozzle boundary layer. Rather than consider such a multiplicity of nozzles, the alternative of conical nozzles is treated briefly in this section with the additional restriction of uniform entrance conditions.

An effective aerodynamic area ratio $\bar{A}$ is defined as the value of $\bar{A}$ determined from equation (1) with $M_{\mathfrak{L}} = M_f$, where $M_{\mathfrak{L}}$ is the nozzle centerline Mach number. The geometric area ratio $\bar{A}_{geom}$ is the ratio of the nozzle cross-sectional areas, measured perpendicular to the nozzle axis, at the nozzle exit and entrance

$$\bar{A}_{geom} = \left(\frac{D}{d'}\right)^2 = \left(1 + \frac{2l_N}{d'} \tan \theta_w\right)^2 \tag{78}$$

Geometric and fluid mechanic parameters.- At this point three parameters are introduced and defined as (see sketch (a))

$$G \equiv \frac{l_{S_2}}{d'} \tan \theta_w \frac{\sqrt{\bar{A}} - 1}{\sqrt{\bar{A}_{geom}} - 1} \tag{79}$$

$$G_o \equiv \frac{l_{S_2}}{d} \tan \theta_w \frac{\sqrt{\bar{A}} - 1}{\sqrt{\bar{A}_{geom}} - 1} = \frac{d'}{d} G \tag{79a}$$

$$G^* \equiv \frac{l^*_{S_2}}{d'} \tan \theta_w \frac{\sqrt{\bar{A}} - 1}{\sqrt{\bar{A}_{geom}} - 1} = \frac{l^*_{S_2}}{l_{S_2}} G \tag{79b}$$

These G parameters are a combination of pure geometric factors modified to various degrees by aerodynamic factors. The parameter G_o is principally dependent on the geometry of the accelerating chamber l_{S_2}/d and nozzle wall angle; whereas the parameters G and G* are more strongly influenced by fluid-mechanic aspects. The asterisk superscript denotes critical values when the lengths l_{S_2} and l_N are such that $\Delta t_{loss} = \Delta t_2$ (i.e., $\Delta t_{test} = 0$); substitution of equation (78) into equation (79) then gives

$$G = \frac{1}{2}\left(\sqrt{\bar{A}} - 1\right)\frac{l_{S_2}}{l_N} \tag{80}$$

$$G^* = \frac{1}{2}\left(\sqrt{\bar{A}} - 1\right)\frac{l^*_{S_2}}{l_N} \tag{80a}$$

The value of G^* for the nonreflected shock tunnel with a conical nozzle is

$$G^*_{NRS} \approx \frac{\sqrt{\gamma + 1}}{(\gamma - 1)(2 - \gamma)} \left[\sqrt{\frac{2}{\gamma(\gamma - 1)}}\left(\frac{\gamma - 1}{\gamma + 1}\frac{\gamma}{2}\right)^{\frac{\gamma+1}{2(\gamma-1)}}\right]^{1/2} M_f^{\frac{2-\gamma}{\gamma-1}} \tag{81}$$

For the nonreflected shock tunnel the reference length is l_S rather than l_{S_2}. Values of G^* are plotted in figures 26(a) and 26(b). An increase in $\bar{A}$ requires an increase in G^*, values of G^* for the expansion tunnel ranging from zero at $\bar{A} = 1$ up to approximately 10 at $\bar{A} = 10^3$. For the nonreflected shock tunnel, G^* increases as $M_f^{1.5}$ (eq. (81)) and varies from 10 at $M_f = 10$ up to approximately 125 at $M_f = 50$. Note that G^* is principally a

function of $\bar{A}$ until the value of $\bar{A}$ becomes large enough to require M_e to no longer be much greater than unity. (See fig. 26(b).)

The testing time for a given configuration is simply

$$\frac{a_f \Delta t_{test}}{l_{S_2}} = \frac{a_f \Delta t_2}{l_{S_2}} \left(1 - \frac{G^*}{G}\right) = \frac{a_f \Delta t_2}{l_{S_2}} \left(1 - \frac{G^*}{G_o} \frac{d'}{d}\right) \tag{82}$$

This test time parameter is shown in figure 27 at values of G of 10, 100, and ∞ for the expansion tunnel and at these three values of G and also at G = 200 for the nonreflected shock tunnel. For $\bar{A} = 10^3$, G = 10 results in a substantial reduction in test time with increasing M_f, and in fact Δt_{test} approaches 0 at $M_f \approx 40$. (See fig. 26.) The penalty for $\bar{A} = 10^3$ is reduced to only about 10 percent at $G \approx 100$. (See fig. 27.) When $\bar{A} = 10^2$, the G = 10 case shows approximately 50 percent penalty; and for G = 100, the reduction is 5 percent.

The shock tunnel is more sensitive to low values of G with larger penalties in test time, the latter vanishing at $M_f \approx 9$ for G = 10 and $M_f \approx 43$ for G = 100.

The test time parameter $\frac{a_f \Delta t_{test}}{l_{S_2}}$ depends principally on M_f and $\bar{A}$ for $M_f \gg 1$, $\bar{A} \gg 1$, and $\frac{l_N}{l_{S_2}}$ of order of 1. The relation of $\frac{a_f \Delta t_{test}}{l_{S_2}}$ to various other expansion-tube parameters is illustrated by the following set of approximate equations. The second term on the right-hand side is the correction for the case when $M_e \not\gg 1$.

$$M_f^2 \frac{a_f \Delta t_{test}}{l_{S_2}} \approx (\bar{A})^{\frac{\gamma-1}{2}} + \frac{1}{M_f}(\bar{A})^{\gamma-1} - \frac{2}{2-\gamma} \frac{l_N}{l_{S_2}} + \ldots \tag{83a}$$

$$M_f^2 \frac{a_f \Delta t_{test}}{l_{S_2}} \approx (\bar{A})^{\frac{\gamma-1}{2}} + \frac{1}{M_f}(\bar{A})^{\gamma-1} - \frac{1}{2-\gamma} \frac{\sqrt{\bar{A}}}{G} + \ldots \tag{83b}$$

$$M_f^2 \frac{a_f \Delta t_{test}}{l_{S_2}} \approx \left(2G \frac{l_N}{l_{S_2}}\right)^{\gamma-1} + \frac{1}{M_f}\left(2G \frac{l_N}{l_{S_2}}\right)^{2(\gamma-1)} - \frac{2}{2-\gamma} \frac{l_N}{l_{S_2}} + \ldots \tag{83c}$$

$$M_f^2 \frac{a_f \Delta t_{test}}{l_{S_2}} \approx \left(2G_o \frac{d}{d'} \frac{l_N}{l_{S_2}}\right)^{\gamma-1} + \frac{1}{M_f}\left(2G_o \frac{d}{d'} \frac{l_N}{l_{S_2}}\right)^{2(\gamma-1)} - \frac{2}{2-\gamma} \frac{l_N}{l_{S_2}} + \cdots \tag{83d}$$

$$M_f^2 \frac{a_f \Delta t_{test}}{l_{S_2}} \approx (\bar{A})^{\frac{\gamma-1}{2}} + \frac{1}{M_f}(\bar{A})^{\gamma-1} - \frac{1}{2-\gamma} \frac{D}{l_{S_2}} \frac{1}{\tan \theta_w} + \cdots \tag{83e}$$

$$M_f^2 \frac{a_f \Delta t_{test}}{l_{S_2}} \approx \left(2 \frac{l_N}{d'} \tan \theta_w \frac{\sqrt{\bar{A}} - 1}{\sqrt{\bar{A}_{geom} - 1}}\right)^{\gamma-1} + \frac{1}{M_f}\left(2 \frac{l_N}{d'} \tan \theta_w \frac{\sqrt{\bar{A}} - 1}{\sqrt{\bar{A}_{geom} - 1}}\right)^{2(\gamma-1)} - \frac{2}{2-\gamma} \frac{l_N}{d'} \frac{d'}{d} \frac{d}{l_{S_2}} + \cdots \tag{83f}$$

$$M_f^2 \frac{a_f \Delta t_{test}}{l_{S_2}} \approx \left(2 \frac{l_N}{l_{S_2}} \frac{l_{S_2}}{d} \frac{d}{d'} \tan \theta_w \frac{\sqrt{\bar{A}} - 1}{\sqrt{\bar{A}_{geom} - 1}}\right)^{\gamma-1} + \frac{1}{M_f}\left(2 \frac{l_N}{l_{S_2}} \frac{l_{S_2}}{d} \frac{d}{d'} \tan \theta_w \frac{\sqrt{\bar{A}} - 1}{\sqrt{\bar{A}_{geom} - 1}}\right)^{2(\gamma-1)} - \frac{2}{2-\gamma} \frac{l_N}{l_{S_2}} + \cdots \tag{83g}$$

$$M_f^2 \frac{a_f \Delta t_{test}}{l_{S_2}} \approx \left(\sqrt{\frac{\bar{A}}{\bar{A}_{geom}}} \frac{D}{l_{S_2}} \frac{l_{S_2}}{d} \frac{d}{d'}\right)^{\gamma-1} + \frac{1}{M_f}\left(\sqrt{\frac{\bar{A}}{\bar{A}_{geom}}} \frac{D}{l_{S_2}} \frac{l_{S_2}}{d} \frac{d}{d'}\right)^{2(\gamma-1)} - \frac{1}{2-\gamma} \frac{D}{l_{S_2}} \frac{1}{\tan \theta_w} + \cdots \tag{83h}$$

If the effect of $\overline{A} \neq \overline{A}_{geom}$ is neglected and $M_e \gg 1$, these equations indicate that $M_f^2 \frac{a_f \Delta t_{test}}{l_{S_2}}$ will increase when

(a) $\overline{A}$ increases for fixed l_N/l_{S_2},

(b) l_N/l_{S_2} decreases for fixed $\overline{A}$,

(c) G increases for fixed $\overline{A}$ or l_N/l_{S_2},

(d) d'/d decreases, and

(e) θ_w increases..

These gains in test time would be modified somewhat if consideration were given to the relation between $\overline{A}$ and $\overline{A}_{geom}$, the indicated beneficial effect due to increasing θ_w (eqs. (83e) to (83h)) probably suffering the largest reduction. Note for positive test times that the maximum ratio of d'/d is specified by equations (83) for given values of l_N, l_{S_2}, θ_w, D, and d. It may also be expressed as a function of G_o and G^* (by using eq. (82)) as

$$\frac{d'}{d} \leq \frac{G_o}{G^*} \qquad \left(G_o \leq G^* \text{ or } \frac{d'}{d} = 1 \text{ for } \frac{G_o}{G^*} > 1\right)$$

The parameter G_o is limited by the physical operating conditions of the apparatus. Because of attenuation or other various reasons, the factor l_{S_2}/d will usually be less than 200. Values of $\tan \theta_w$ will probably be close to 0.1, although a value of 0.2 might be acceptable for some uses. The third component term of G_o, $\frac{\sqrt{\overline{A}} - 1}{\sqrt{\overline{A}_{geom}} - 1}$, is a function of M_e, θ_w, and the distance downstream from the nozzle entrance. This term has a value of zero at the entrance and maintains this value until the first characteristic wave from the nozzle entrance reaches the center line. The term will then increase in value with distance and reach a maximum appreciably in excess of unity, and thereafter decreases toward the asymptotic conical nozzle value near unity. Thus a typical value for G_o might be 20.

The test-section size must also be considered since practical aspects prohibit the use of very large test-section diameters. Consequently, the range of the ratio of D/d will be bounded and, as a result, very large values of $\overline{A}$ can be obtained only at the expense of decreasing d'/d.

Growth of the nozzle boundary layer for the rather low Reynolds numbers of the nozzle is also a factor for consideration. However, only fairly small effective nozzle half-angles are required. Consequently, at first glance the problem appears to be principally one of correcting for the effect of $d\delta^*/d\xi$ at small ξ, and then at a larger ξ expanding further, if necessary, to assure a potential "core" at the test section. This low Reynolds number nozzle problem will require additional study before its full effect can be determined.

Example

A numerical example, illustrating the discussions in the foregoing paragraphs, is solved with the assumptions: (a) $\frac{l_{S_2}}{d} = 150$, (b) $\frac{D}{d} = 10$, (c) $G_o = 20$, and (d) $\bar{A} = \bar{A}_{geom}$. Equation (82) may then be rewritten as

$$\frac{a_f \Delta t_{test}}{D} = \frac{a_f \Delta t_2}{l_{S_2}} \left(\frac{l_{S_2}}{d} \right) \left(\frac{d}{D} \right) \left(1 - \frac{G^*}{G_o} \frac{1}{\sqrt{\bar{A}}} \sqrt{\frac{\bar{A}}{\bar{A}_{geom}}} \frac{D}{d} \right) \tag{84}$$

$$\frac{a_f \Delta t_{test}}{D} = 15 \frac{a_f \Delta t_2}{l_{S_2}} \left(1 - \frac{1}{2} \frac{G^*}{\sqrt{\bar{A}}} \right) \tag{84a}$$

Equation (84) is in a form which permits evaluation and comparison on a test-section-diameter basis which is significant when considering large $\bar{A}$. The variation of $\frac{a_f \Delta t_{test}}{D}$ with M_f is shown in figure 28. Since $\frac{d'}{d} = 10\bar{A}^{-1/2}$, no curves are drawn for $\bar{A}$ less than 100. The gains with increasing $\bar{A}$ of Δt_{test} are larger when compared on a common test-section-diameter basis (fig. 28) than on a common accelerating-chamber-length basis. (See fig. 27.) This statement is not universally valid but applies under the previous restrictions (a) to (d).

Equation (83e) may be rewritten for $M_e \gg 1$ as

$$\frac{a_f \Delta t_{test}}{D} = \frac{1}{M_f^2} \left(\frac{l_{S_2}}{d} \frac{d}{D} \bar{A}^{\frac{\gamma-1}{2}} - \frac{1}{2 - \gamma} \frac{1}{\tan \theta_w} \right) \tag{85}$$

Examination of equation (85) reveals the reason that the shock tunnel (operating at very large $\bar{A}$) has a higher value of $\frac{a_f \Delta t_{test}}{D}$ than the expansion tunnel

for which curves are drawn only for $\bar{A} \leqq 10^3$. Evaluation of $\frac{a_f \Delta t_{test}}{D}$ from equation (84), with the corresponding $\bar{A}(M)$ of the shock tunnel, will not produce an answer in agreement with the shock-tunnel curve for two reasons. The first is that the assumption $M_e \gg 1$ is violated when M_e approaches M_2, and this violation introduces an error which results in the first term of equation (84) being low by a factor of 5.6. Even if this correction factor were taken into account, the expansion tunnel with $M_e = M_2$ would not have the same value of $\frac{a_f \Delta t_2}{D}$ as the shock tunnel at the same M_f and $\bar{A}$. Instead $\left(\frac{a_f \Delta t_2}{D}\right)_{ETun}$ would be greater than $\left(\frac{a_f \Delta t_2}{D}\right)_{NRS}$ by the factor of 6.74 which is $\left(\frac{l_{S_1}}{l_{S_2}}\right)_{M_e=M_2}$. This variance should not be interpreted to mean $\Delta t_{ETun} > \Delta t_{NRS}$ because $\left(\frac{l_{S_2}}{D}\right)_{ETun}$ was assumed to be equal to $\left(\frac{l_S}{D}\right)_{NRS}$, whereas the overall length $l_{S_1} + l_{S_2}$ of the expansion tunnel is $7.74 l_{S_2}$. Consequently, if a comparison were to be made on a total length basis, $(\Delta t_2)_{ETun}$ would be equal to $\frac{6.74}{7.74} = 0.87(\Delta t_2)_{NRS}$. This answer is different from unity only because by the definition of $(\Delta t_2)_{ETun}$, gas in condition (21) is not included; yet for $M_e = M_2$, state (1) = state (11) and state (2) = state (e) = state (21). Consequently, if this gas in state (21) were also used, the times for the two apparatus would then be equal.

The overall efficiency for this particular example may be expressed as

$$\eta = \eta_o \left(1 - \frac{1}{2} \frac{G^*}{\sqrt{\bar{A}}}\right) \frac{100}{\bar{A}} \tag{86}$$

At $M_f = 50$, the values of η are 0.019, 0.0070, and 0.0044 for $\bar{A} = 100$, 500, and 1000, respectively. Thus the nozzle capture losses more than offset the gains in η_o (fig. 24) with increasing $\bar{A}$, and the most efficient operating point for this example is the value of $\bar{A}$ such that $d' = d$ $(\bar{A} = 100)$. Note that the expansion tube $(\bar{A} = 1)$ has an ideal efficiency of only 0.003 for $M_f = 50$.

Since η_o was not computed for the nonreflected shock tunnel, the exact value of η cannot be found. However, since the nozzle capture efficiency at

$M_f = 50$ is approximately $\frac{100}{\bar{A}} \approx 10^{-4}$, it is obvious that the overall efficiency is well below the expansion-tunnel values.

Design Details

The design of the conical nozzles is an important problem area where a study that uses the method of characteristics has been underway for an extended period. The general results of this study are not included here but one particular case is illustrated in figures 29 and 30. The entrance Mach number is 10 and the primary nozzle angle θ_w is 5.3°. In an effort to reduce the nozzle lengths l_N, the use of compound or multiple nozzles has also been considered. This latter scheme, similar to that used in shock tunnels (refs. 2 and 6), is shown in sketch (b). The curves of figure 29 show the center-line Mach number distribution as a function of l_N/d for both the simple nozzle and the compound nozzle with the imbedded nozzle lips located at $\frac{\xi}{d} = 12$. This imbedded nozzle has an entrance radius equal to $0.37d'$ and a wall angle of 5.6° The compound nozzle arrangement is successful in shortening the nozzle for a given M_f (for example, $M_f = 40$ at $\frac{l_N}{d} = 40$ for a compound nozzle and at $\frac{l_N}{d} = 75\frac{1}{2}$ for a simple nozzle). However, this reduction in l_N is obtained at the expense of test-section gradients as shown by the radial distribution of flow angle and Mach number in figure 30.

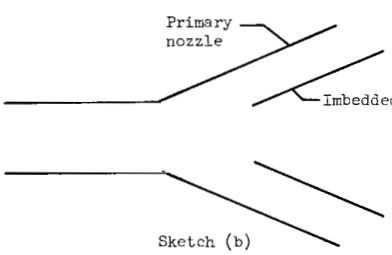

Sketch (b)

The velocity variation is negligible since the Mach number variation is almost entirely due to changes in the speed of sound. Values of θ for source flow with virtual origins at the nozzle entrances indicate that the flow inclination is slightly worse than that of source flow. For radiation experiments where the important contributions arise at the model surfaces most normal to the free stream, the variation in θ would probably not be important.

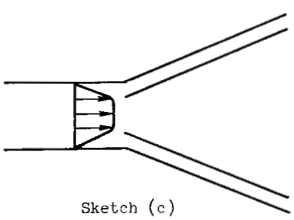
Sketch (c)

A practical nozzle configuration might also include a boundary-layer scoop at the entrance section to obtain a more uniform entering velocity profile. (See sketch (c).) The trade-off in nozzle performance against this increased complexity has not been explored.

Critical Lengths

Accelerating-chamber critical length.- Since operation over a range of M_f and $\bar{A}$ is desirable and the values of d and D are generally fixed, the

nozzle capture diameter d' will probably be the variable parameter of an actual expansion tunnel. This variation is easily accomplished; for example, a reduction in d' results from a slight forward extension to the nozzle section. Thus the "constant" component dimensions are l_N and D. Expressions relating the critical acceleration-chamber length $l^*_{S_2}$ for which the test time vanishes to these components may be obtained from equations (78), (79), and (80). Thus,

$$\frac{l^*_{S_2}}{l_N} = \frac{2G^*}{\sqrt{\bar{A}} - 1} \approx \frac{2G^*}{\sqrt{\bar{A}}} \tag{87}$$

$$\frac{l^*_{S_2}}{D} = \frac{1}{\tan \theta_w} \frac{\sqrt{\bar{A}_{geom}} - 1}{\sqrt{\bar{A}} - 1} \frac{G^*}{\sqrt{\bar{A}_{geom}}} \approx \frac{1}{\tan \theta_w} \frac{G^*}{\sqrt{\bar{A}}} \tag{88}$$

From figure 26 at $M_f = 50$, $\frac{G^*}{\bar{A}} \approx 0.32$ and $\frac{G^*}{\bar{A}} \approx 0.47$ for $\bar{A} = 10^3$ and $\bar{A} = 10^2$, respectively. Consequently, for these cases $\frac{l^*_{S_2}}{l_N} \approx 0.64$ and 0.94; and $\frac{l^*_{S_2}}{D} \approx 3.2$ and 4.7 (for $\tan \theta_w = 0.1$). The critical accelerating-chamber length is not excessive; therefore, practical lengths for l_{S_2} do not result in large percentage of losses in test time. If in the cases above $l_{S_2} \approx 150d \approx 15D$, the test-time percentage loss is $\frac{l^*_{S_2}}{l_{S_2}} \approx \frac{3}{15} \approx 20$ percent for $\bar{A} = 10^3$.

Dump-tank length.- From equation (65) and figures 19(a) and 19(b), it is evident that the ratio l_{S_R}/l_{S_2} increases with increasing $\bar{A}$. Such an increase is not a true penalty for expansion-tunnel operation because of the increased testing time available. For example, by combining equations (65), (39), (3a), and (1a), the following relation may be found:

$$\frac{l_{S_R}}{a_f \Delta t_2} \approx \frac{\gamma_{10}^2 - 1}{3\gamma_{10} - 1} \frac{2}{\gamma_{11} + 1} \left(\frac{\gamma_{11} + 1}{1 + \frac{2}{\gamma_{11} - 1} \frac{1}{M_{30}^2}} \right)^{1/2} M_f \left[1 + \frac{\gamma_{11} - 1}{2} (\bar{A})^{-\frac{\gamma - 1}{2}} \right] \tag{89}$$

Consequently, on a unit test time basis, l_{S_R} actually decreases with $\bar{A}$. Of course, to utilize fully the expansion-tunnel capabilities the ratios for l_{S_R}/l_{S_2} of equation (65) should be maintained.

RÉSUMÉ

The perfect-gas analysis of this report has covered many facets of expansion-tunnel operation. The more important advantages and disadvantages of the expansion tunnel compared with the expansion tube are as follows:

Advantages:

(1) The zero-nozzle-length test time $\left(a_f \Delta t_2 / l_{S_2}\right)$ per unit length is increased. The time lost in the starting and stopping processes of the nozzle is, in general, only a small fraction of this time Δt_2 for ratios of nozzle length l_N to accelerating-chamber length l_{S_2} less than 1/2 and for large area ratios $\bar{A}$.

(2) The usable test slug length prior to secondary-diaphragm rupture increases rapidly with $\bar{A}$ and is roughly proportional to $\bar{A}^{\frac{\gamma+1}{2}}$ at high test-section Mach number M_f.

(3) The secondary-diaphragm bursting problem is greatly reduced.

(4) The nondimensional energy parameter $E/A_f p_f a_f \Delta t_2$ decreases with increasing $\bar{A}$. Thus the expansion tunnel is especially suited to arc-heated drivers. The ideal efficiency also increases with $\bar{A}$.

(5) The primary diaphragm is of smaller diameter for the same test-section area A_f and consequently this bursting problem is also reduced.

(6) The low pressure in the accelerating chamber p_{11} is significantly higher. As a consequence, either the pumping capacity could be reduced and/or the same gas as the test gas might be used to reduce interface mixing effects.

(7) The dump-tank length parameter $l_{S_R}/a_f \Delta t_2$ is reduced.

(8) Viscous effects may be reduced for nozzle entrance diameter less than accelerating-chamber diameter ($d' < d$).

Disadvantages:

(1) Fairly long nozzles are required. The (theoretical) expansion tube flexibility of variable Mach number M_f without nozzle changes is lost. However, conical nozzles might be employed to regain this flexibility with small flow gradients. The effect of nozzle boundary-layer growth must also be considered.

(2) The ratio of driver pressure to test-section pressure p_4/p_f is increased.

(3) The ratio of the minimum charging pressure in the dump tank to the test-section pressure p_{10}/p_f is decreased and thus requires increased pumping capacity.

(4) A third diaphragm is added to apparatus.

(5) The length parameters l_D/l_{S_2}, l_{S_1}/l_{S_2}, and l_{S_R}/l_{S_2} all increase with $\bar{A}$ as well as $l_{S_1}/a_f\Delta t_2$ and $l_D/a_f\Delta t_2$ where l_D is the driver length, l_{S_1}, the intermediate-chamber length, l_{S_R}, the dump-tank length, and a_f is speed of sound in test section. However, for large M_f, the length l_{S_2} is still by far the predominant length as long as $\bar{A} > 10^3$.

In the opinion of the authors, the advantages of the expansion tunnel appear, particularly in the light of practical operating problems, to outweigh the disadvantages.

Langley Research Center,
National Aeronautics and Space Administration,
Langley Station, Hampton, Va., February 2, 1965.

REFERENCES

1. Trimpi, Robert L.: A Preliminary Theoretical Study of the Expansion Tube, a New Device for Producing High-Enthalpy Short-Duration Hypersonic Gas Flows. NASA TR R-133, 1962.

2. Hertzberg, A.; Smith, W. E.; Glick, H. S.; and Squire, W.: Modifications of the Shock Tube for the Generation of Hypersonic Flow. AEDC-TN-55-15 (AD-789-A-2), Arnold Eng. Dev. Center, Mar. 1955.

3. Ames Research Staff: Equations, Tables, and Charts for Compressible Flow. NACA Rept. 1135, 1953. (Supersedes NACA TN 1428.)

4. Glick, H. S.; Hertzberg, A.; and Smith, W. E.: Flow Phenomena in Starting a Hypersonic Shock Tunnel. Rept. No. AD-789-A-3 (AEDC-TN-55-16), Cornell Aero. Lab., Inc., Mar. 1955.

5. Knoos, Stellan: A Theoretical and Experimental Study of the Opening of the Low-Pressure Diaphragm in a Double-Diaphragm Shock Tube. Thesis, Roy. Inst. of Technol. (Stockholm), 1963.

6. Hertzberg, A.: The Shock Tunnel and Its Applications to Hypersonic Flight. Rep. No. AD-1052-A-5 (AFOSR-TN-57-268, AD-126567), Cornell Aero. Lab., Inc., June 1957.

TABLE I.- INDEX TO FIGURES

TABLE I.- INDEX TO FIGURES - Concluded

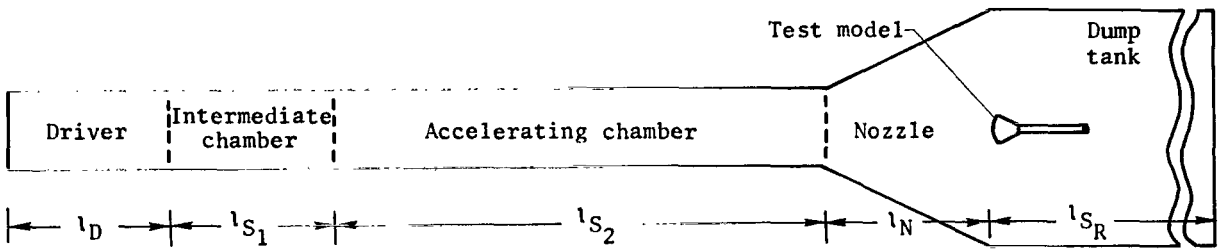

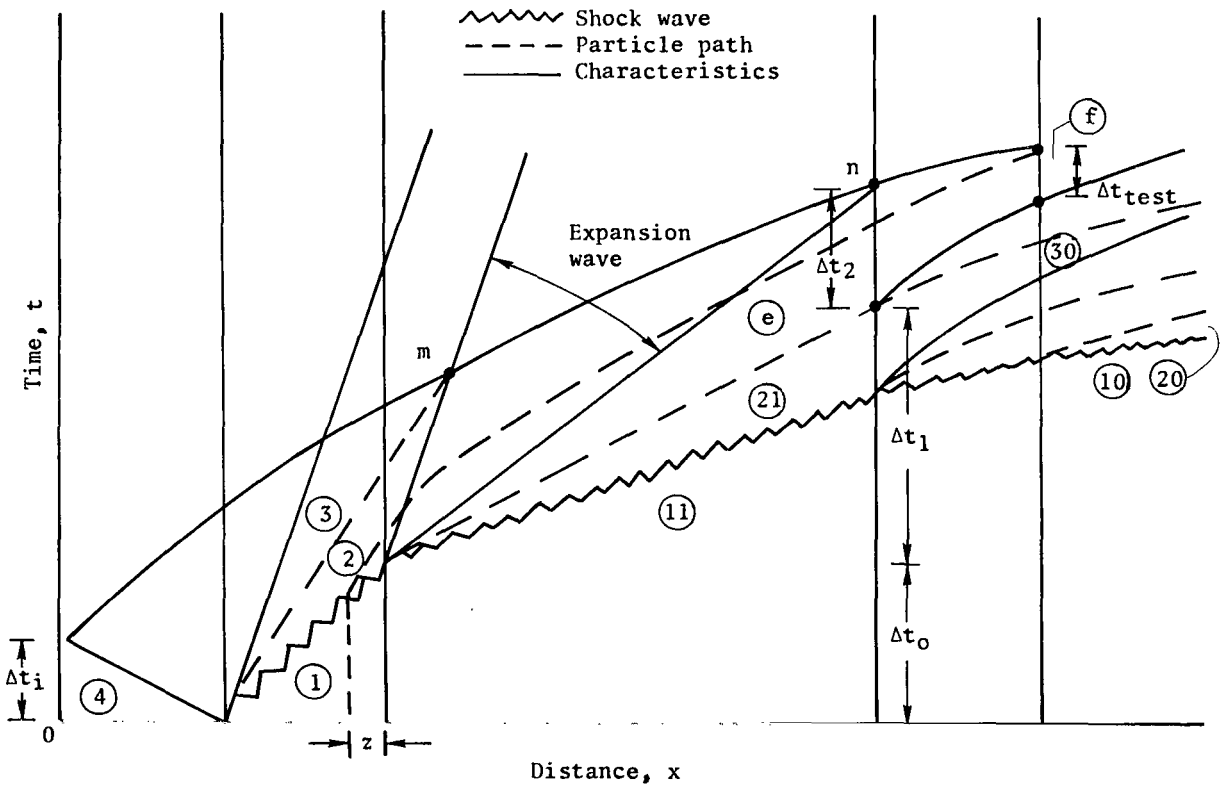

Figure I.- Schematic and wave diagram for expansion tunnel.

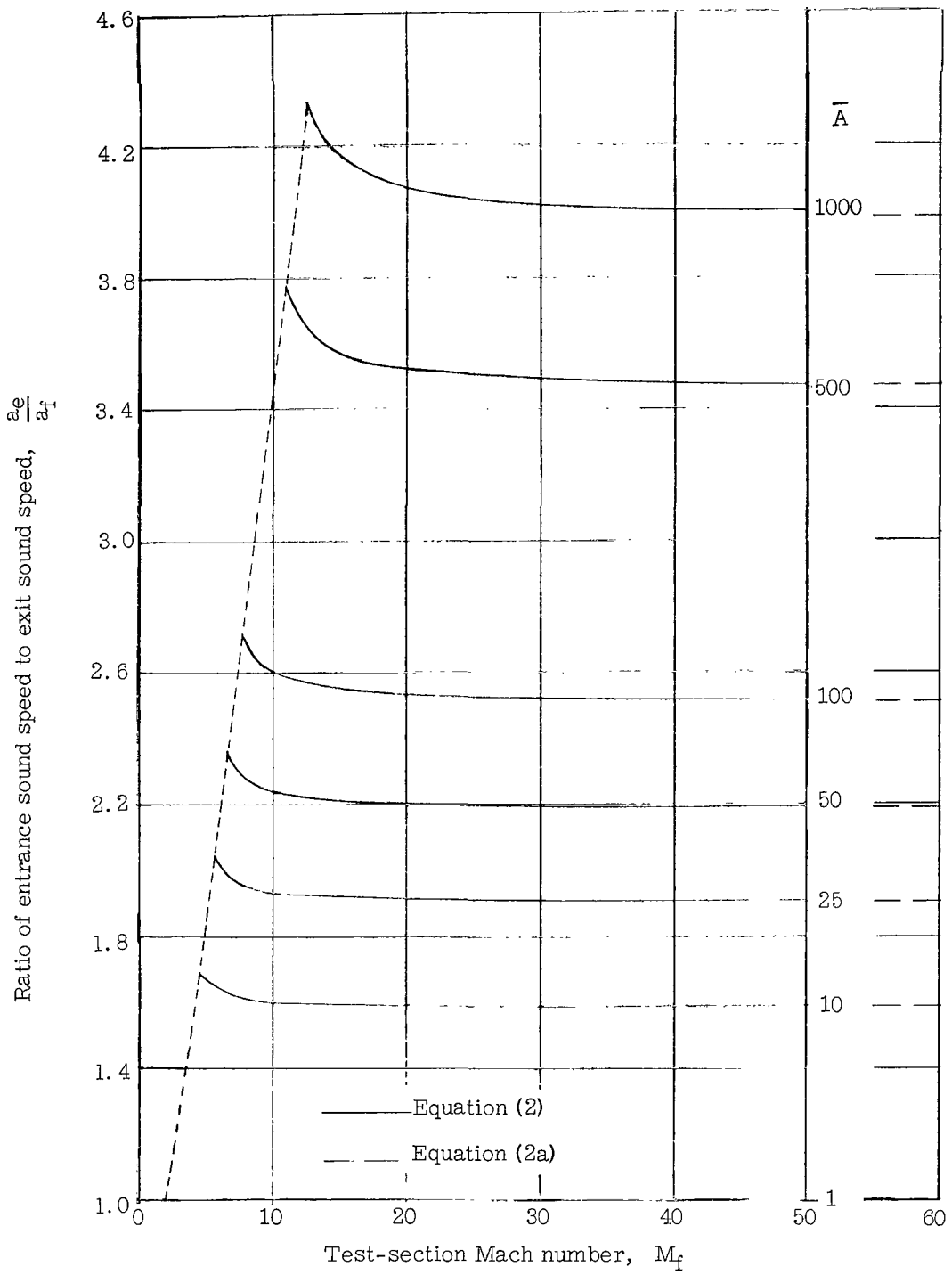

(a) Speed-of-sound ratio.

Figure 2.- Variation of conditions at nozzle entrance with test-section Mach number.

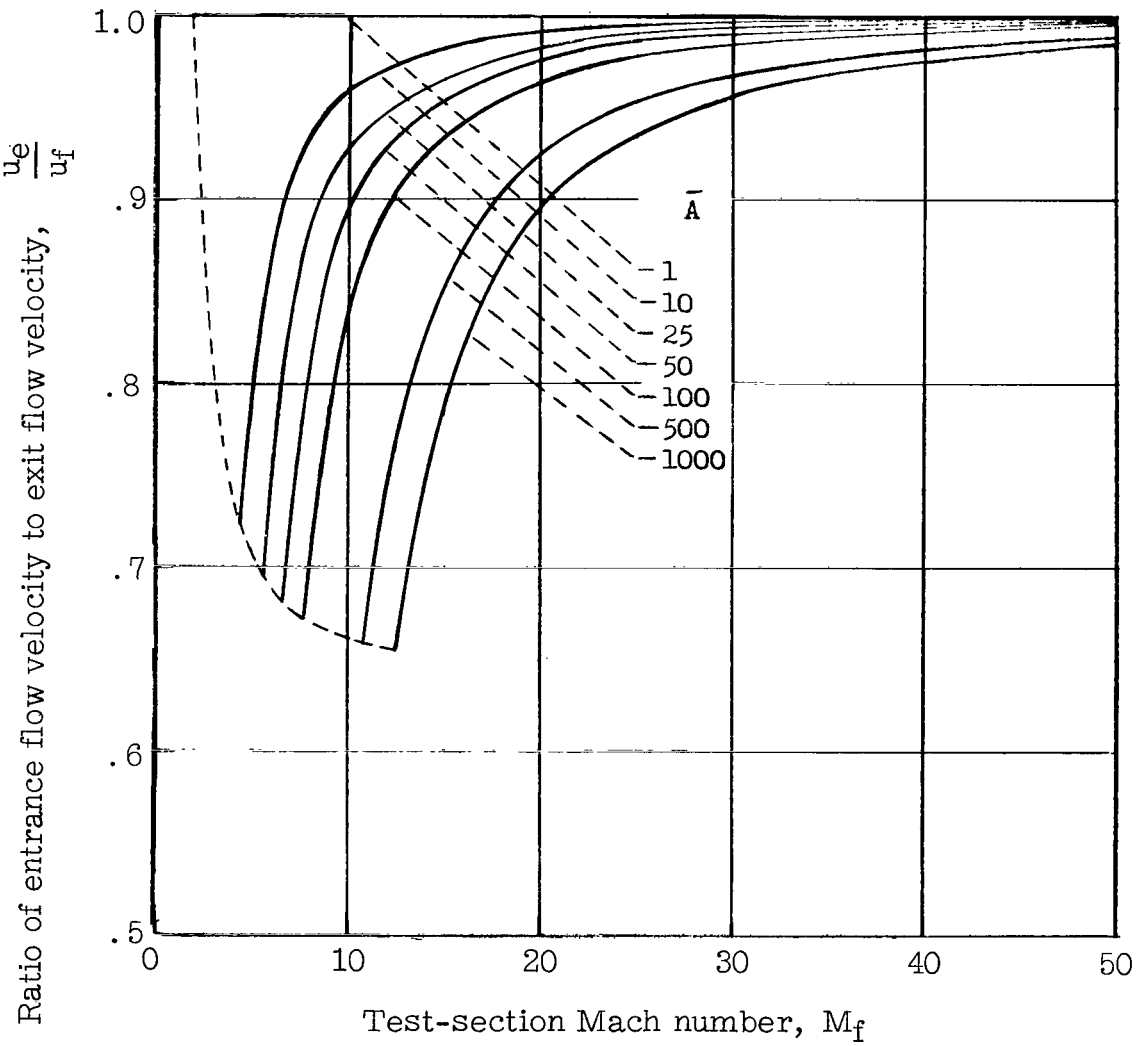

(b) Flow-velocity ratio.

Figure 2.- Continued.

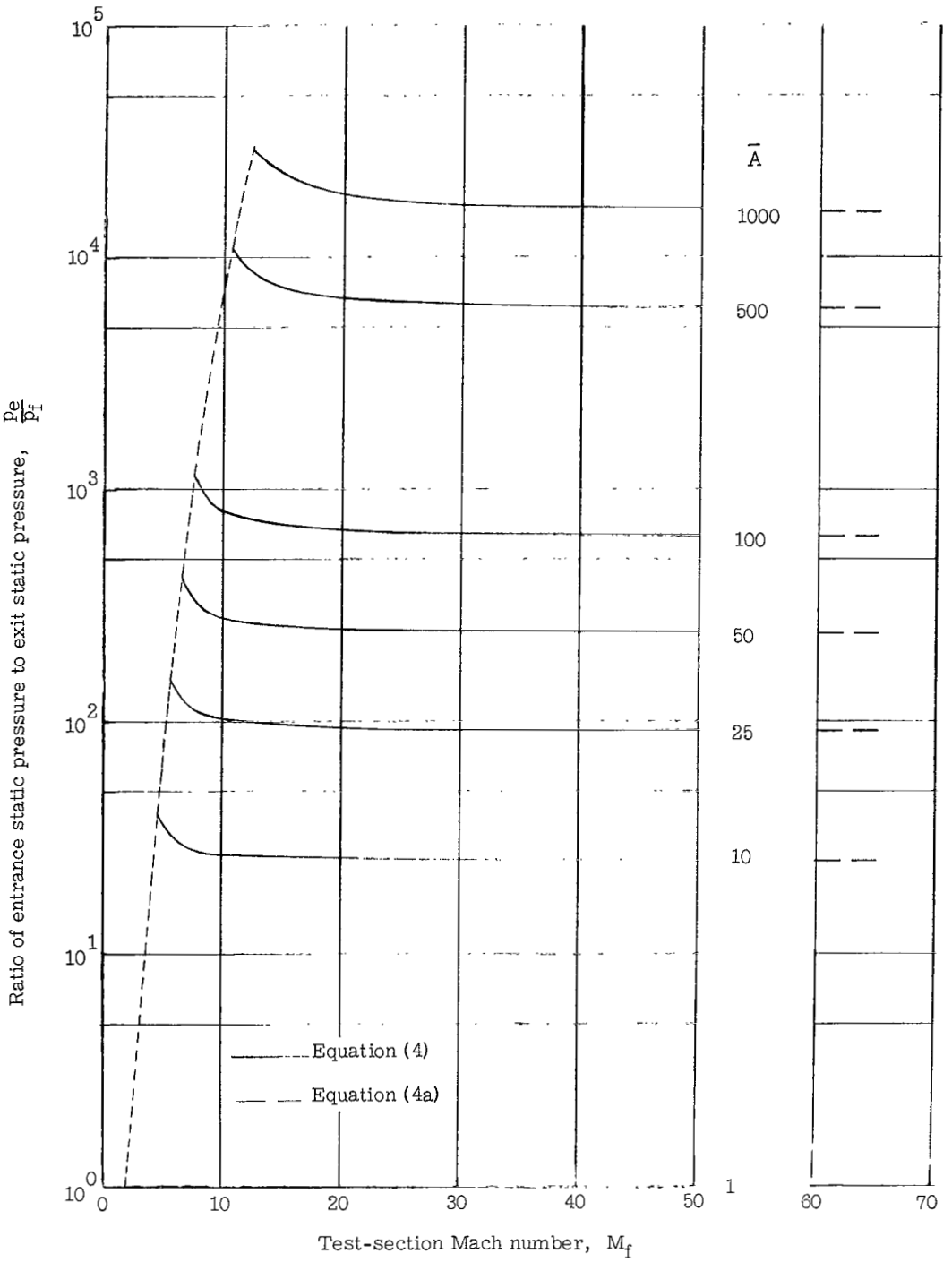

(c) Static-pressure ratio.

Figure 2.- Continued.

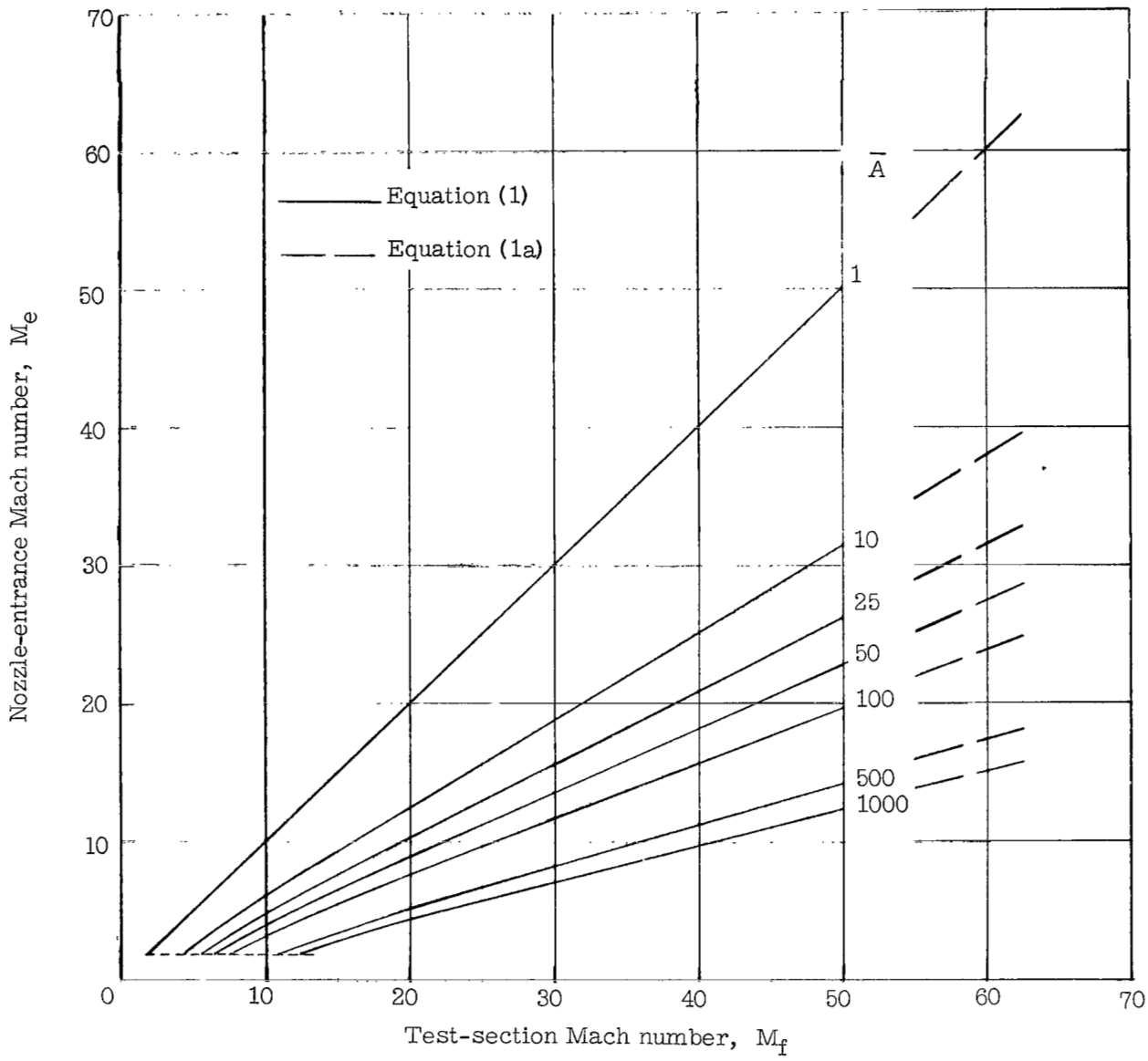

(d) Nozzle-entrance Mach number.

Figure 2.- Concluded.

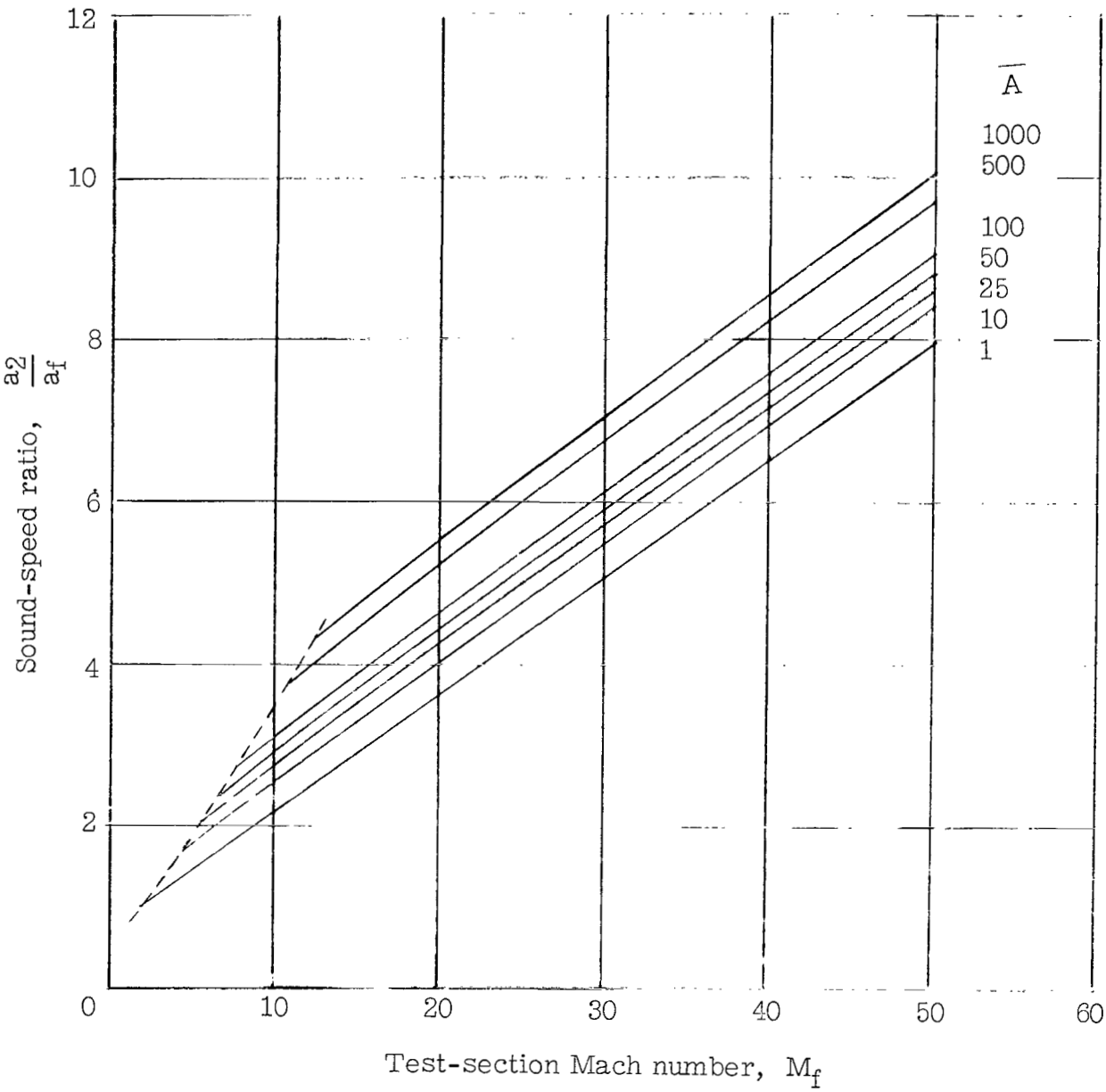

(a) Speed-of-sound ratio.

Figure 3.- Variation of conditions in region ② with test-section Mach number.

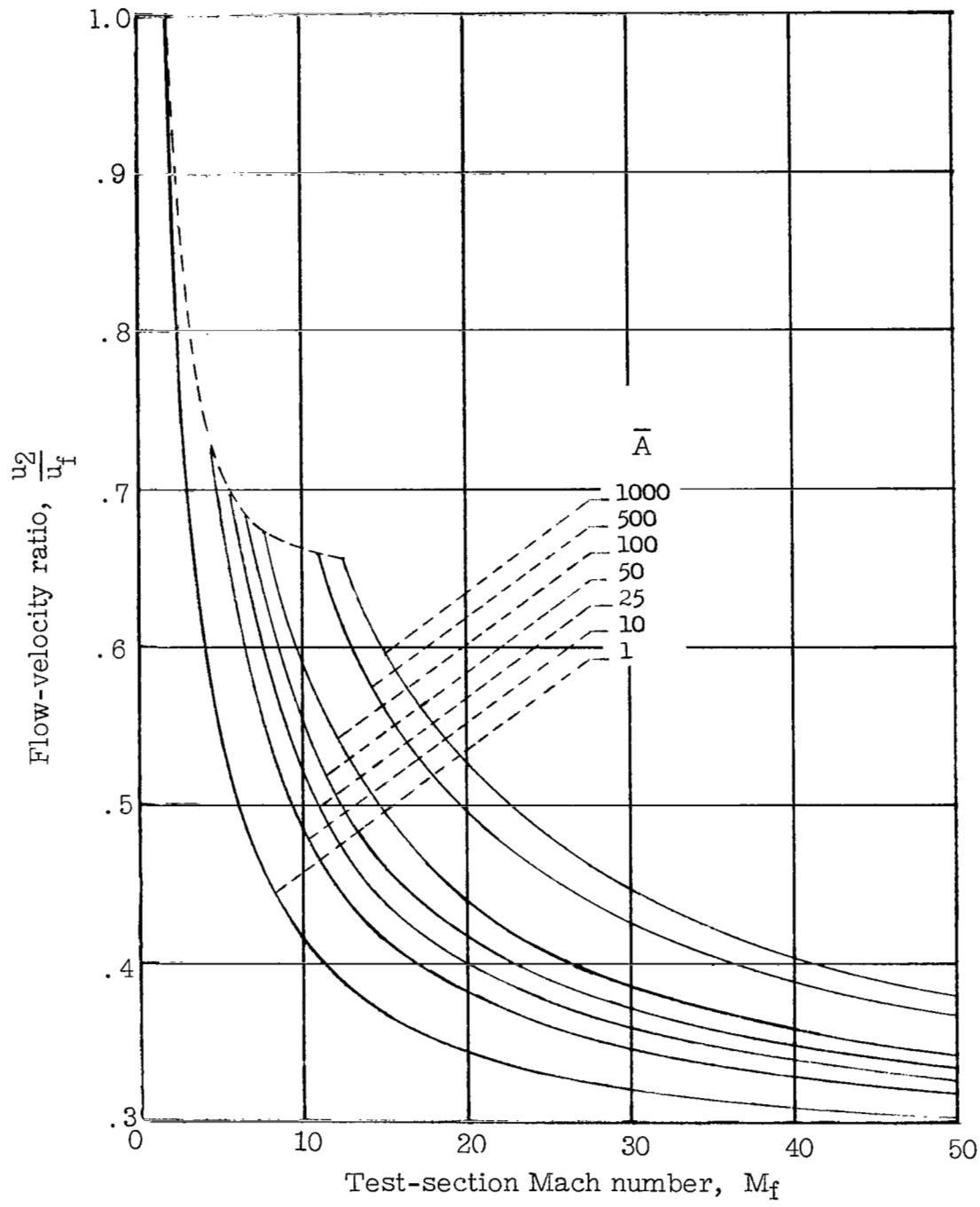

(b) Flow-velocity ratio.

Figure 3.- Continued.

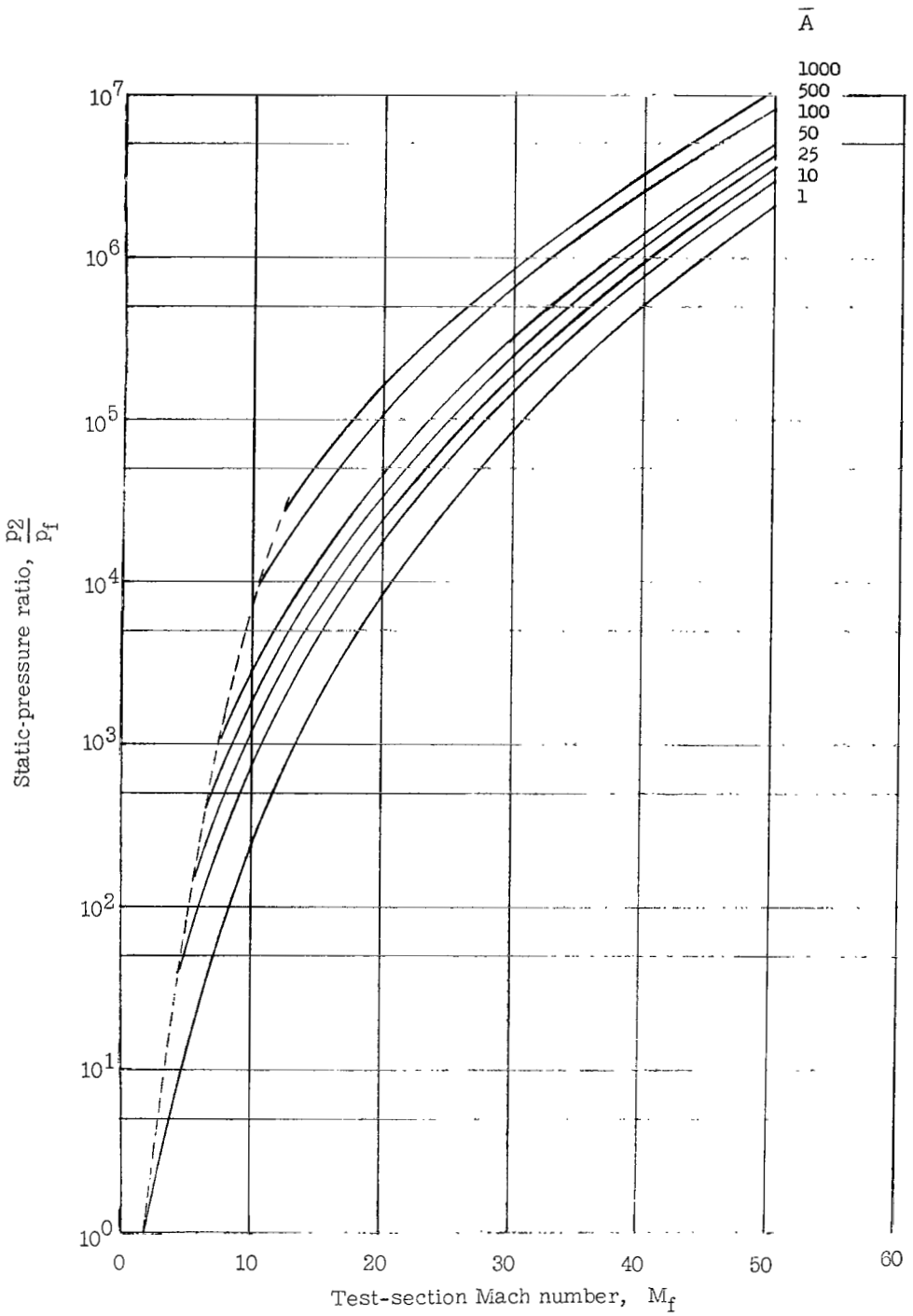

(c) Static-pressure ratio.

Figure 3.- Continued.

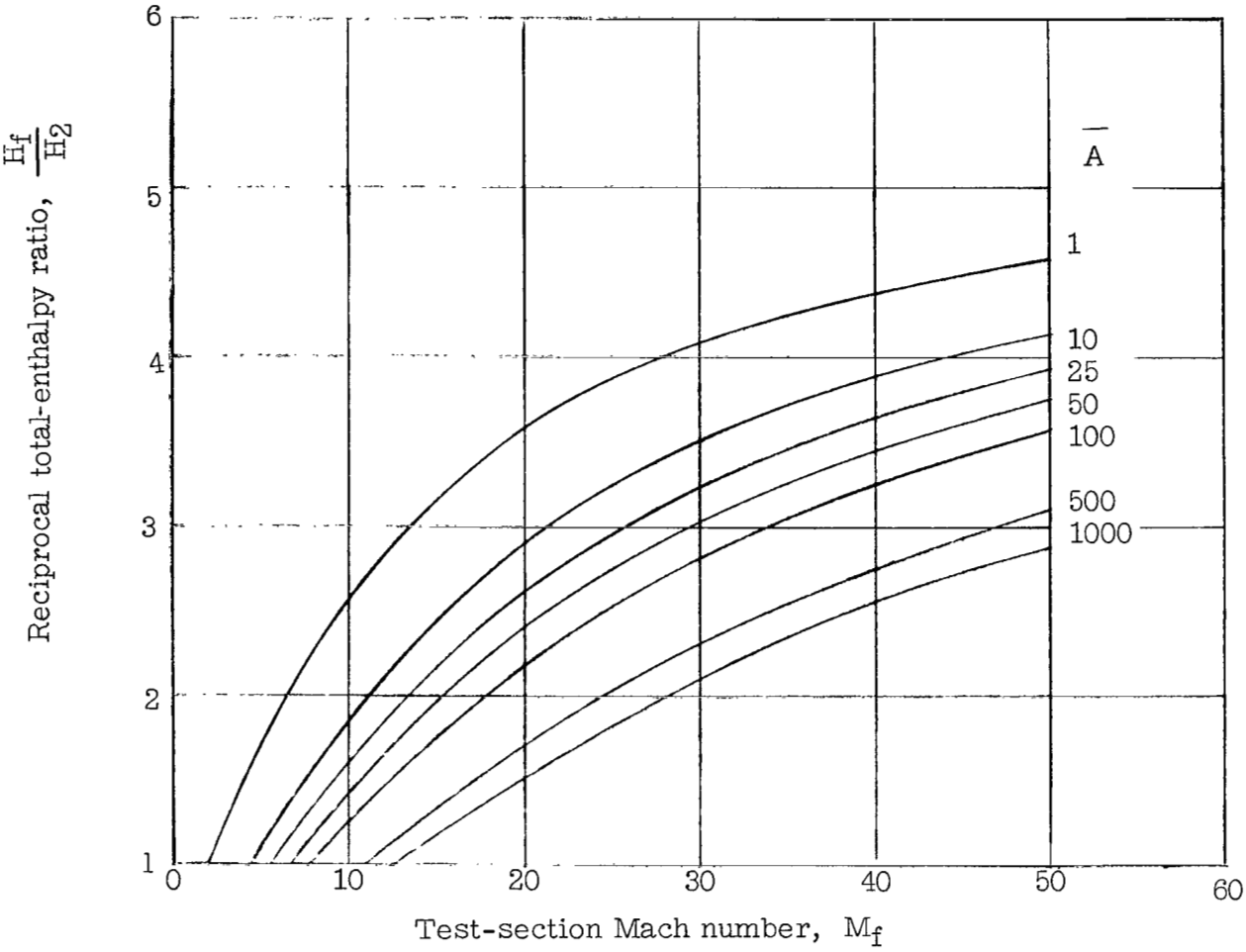

(d) Reciprocal total-enthalpy ratio.

Figure 3.- Concluded.

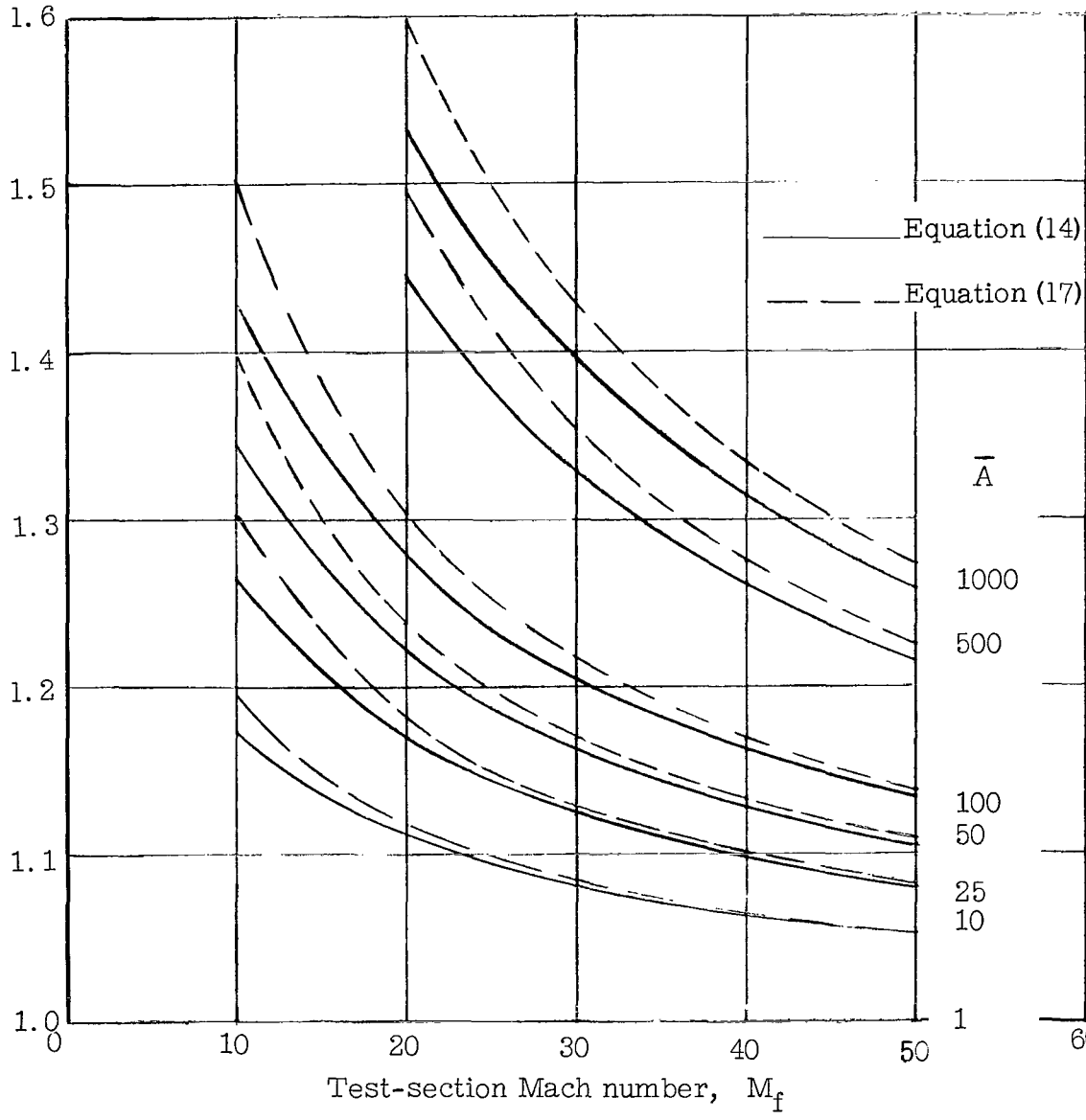

(a) Mach number.

Figure 4.- Variation of parameter β with Mach number and area ratio.

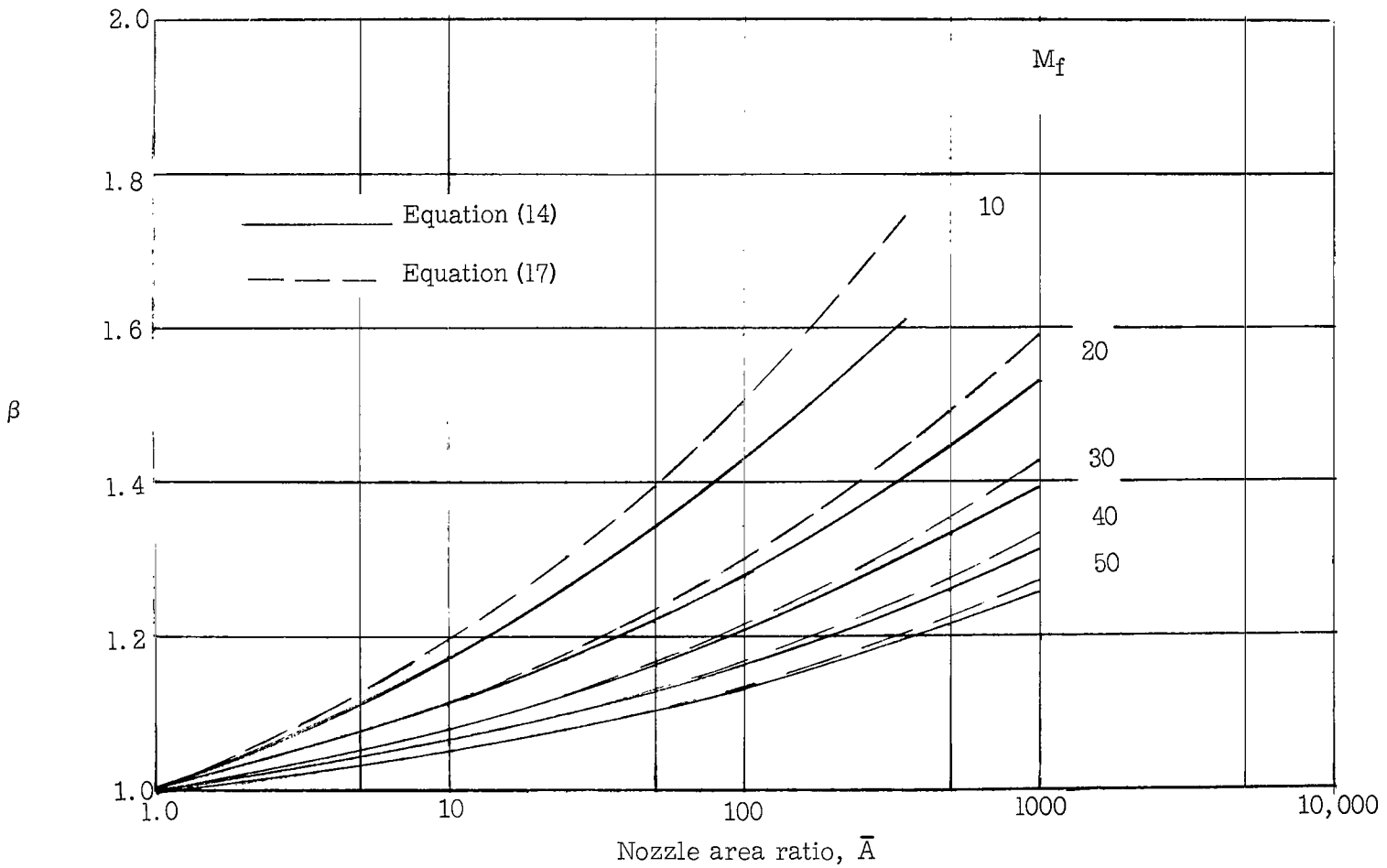

(b) Area ratio.

Figure 4.- Concluded.

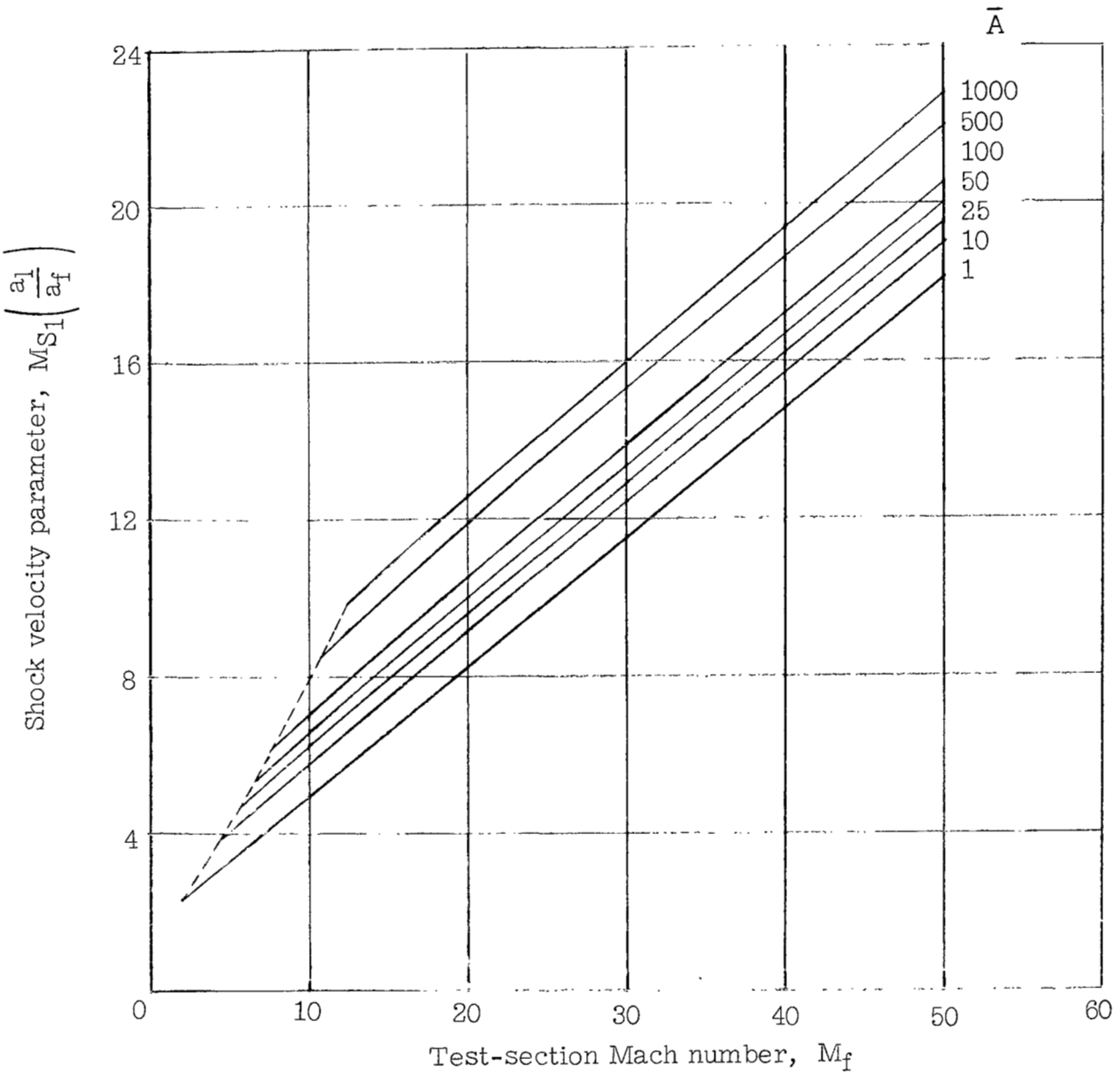

Figure 5.- Variation of primary shock velocity parameter with test-section Mach number.

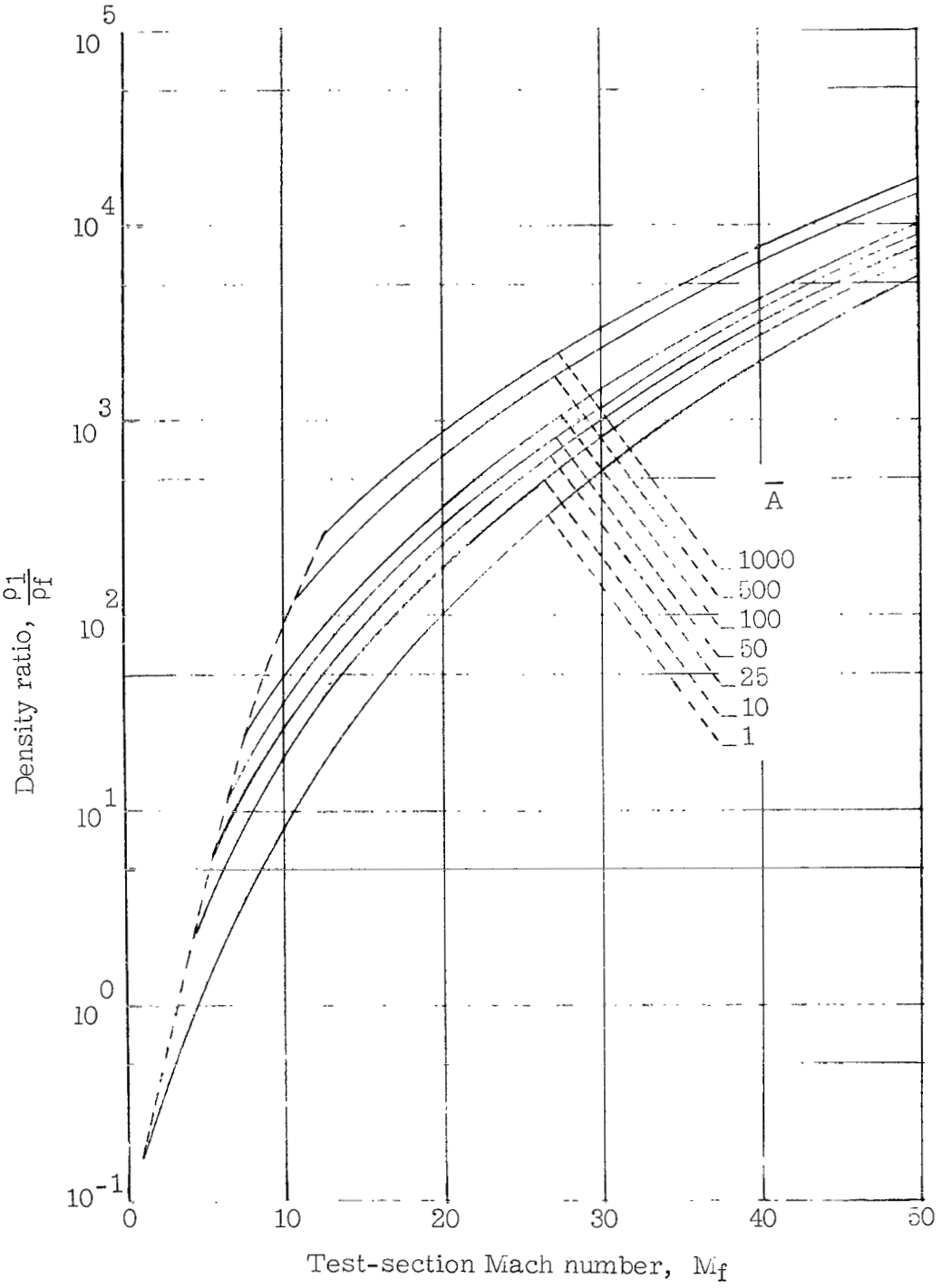

Figure 6.- Variation of initial intermediate-chamber density ratio with test-section Mach number.

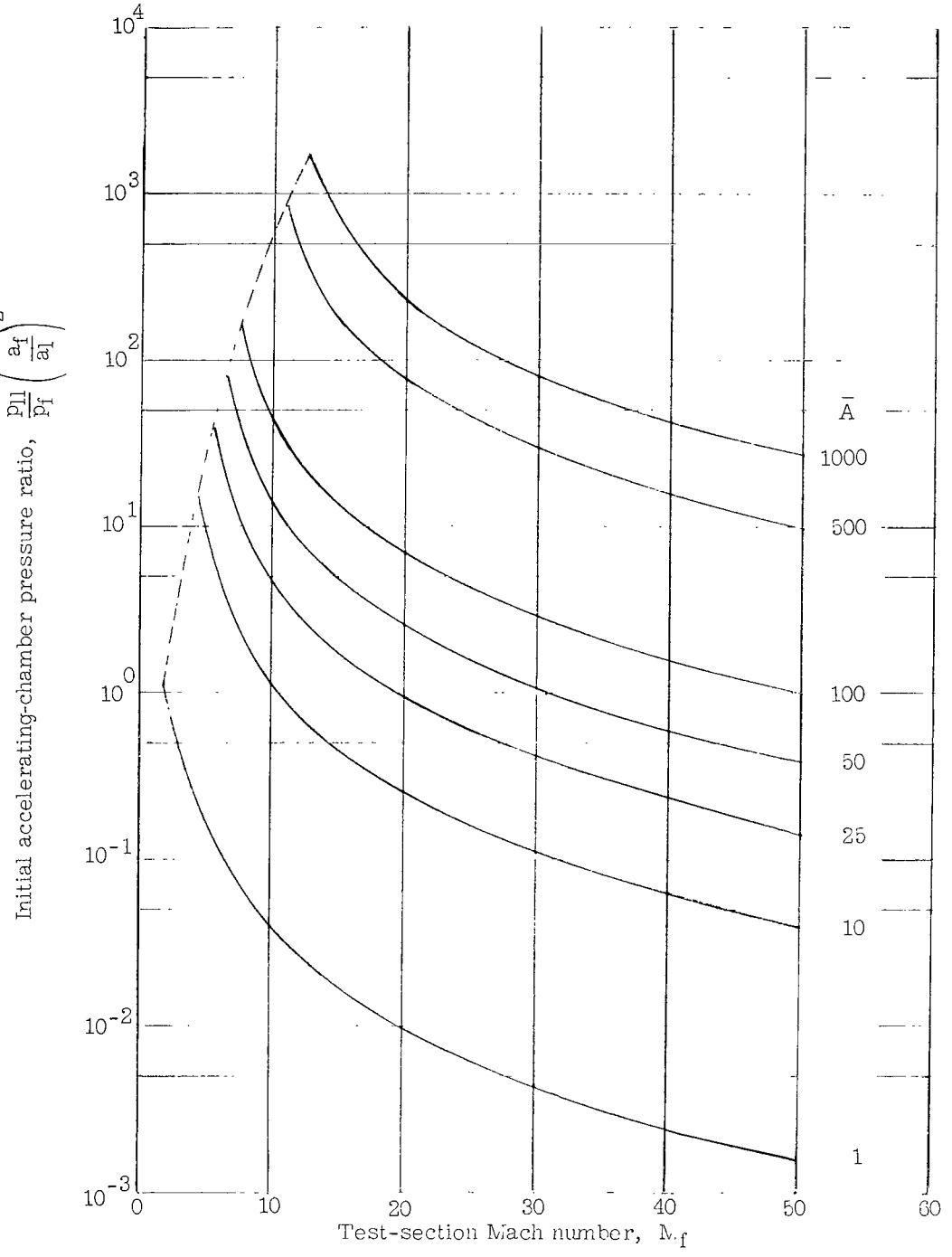

Figure 7. - Initial accelerating-chamber pressure ratio parameter for $\frac{a_1}{a_{11}} = \frac{49}{144}$, $\gamma_{11} = \frac{5}{3}$.

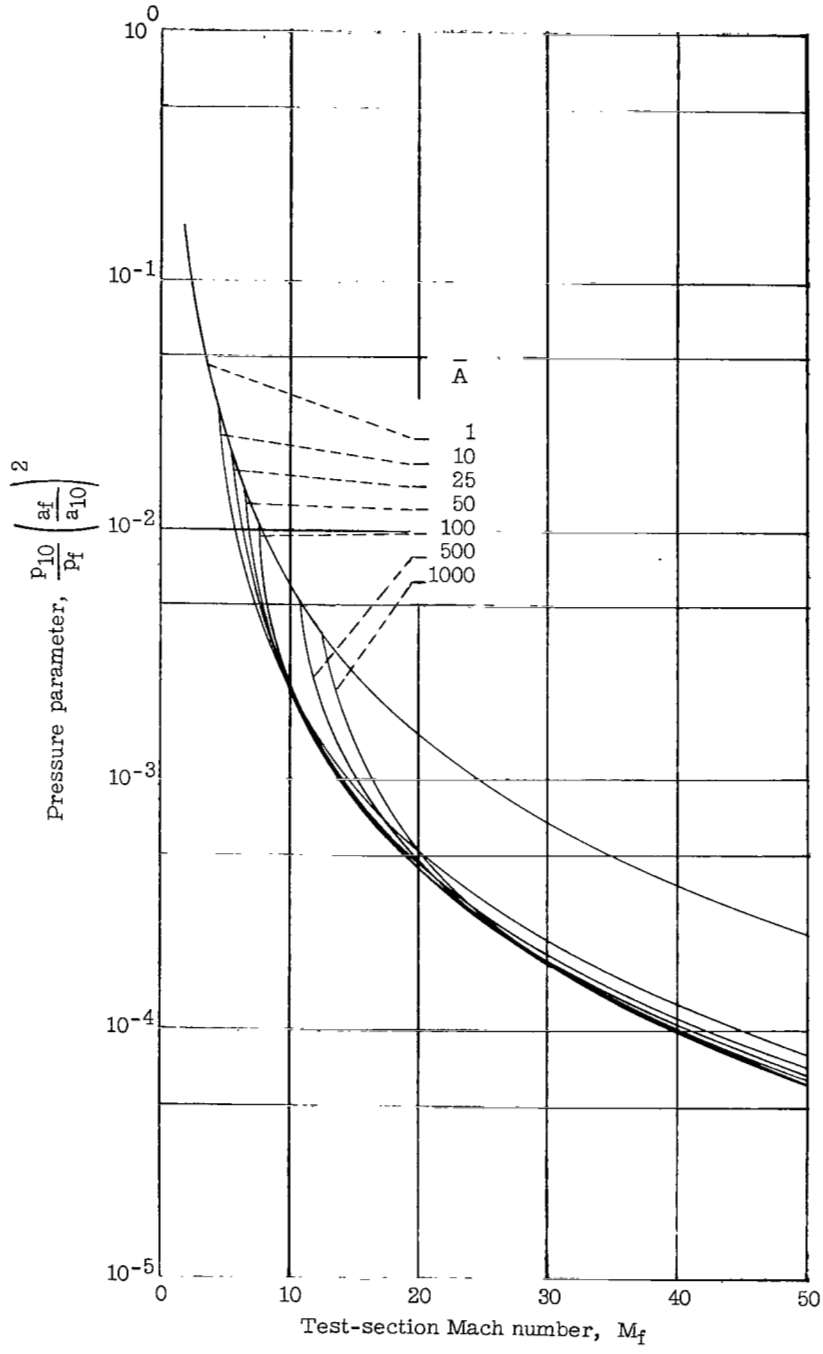

(a) $\gamma_{10} = \gamma_{11} = 1.4$.

Figure 8. - Dump-tank charging pressure parameter for perfect nozzle start.

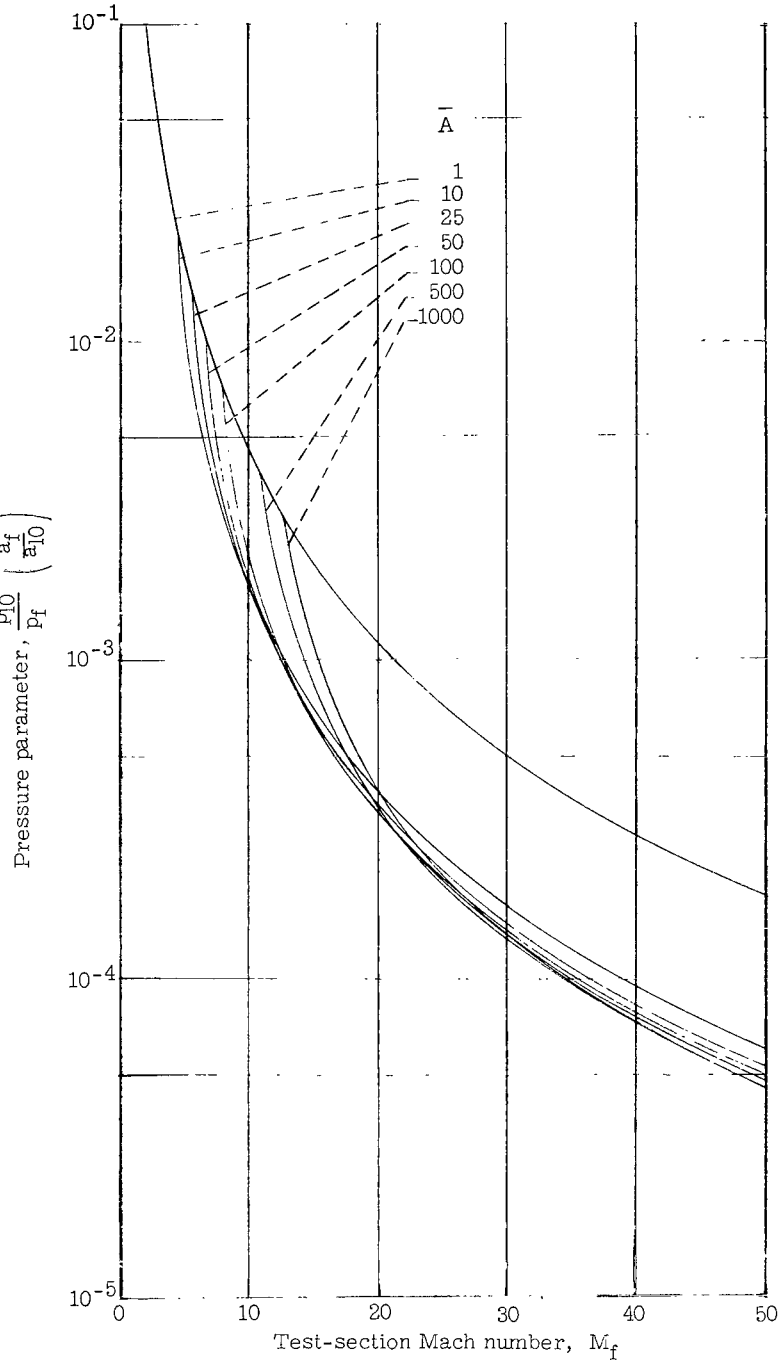

(b) $\gamma_{10} = \frac{5}{3}$; $\gamma_{11} = 1.4$.

Figure 8.- Continued.

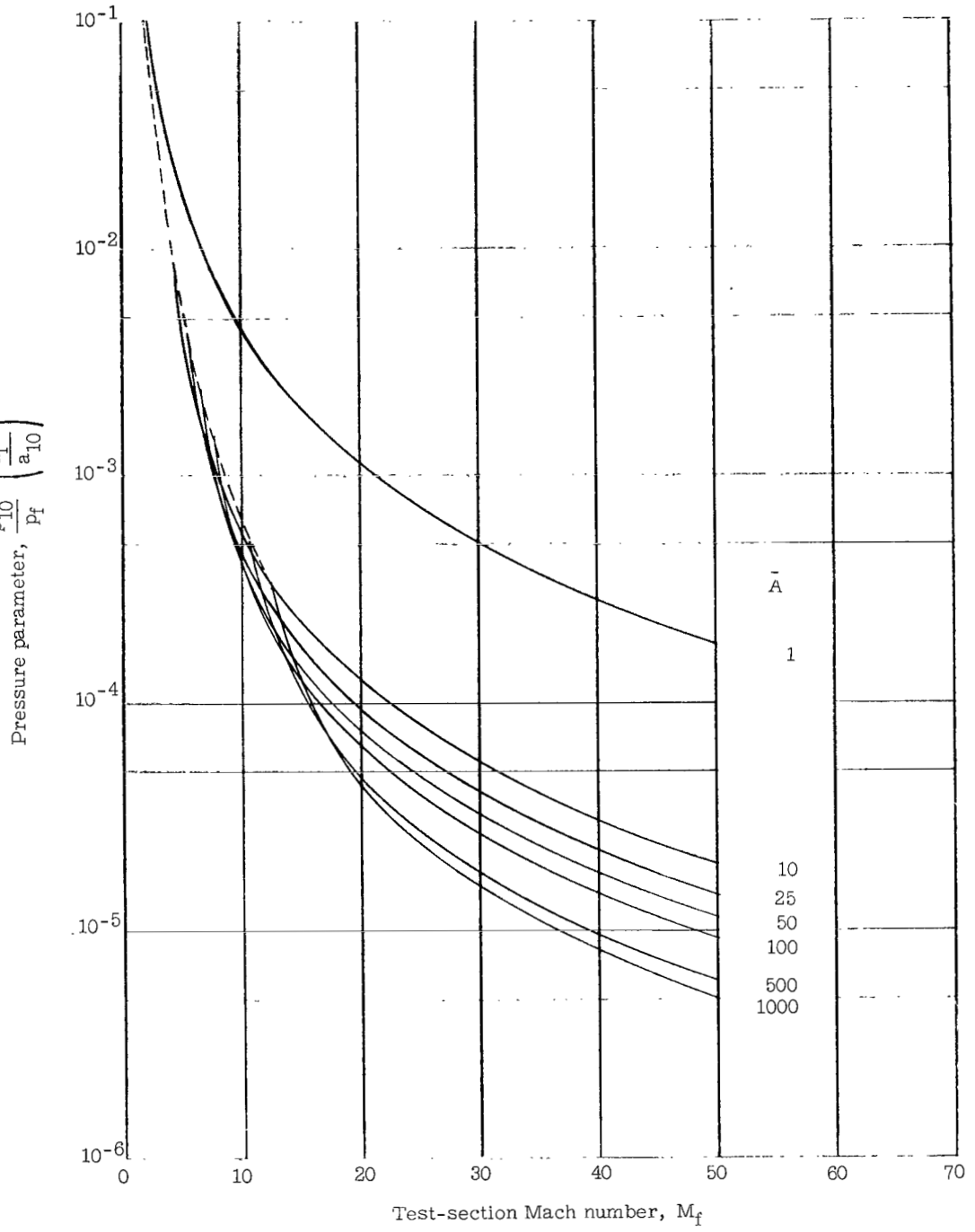

(c) $\gamma_{10} = \gamma_{11} = \frac{5}{3}$.

Figure 8.- Concluded.

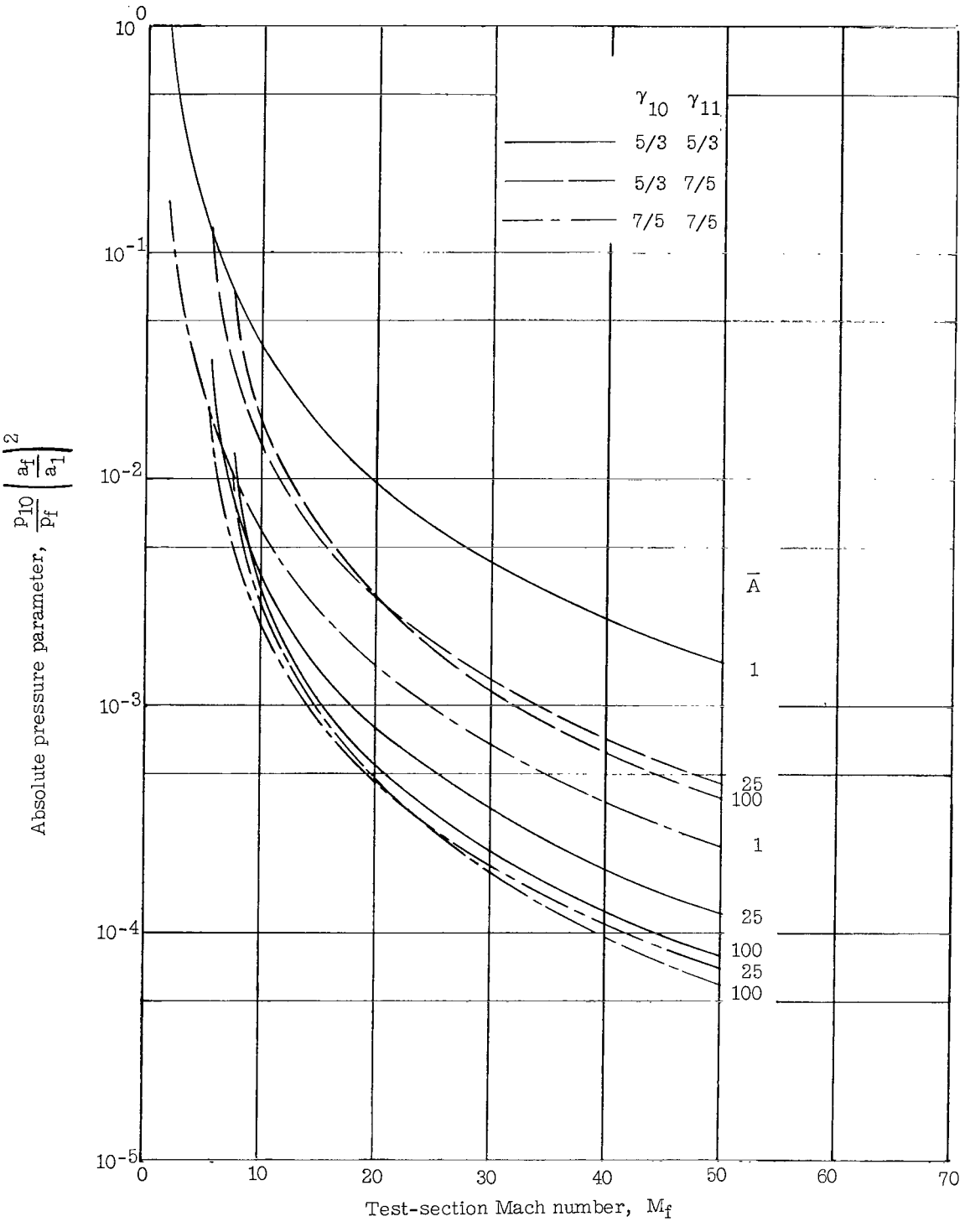

Figure 9. - Dump-tank absolute charging pressure for perfect nozzle start.

(a) Schematic of wave system.

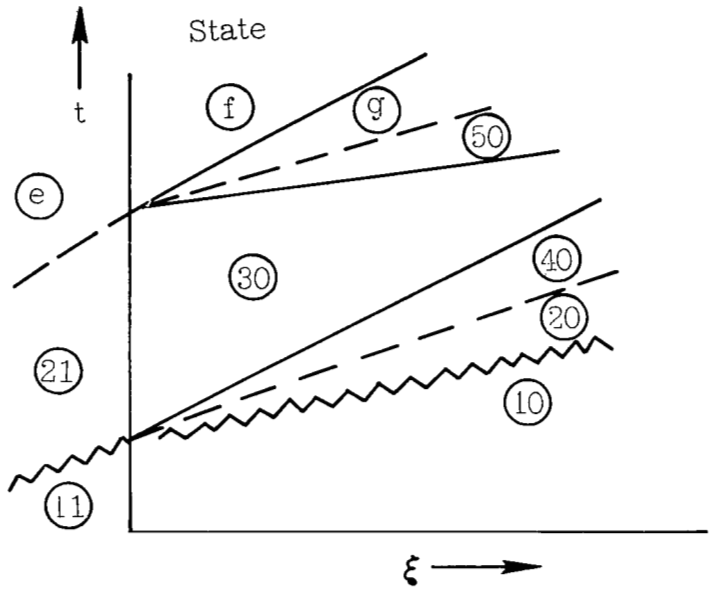

(b) Wave diagram.

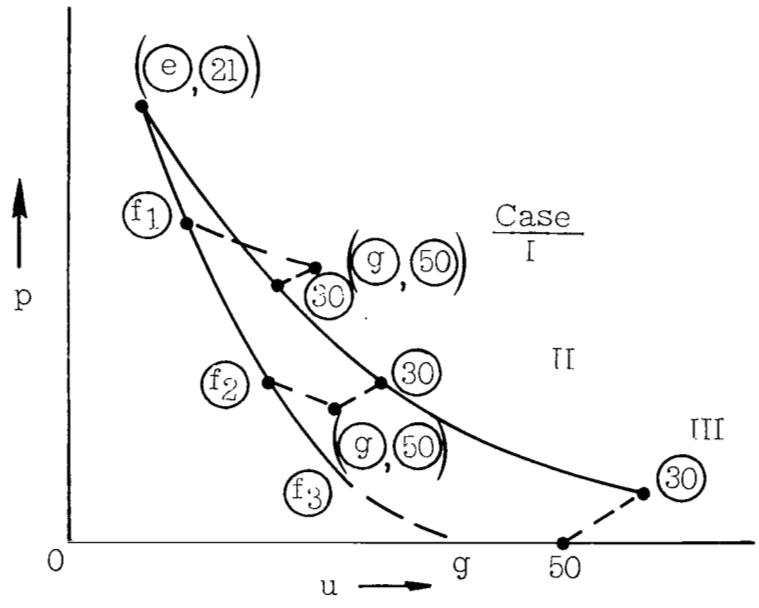

(c) Pressure-velocity diagram.

Figure 10.- Unsteady waves generated by entropy discontinuity flowing through nozzle.

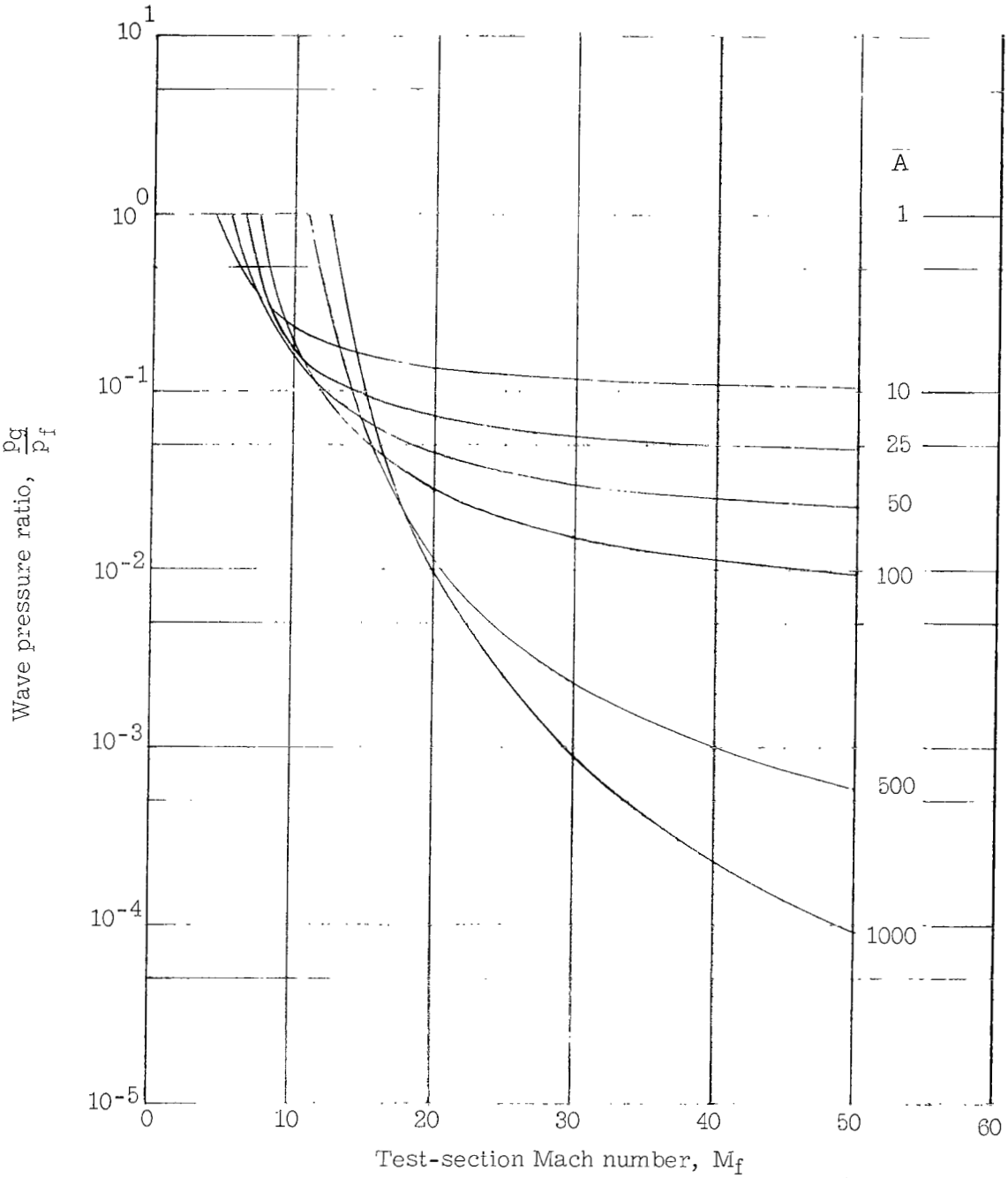

(a) $\gamma_{11} = 1.4$.

Figure 11. - Pressure ratio across waves generated by passage of entropy discontinuity between ⓔ and ㉑ through nozzle.

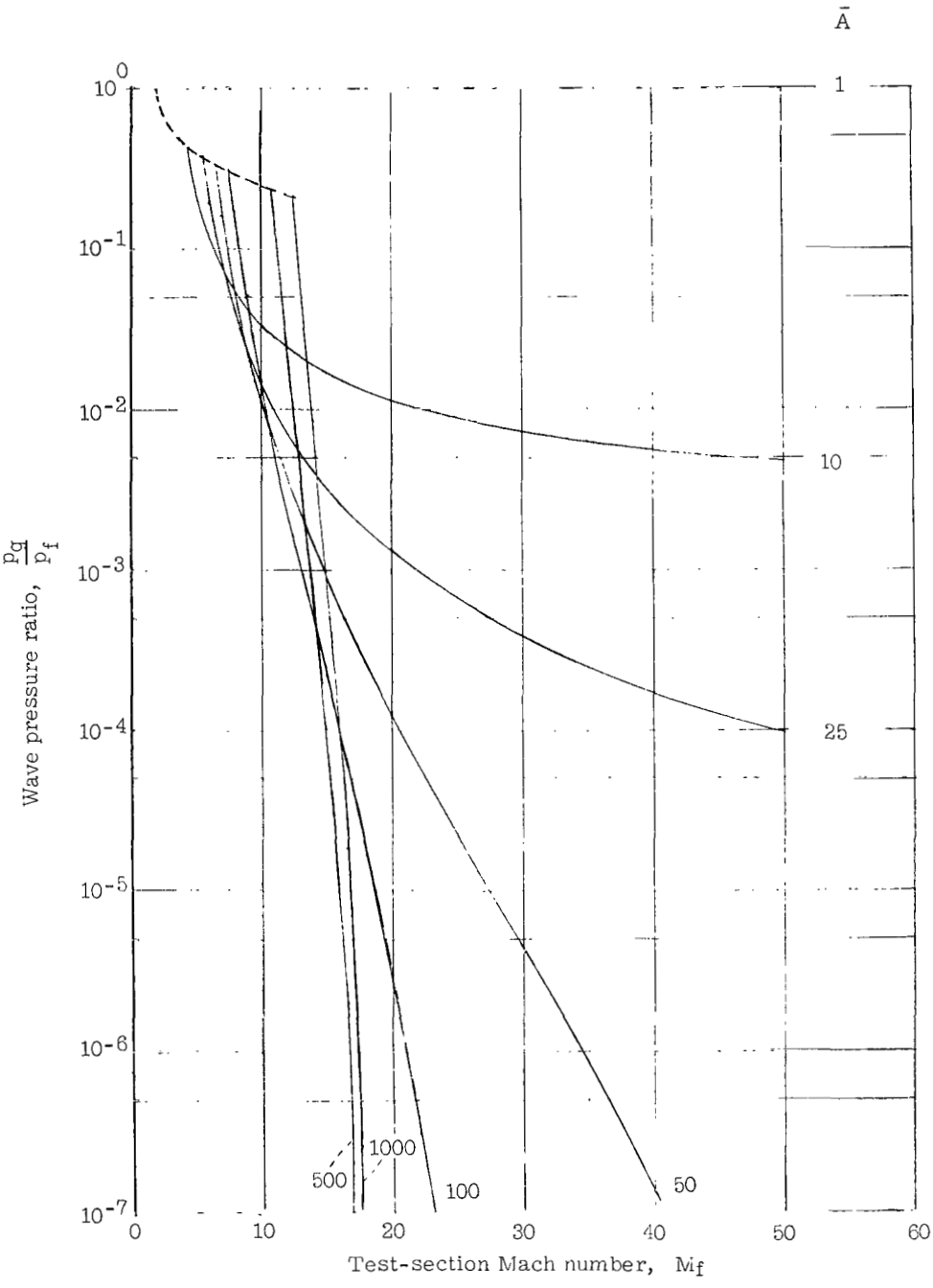

(b) $\gamma_{11} = \frac{5}{3}$.

Figure 11.- Concluded.

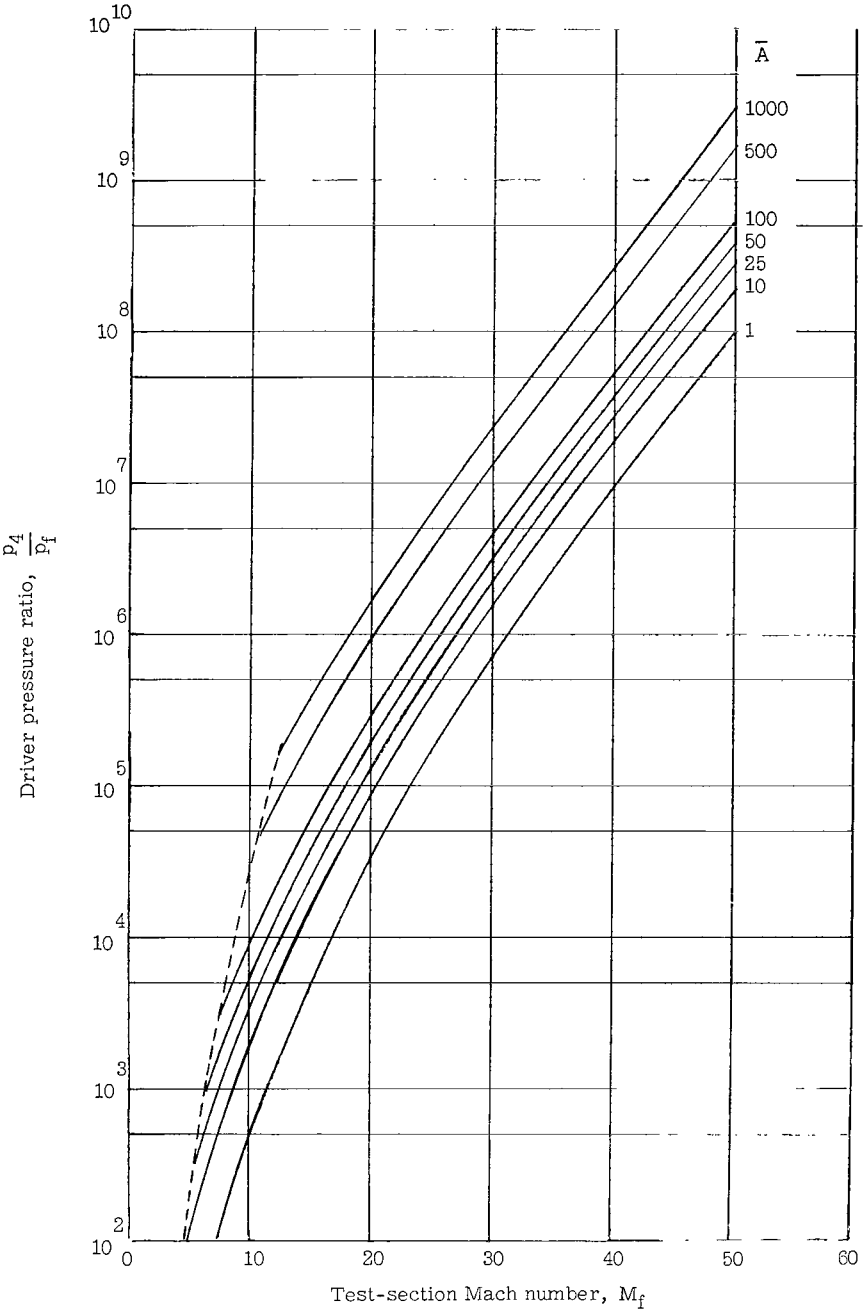

(a) $\frac{T_4}{T_f} = 10.$

Figure 12. - Driver pressure ratio for helium driver gas at various temperatures.

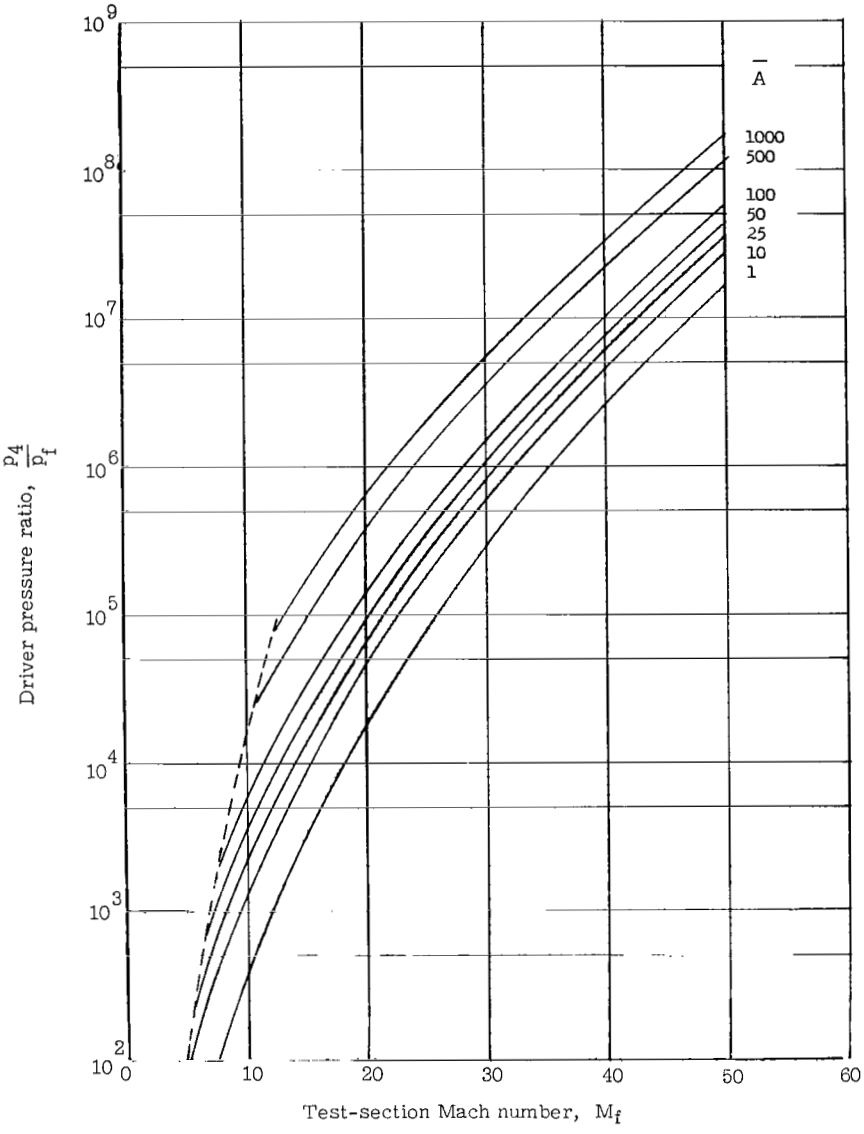

(b) $\frac{T_4}{T_f} = 25.$

Figure 12.- Continued.

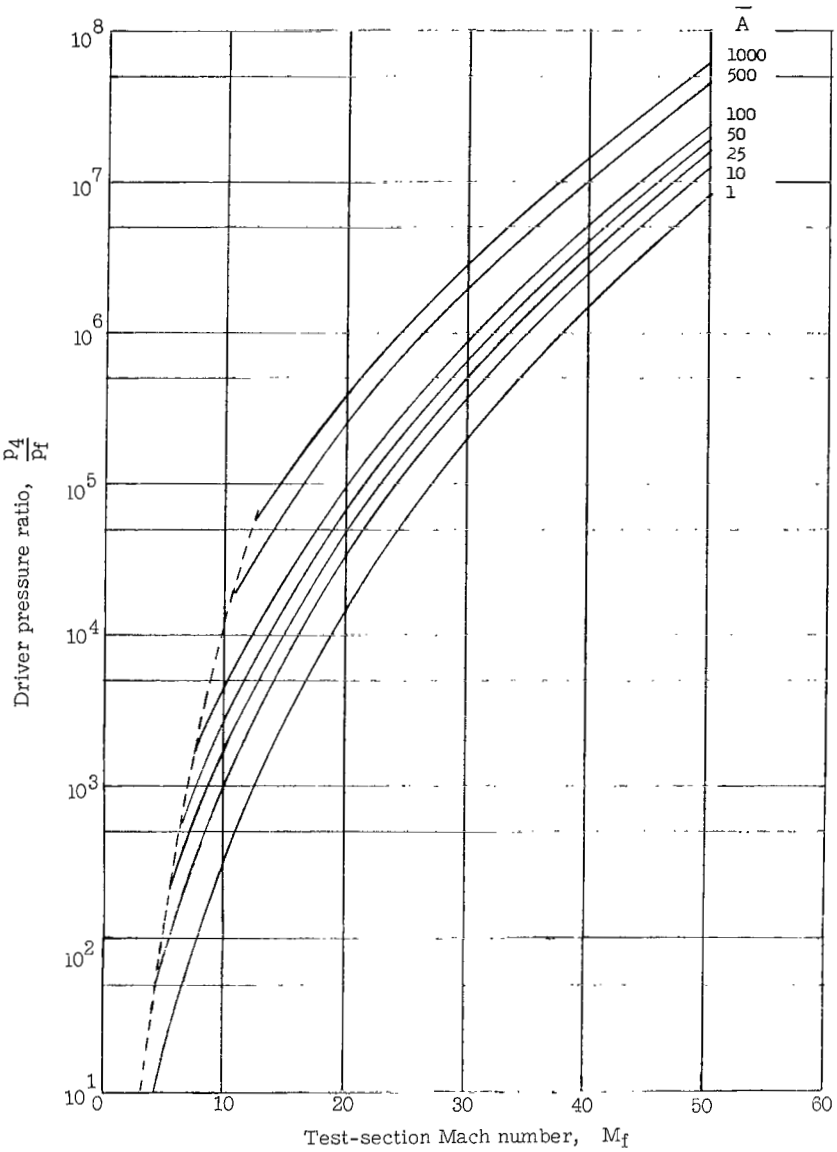

(c) $\frac{T_4}{T_f} = 50.$

Figure 12.- Concluded.

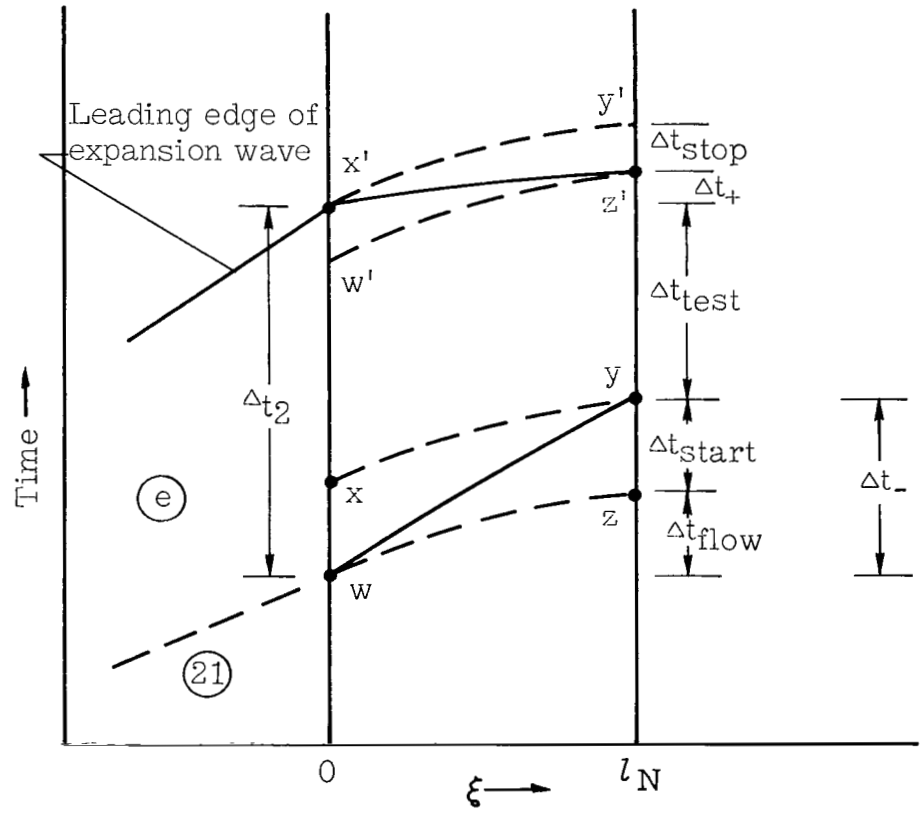

Figure 13.- Wave diagram illustrating nozzle starting processes and resulting test time.

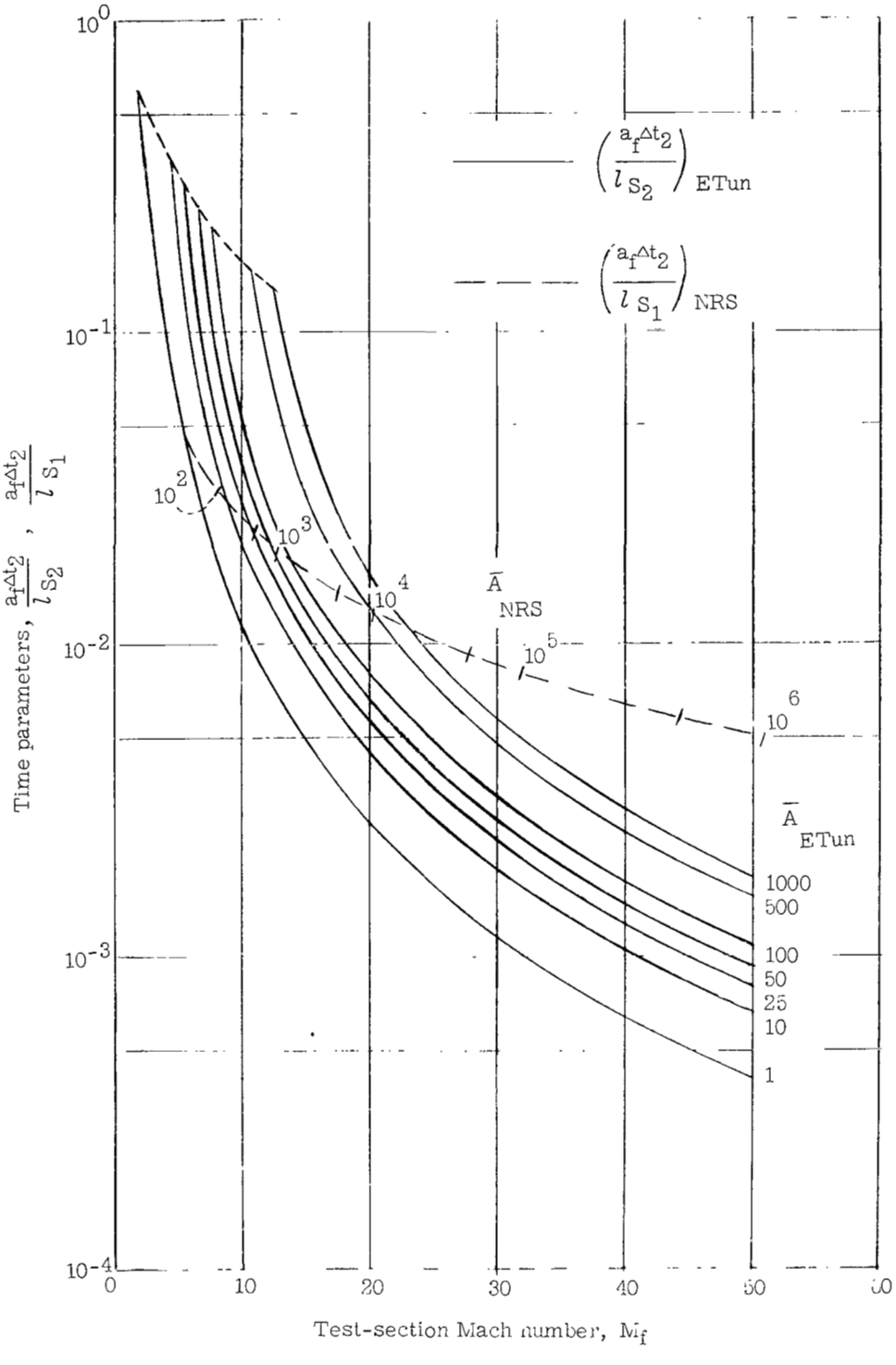

Figure 14. - Zero-nozzle-length test time parameters for expansion tunnel and nonreflected shock tunnel.

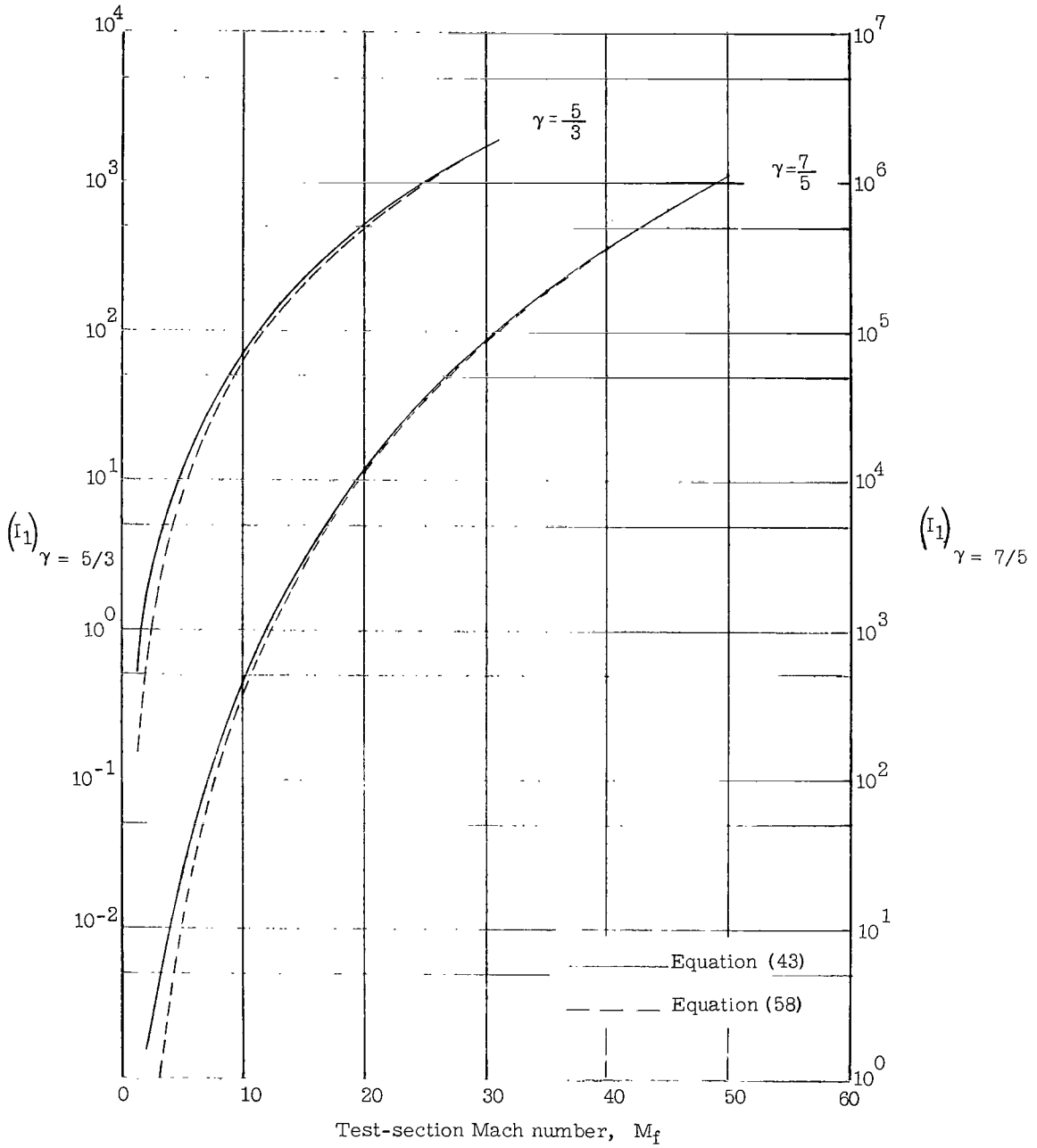

(a) I_1.

Figure 15.- Integrals I_n and J_n for $\gamma = \frac{5}{3}$ and $\frac{7}{5}$ with lower limit $M_e = 1$.

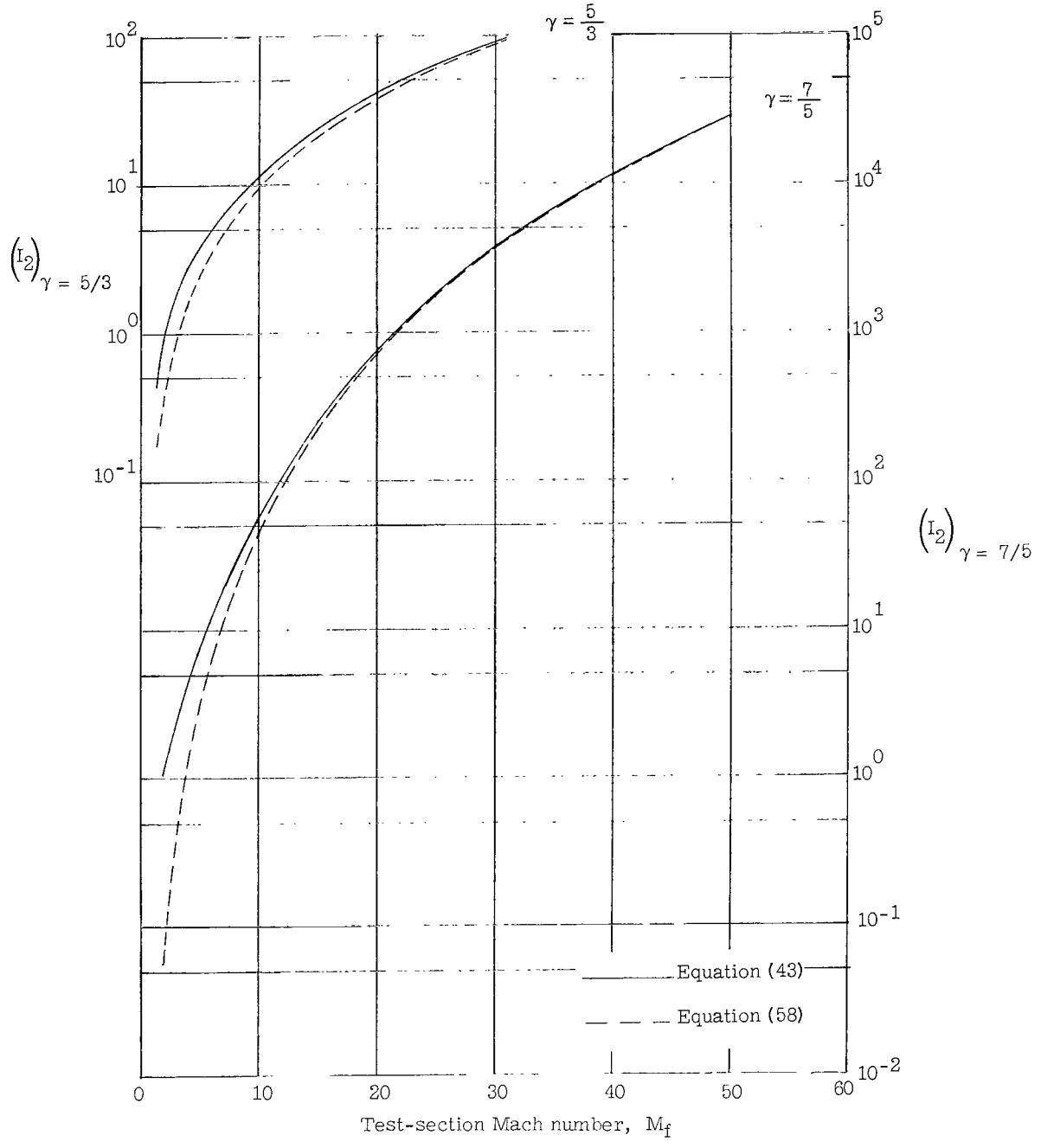

(b) I_2.

Figure 15.- Continued.

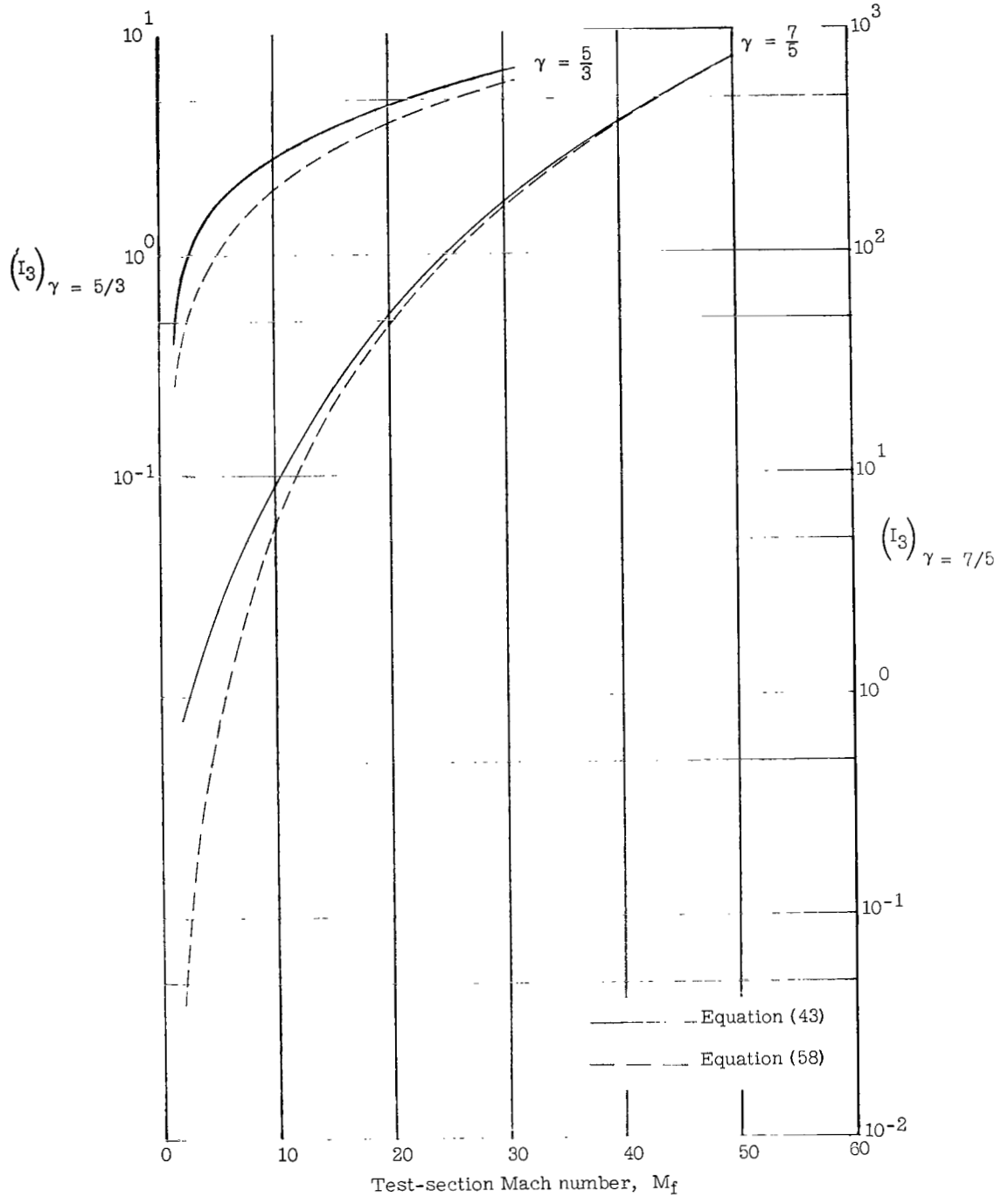

(c) I_3.

Figure 15.- Continued.

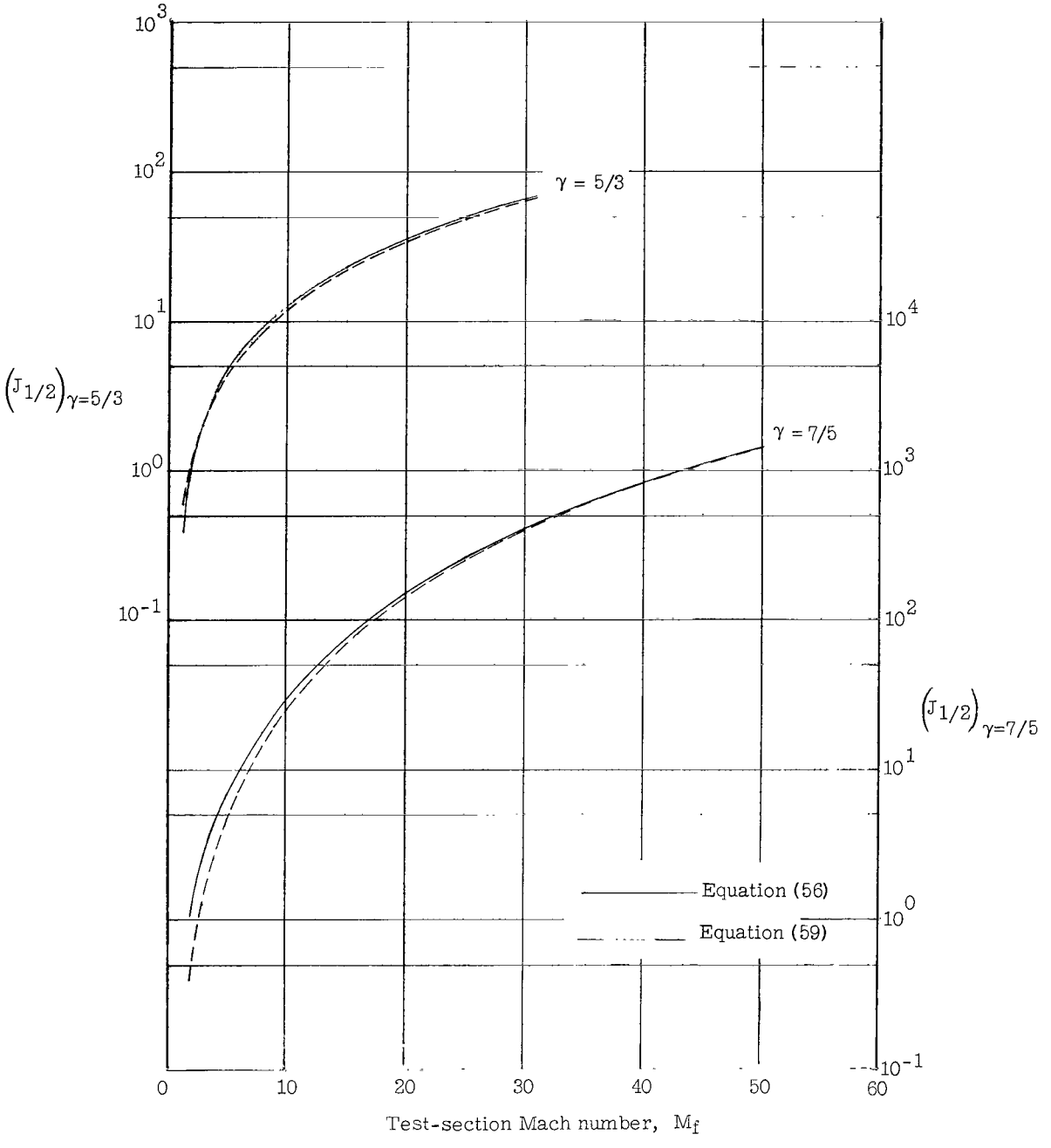

(d) $J_{1/2}$.

Figure 15.- Continued.

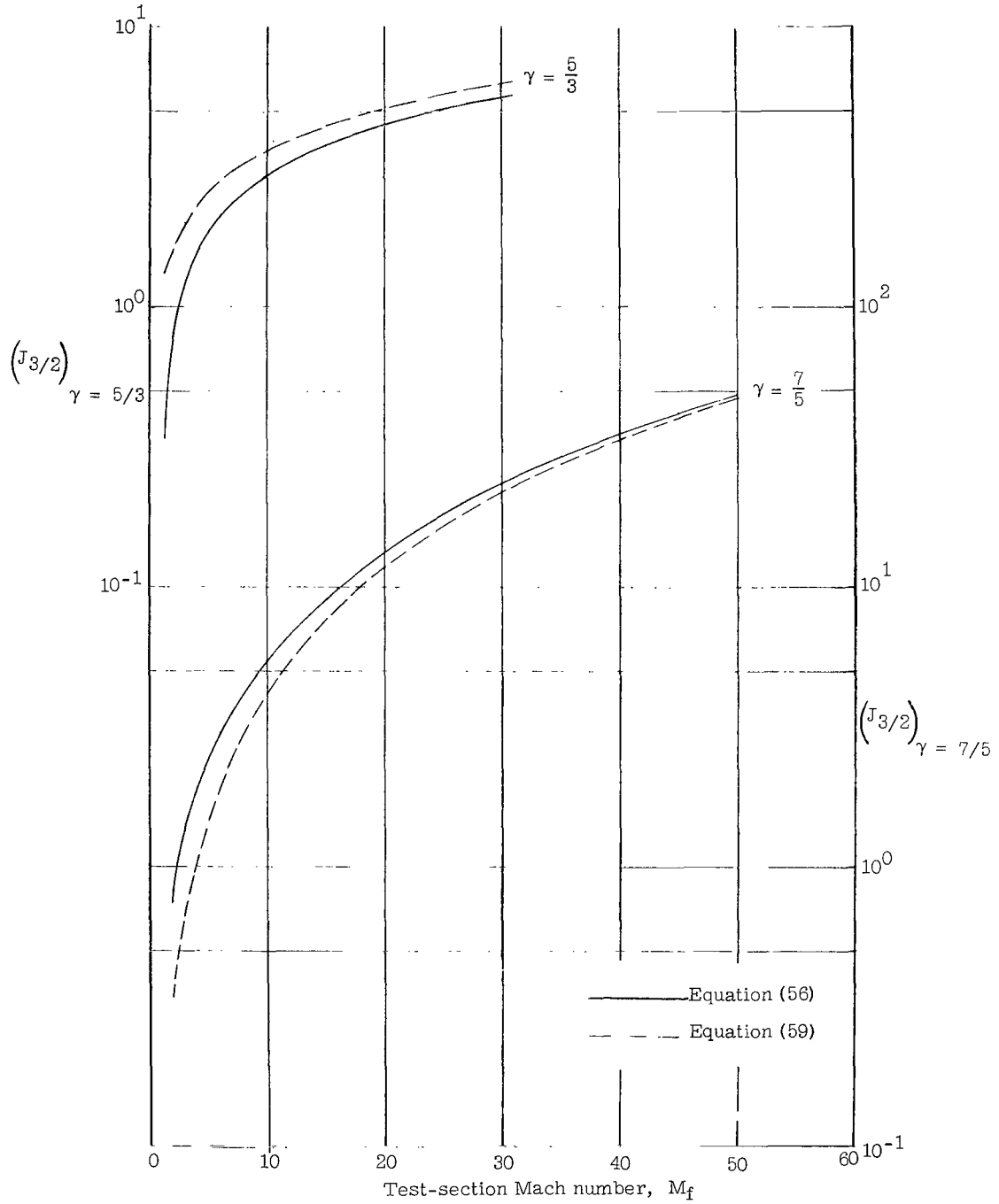

(e) $J_{3/2}$.

Figure 15.- Continued.

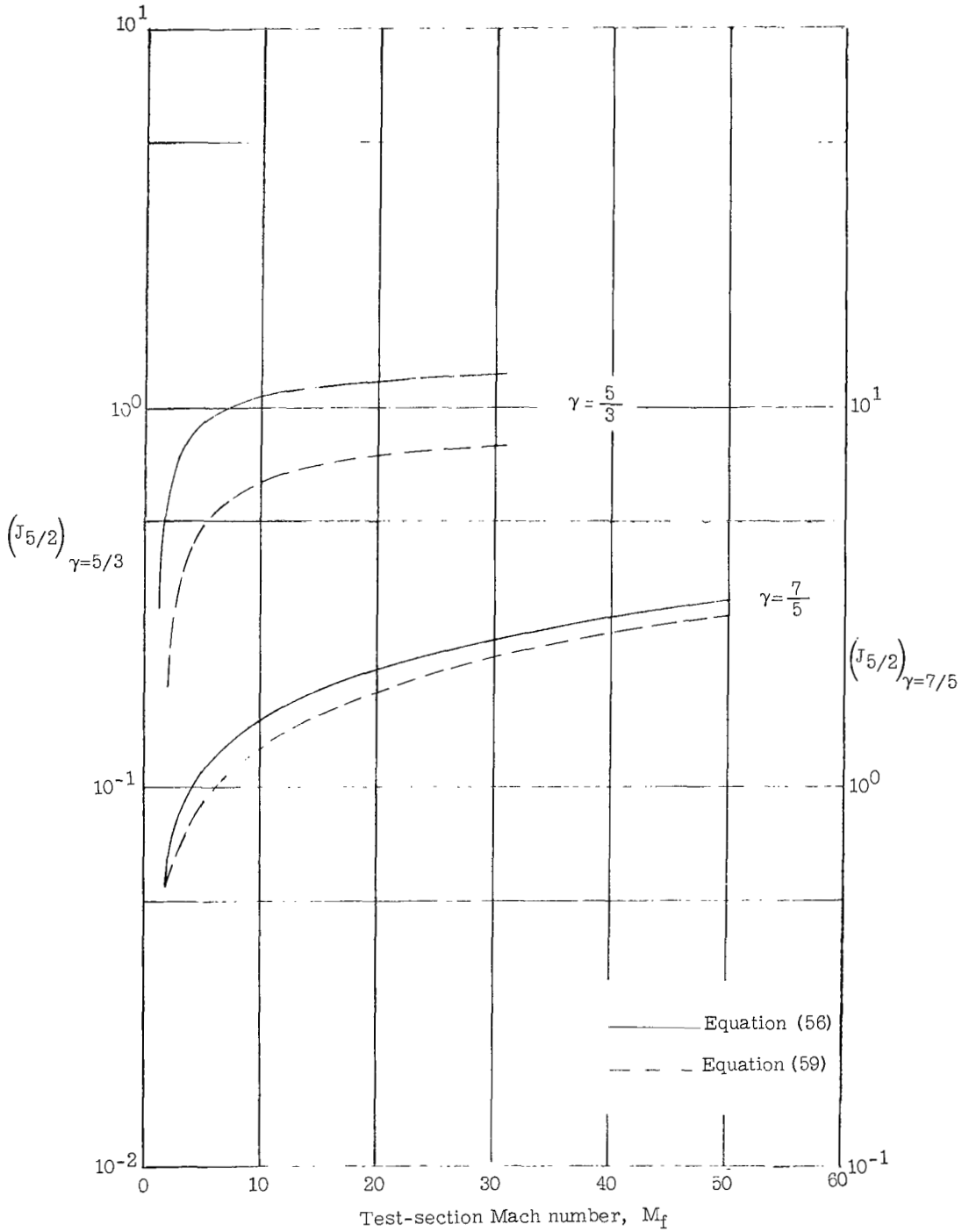

(f) $J_{5/2}$.

Figure 15.- Concluded.

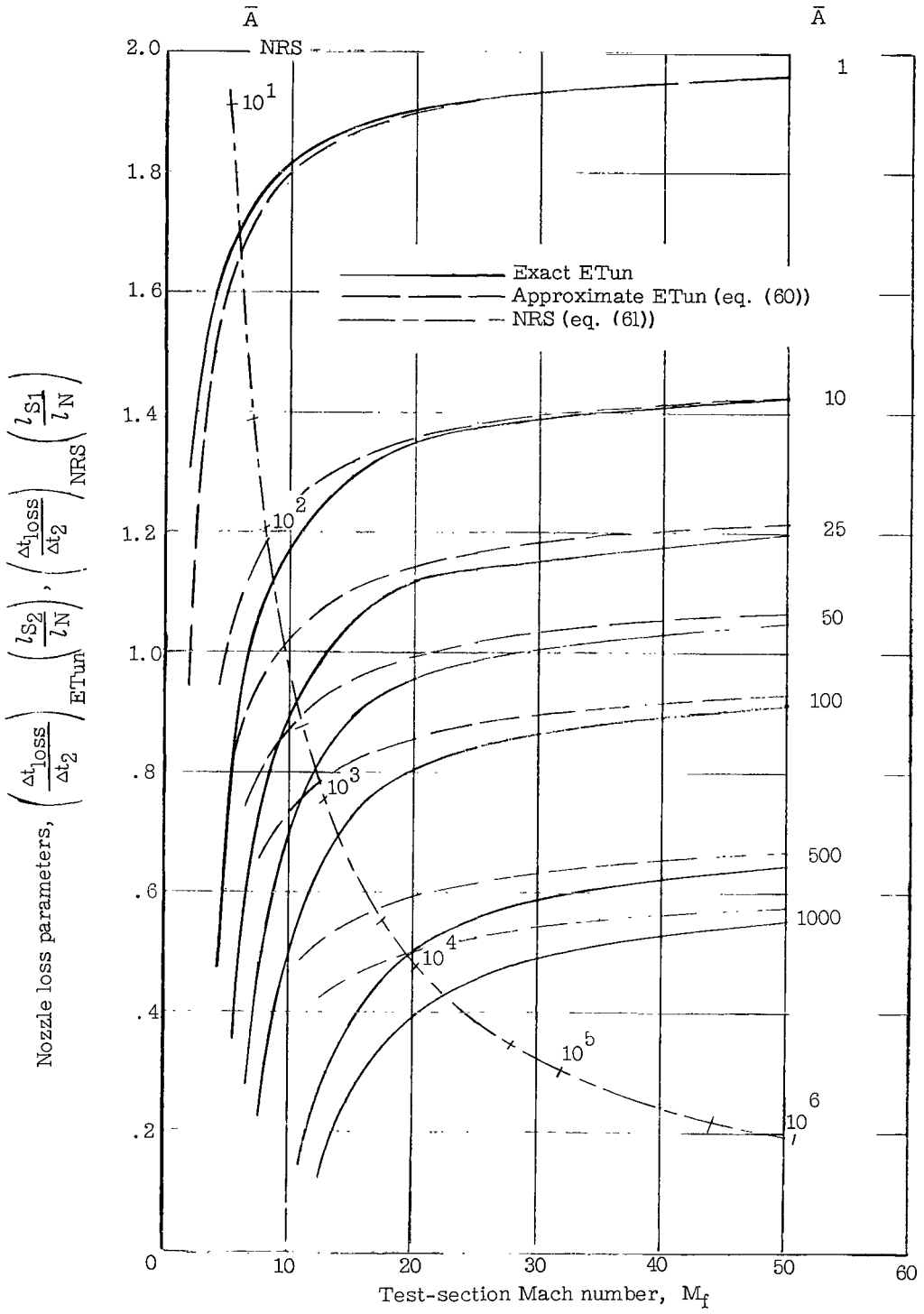

Figure 16.- Effect of nozzle length on loss of test time for linear area nozzle.

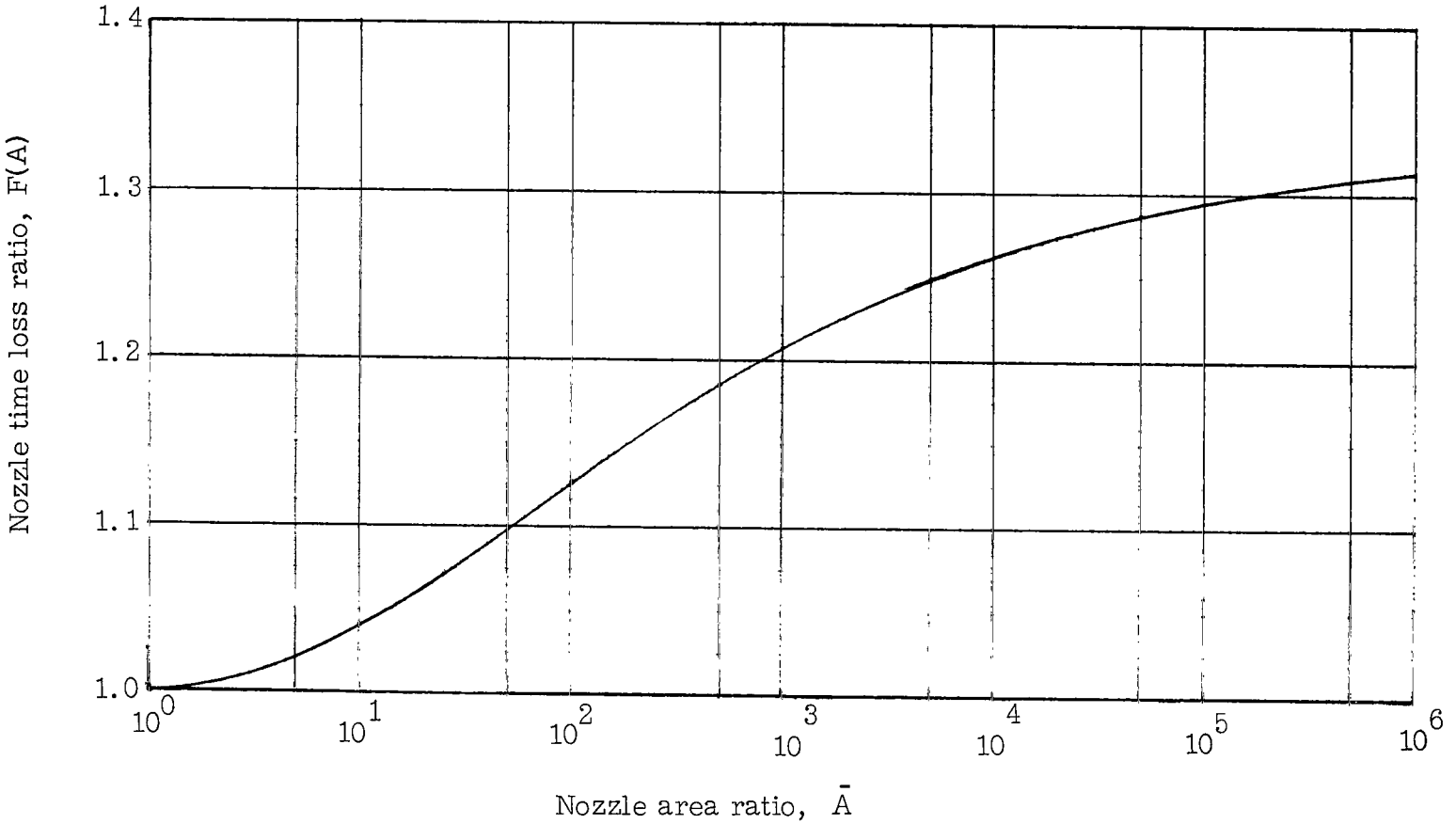

Figure 17.- Ratio of nozzle time losses in linear-radius nozzle compared with those in linear-area nozzle.

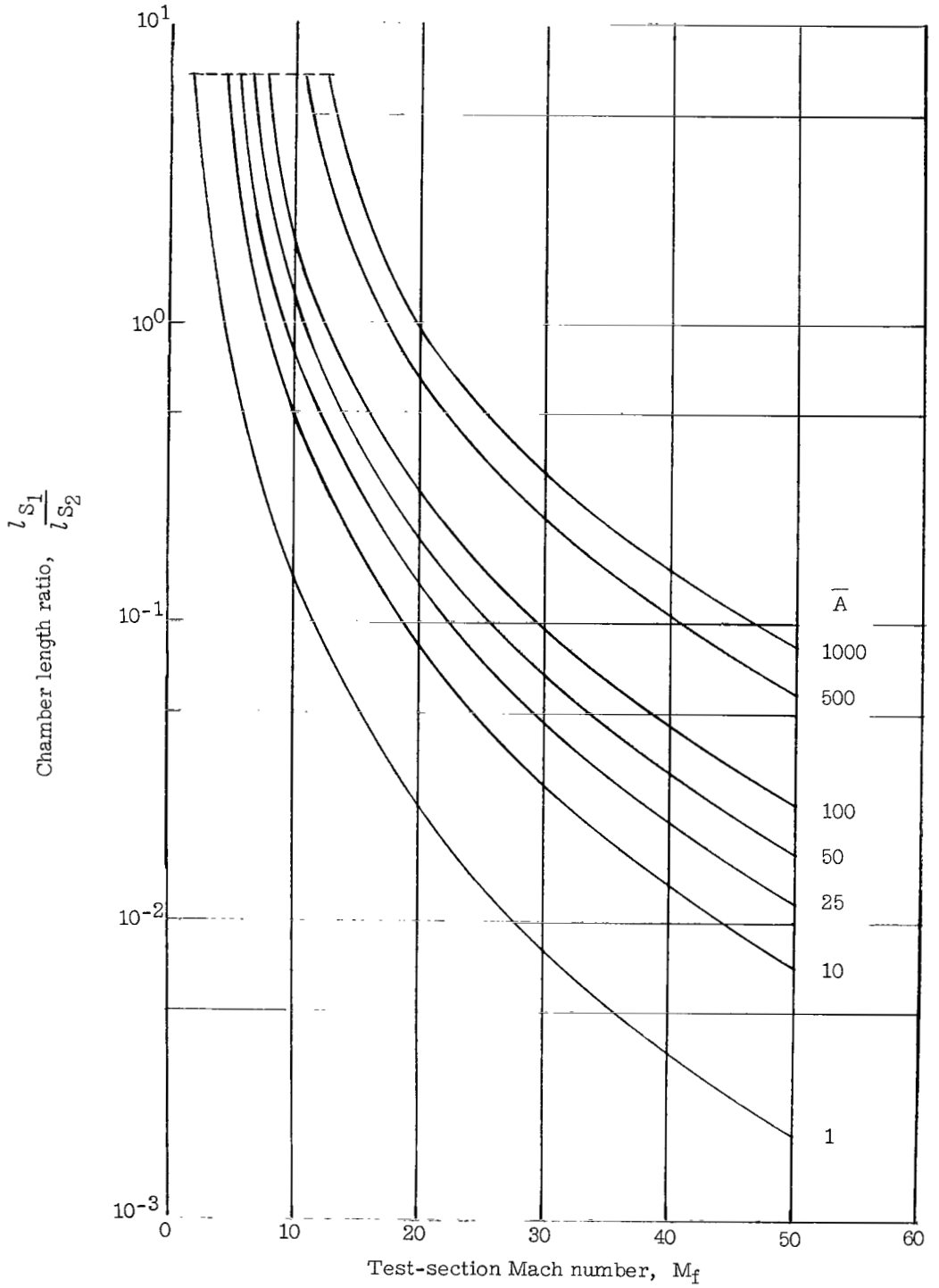

Figure 18. - Ratio of intermediate-chamber length to accelerating-chamber length.

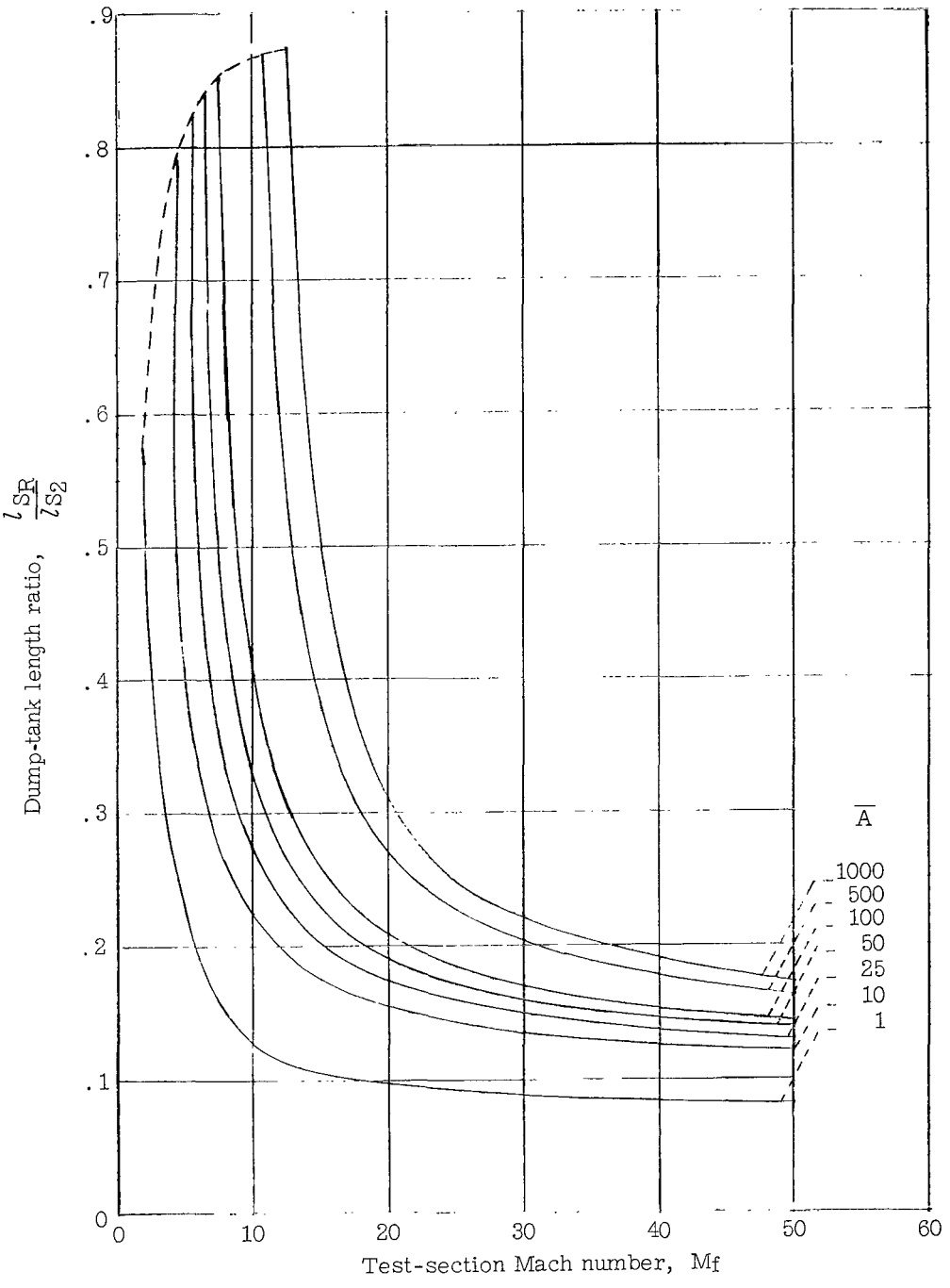

(a) $\gamma_{10} = \frac{5}{3}$; $\gamma_{11} = \frac{7}{5}$.

Figure 19. - Ratio of dump-tank length to accelerating-chamber length.

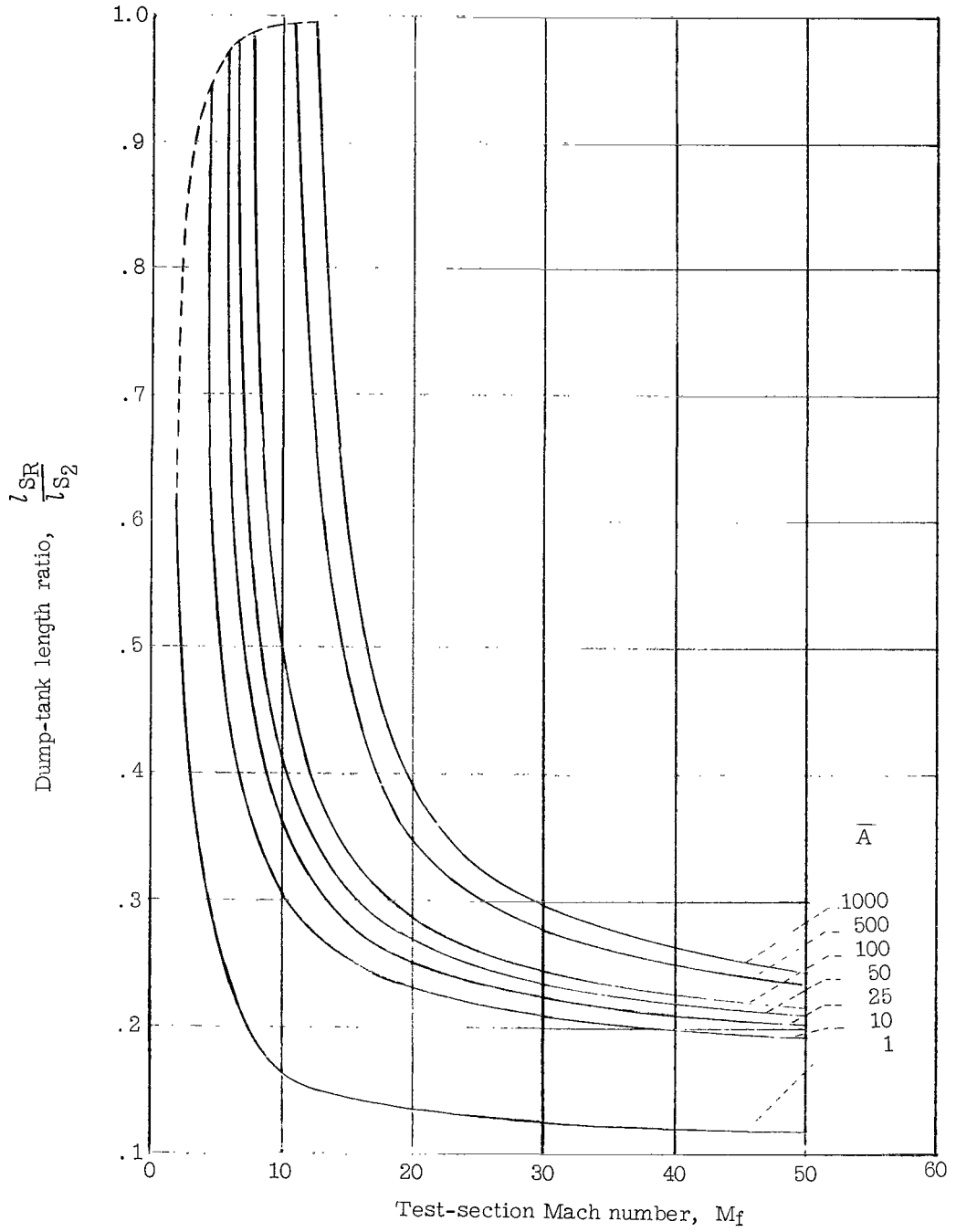

(b) $\gamma_{10} = \gamma_{11} = \frac{5}{3}$.

Figure 19.- Concluded.

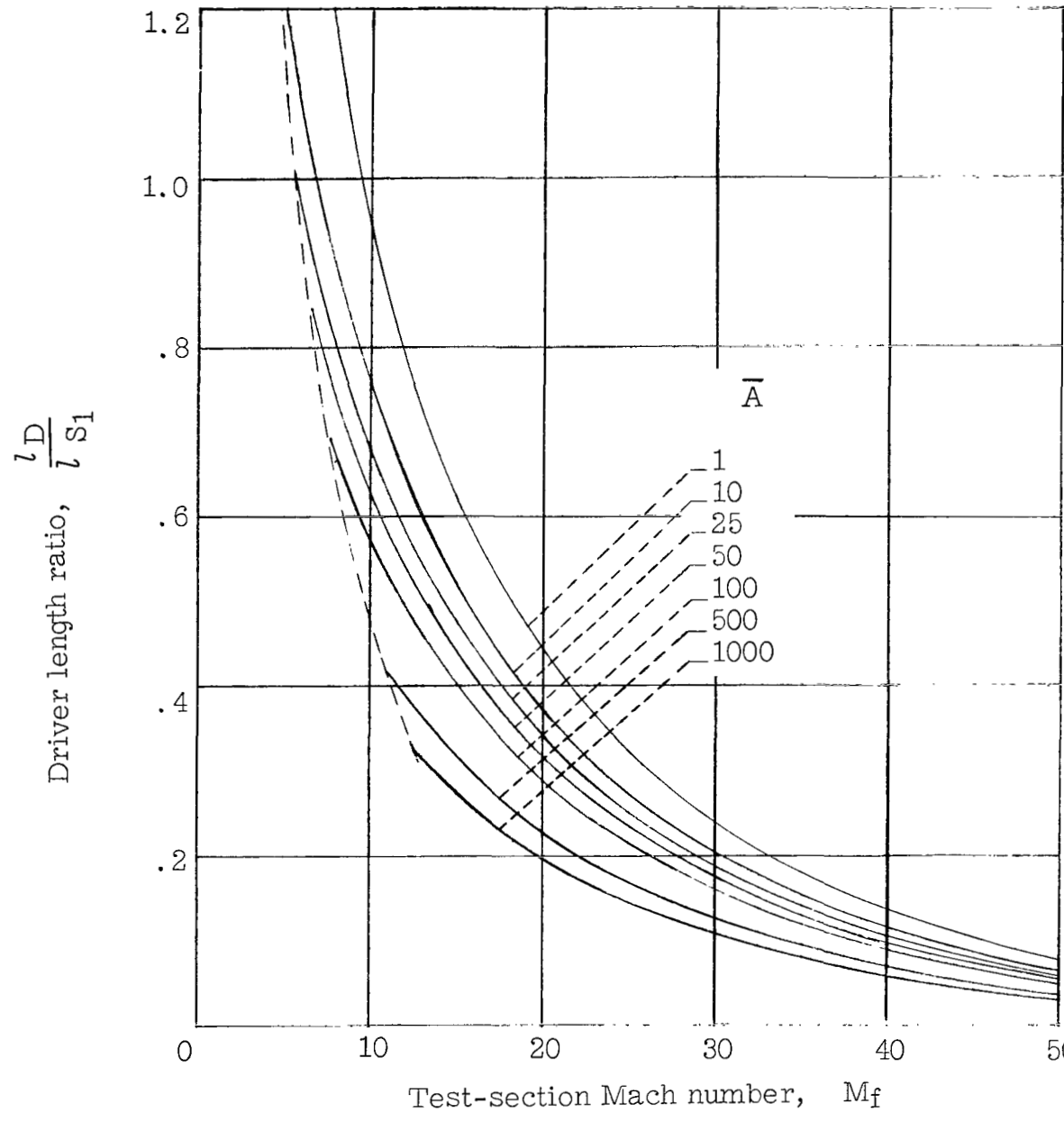

(a) $\frac{T_4}{T_f} = 10.$

Figure 20. - Ratio of driver length to intermediate-chamber length for helium driver. $\gamma_4 = \frac{5}{3}$.

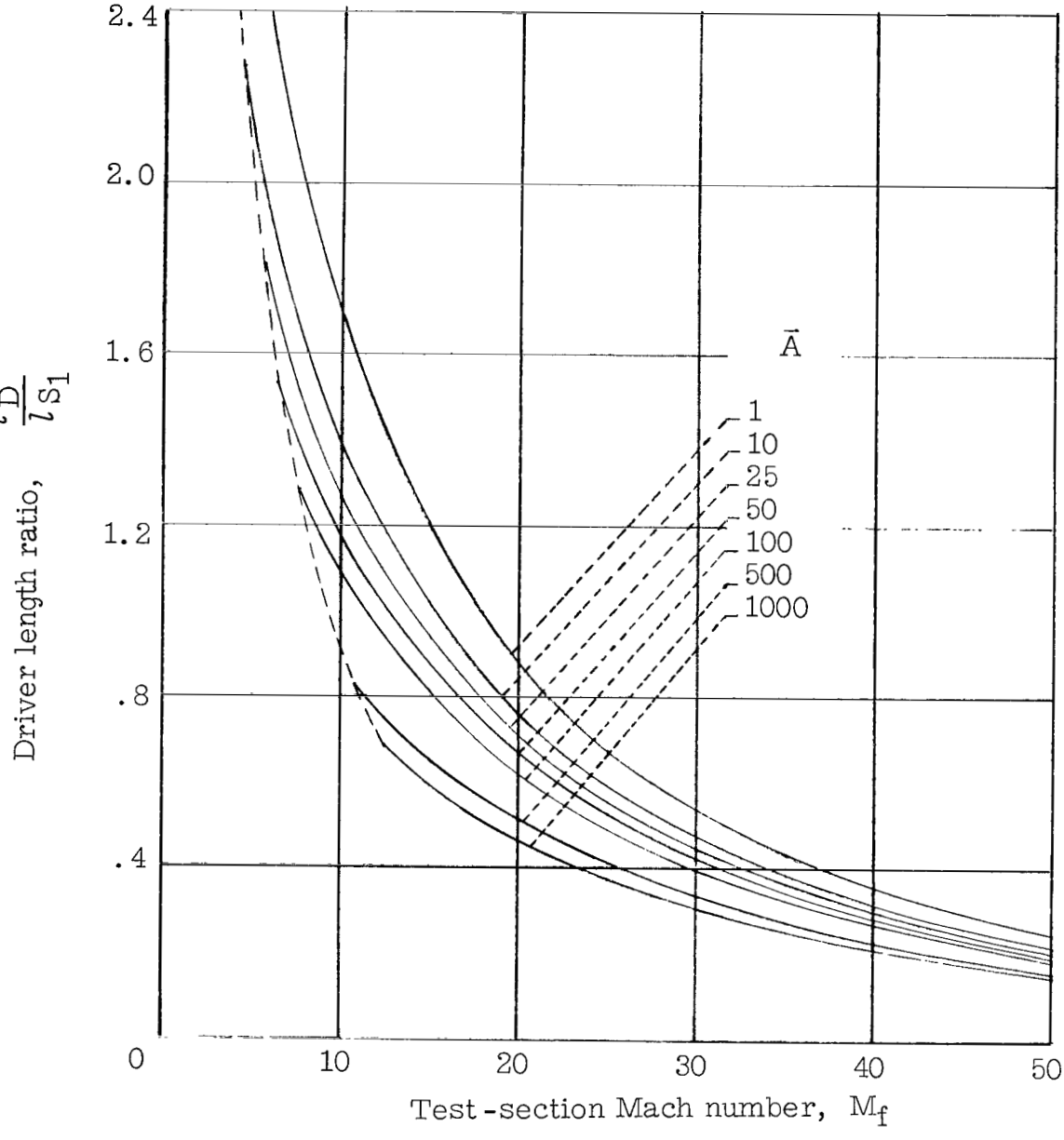

(b) $\frac{T_4}{T_f} = 25.$

Figure 20.- Continued.

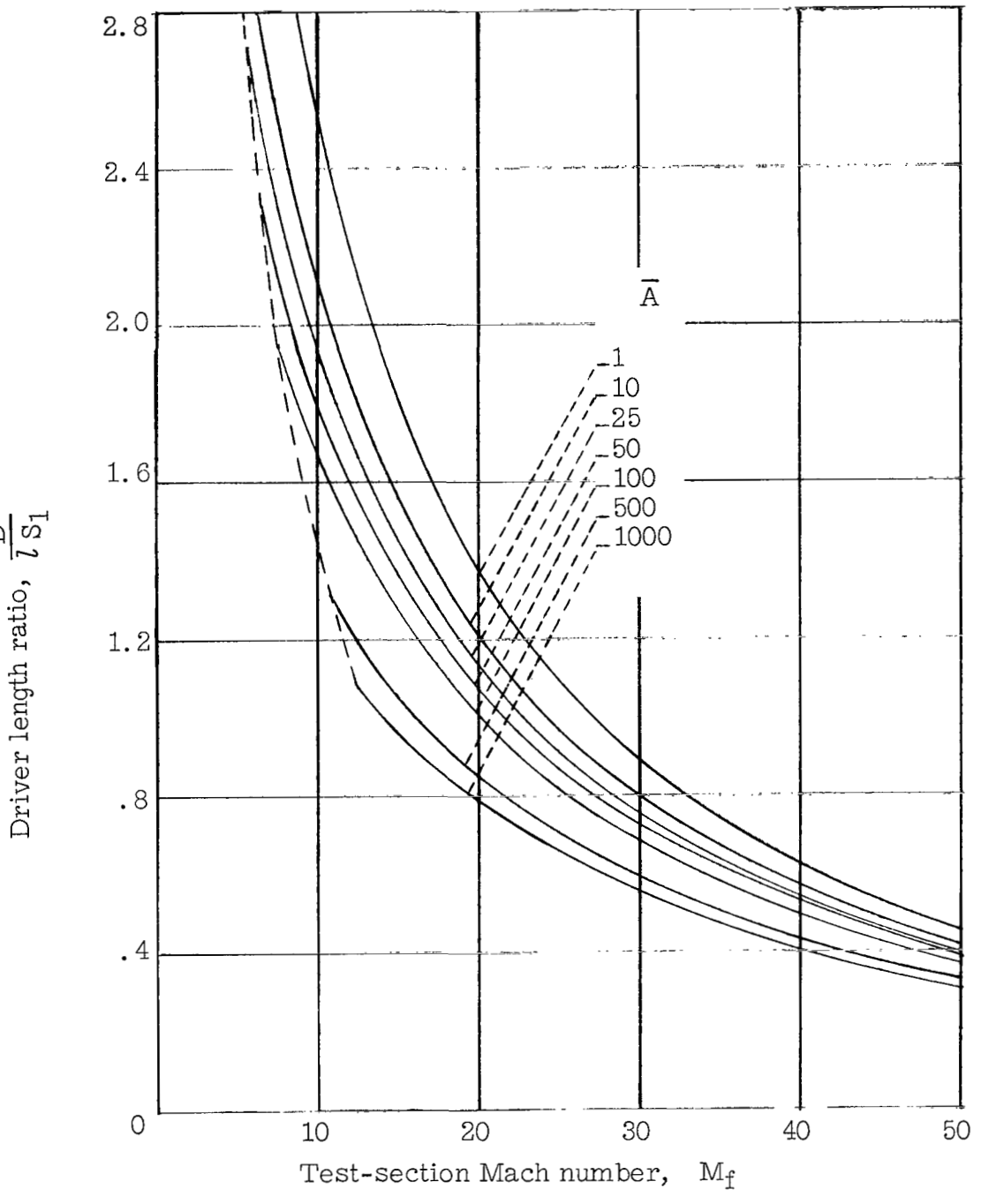

(c) $\frac{T_4}{T_f} = 50.$

Figure 20.- Concluded.

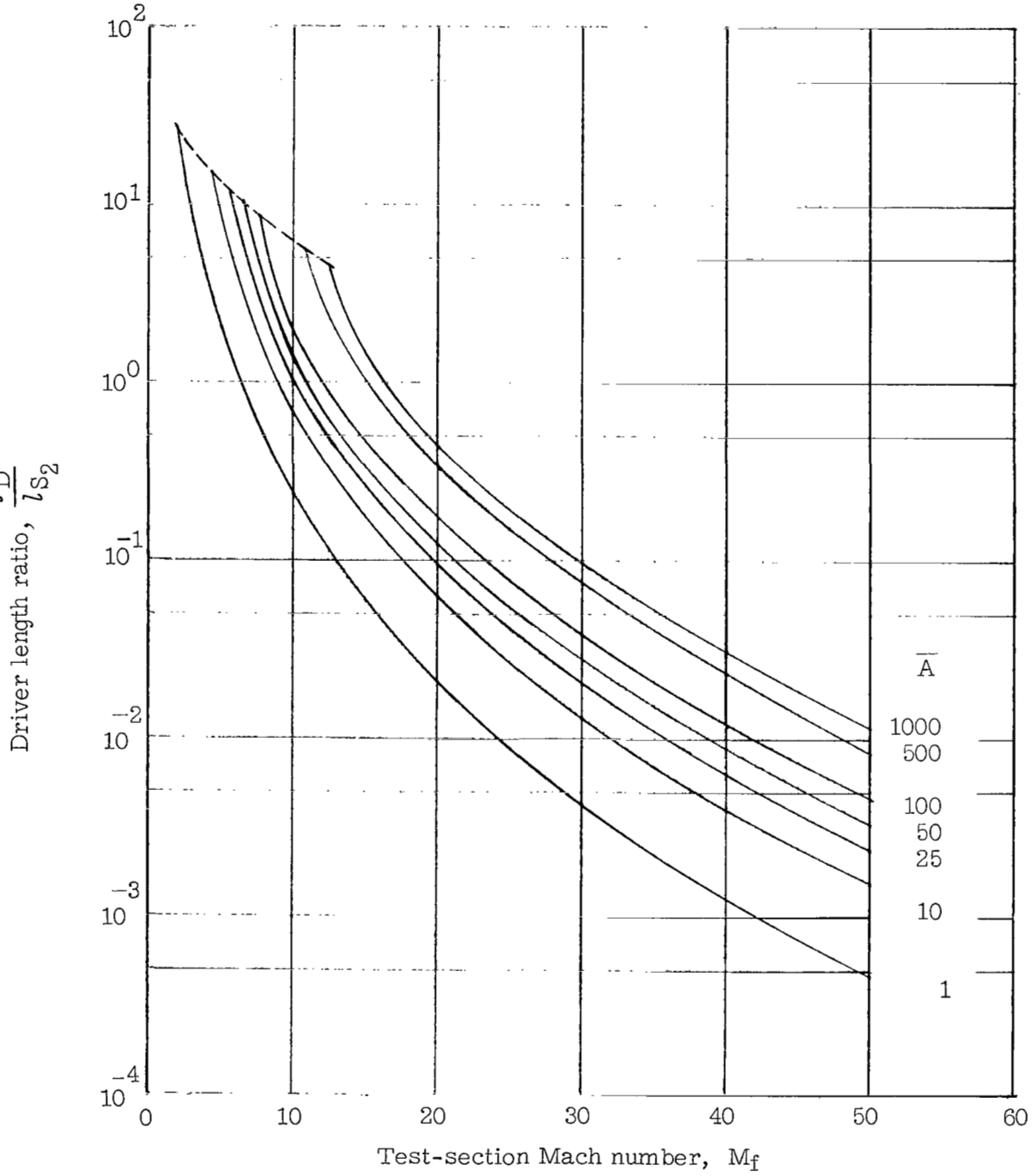

Figure 21. - Ratio of driver length to accelerating-chamber length for helium driver. $\gamma_4 = \frac{5}{3}$; $\frac{T_4}{T_f} = 25$.

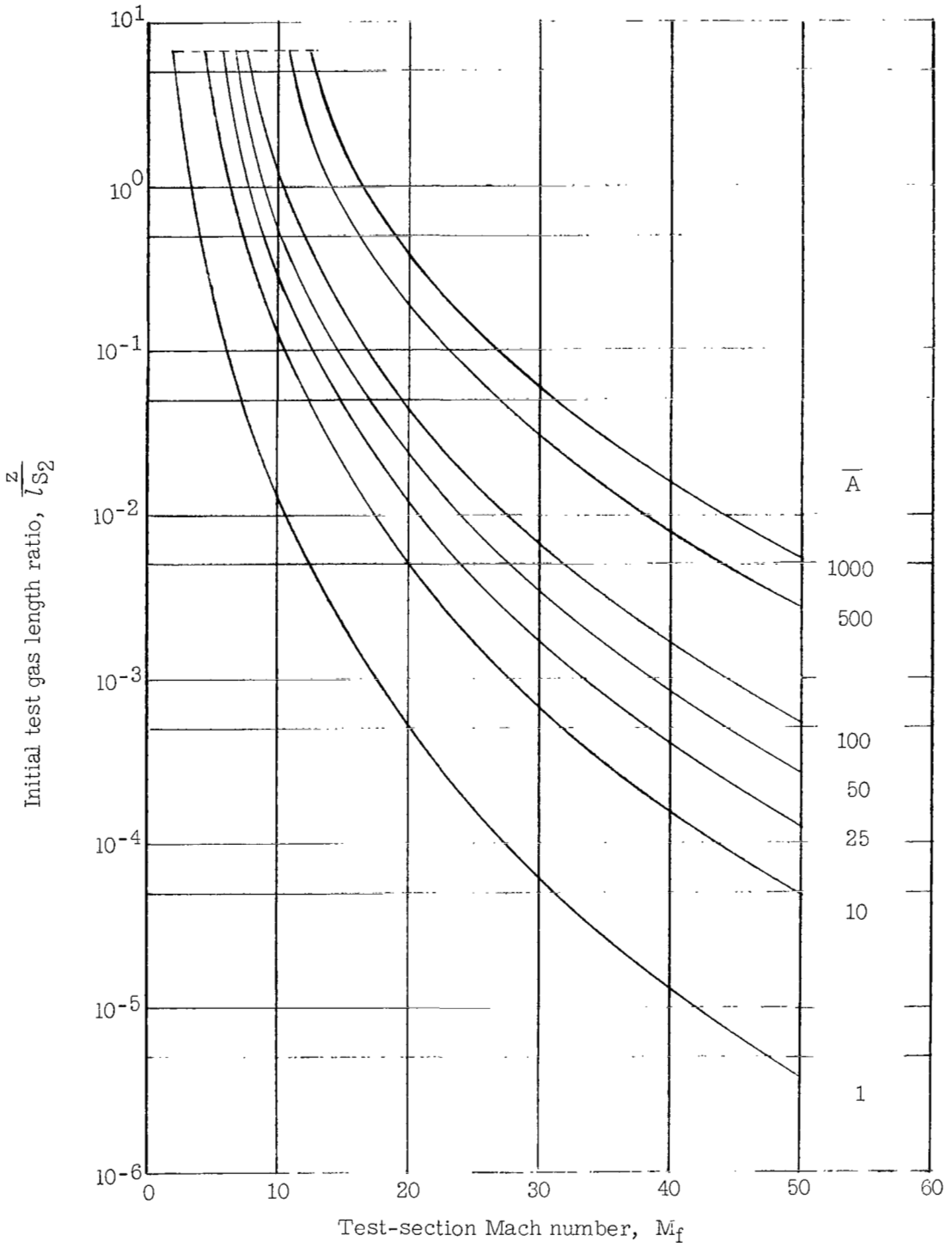

Figure 22. - Ratio of initial length of test gas slug to accelerating-chamber length. $l_N = 0$.

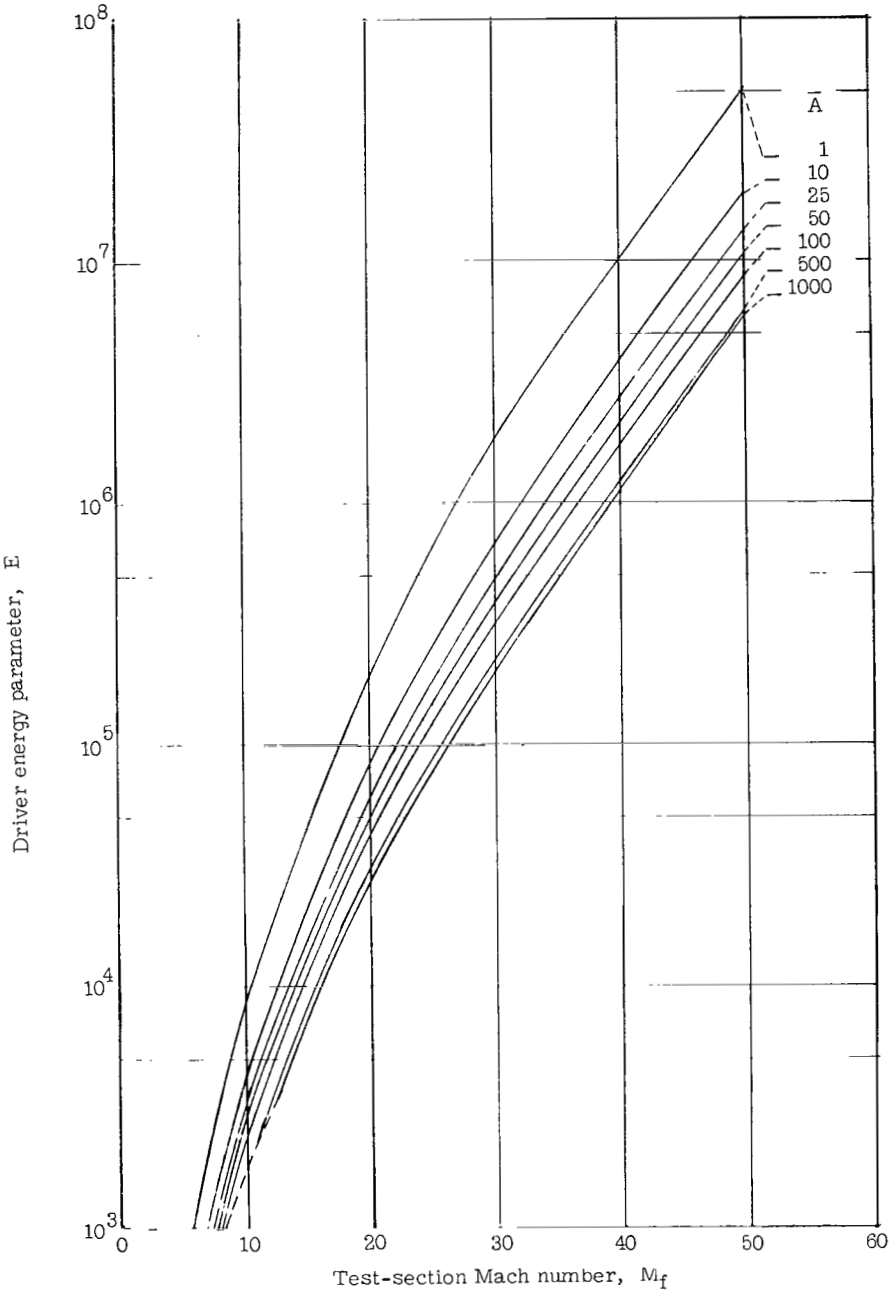

(a) $\frac{T_4}{T_f} = 10.$

Figure 23.- Variation of driver energy parameter with test-section Mach number for helium-driven expansion tunnels.

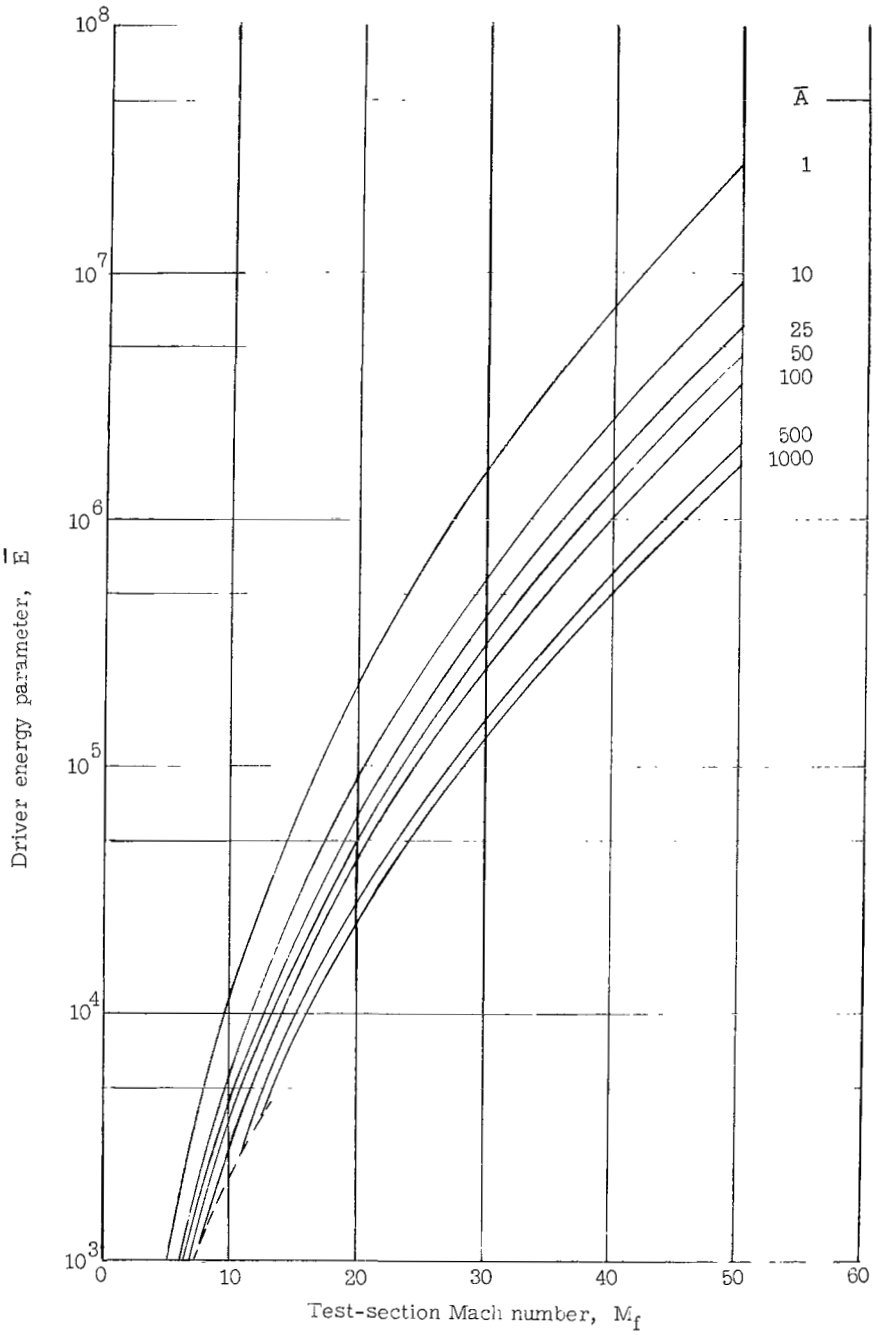

(b) $\frac{T_4}{T_f} = 25.$

Figure 23.- Continued.

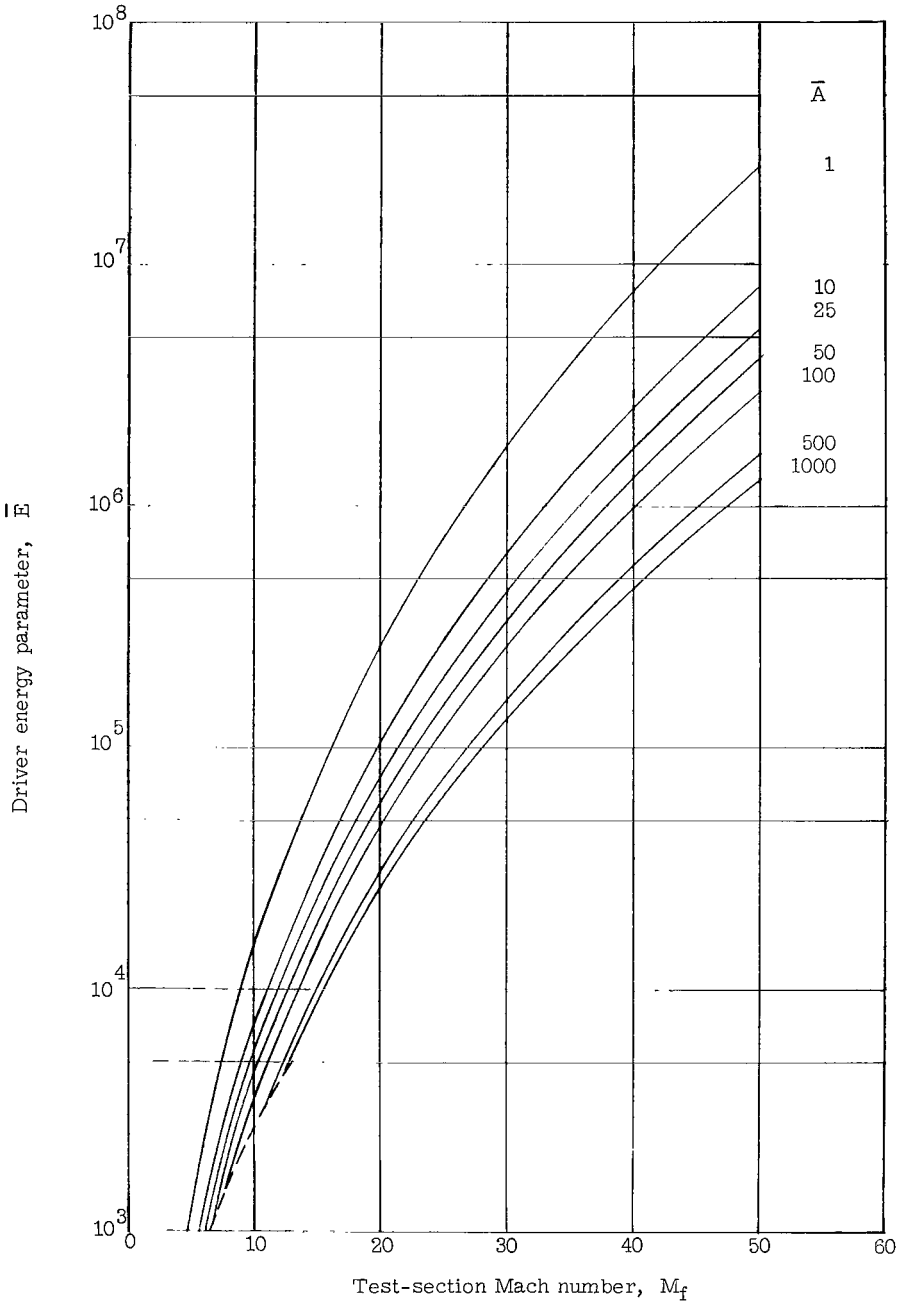

(c) $\frac{T_4}{T_f} = 50.$

Figure 23.- Concluded.

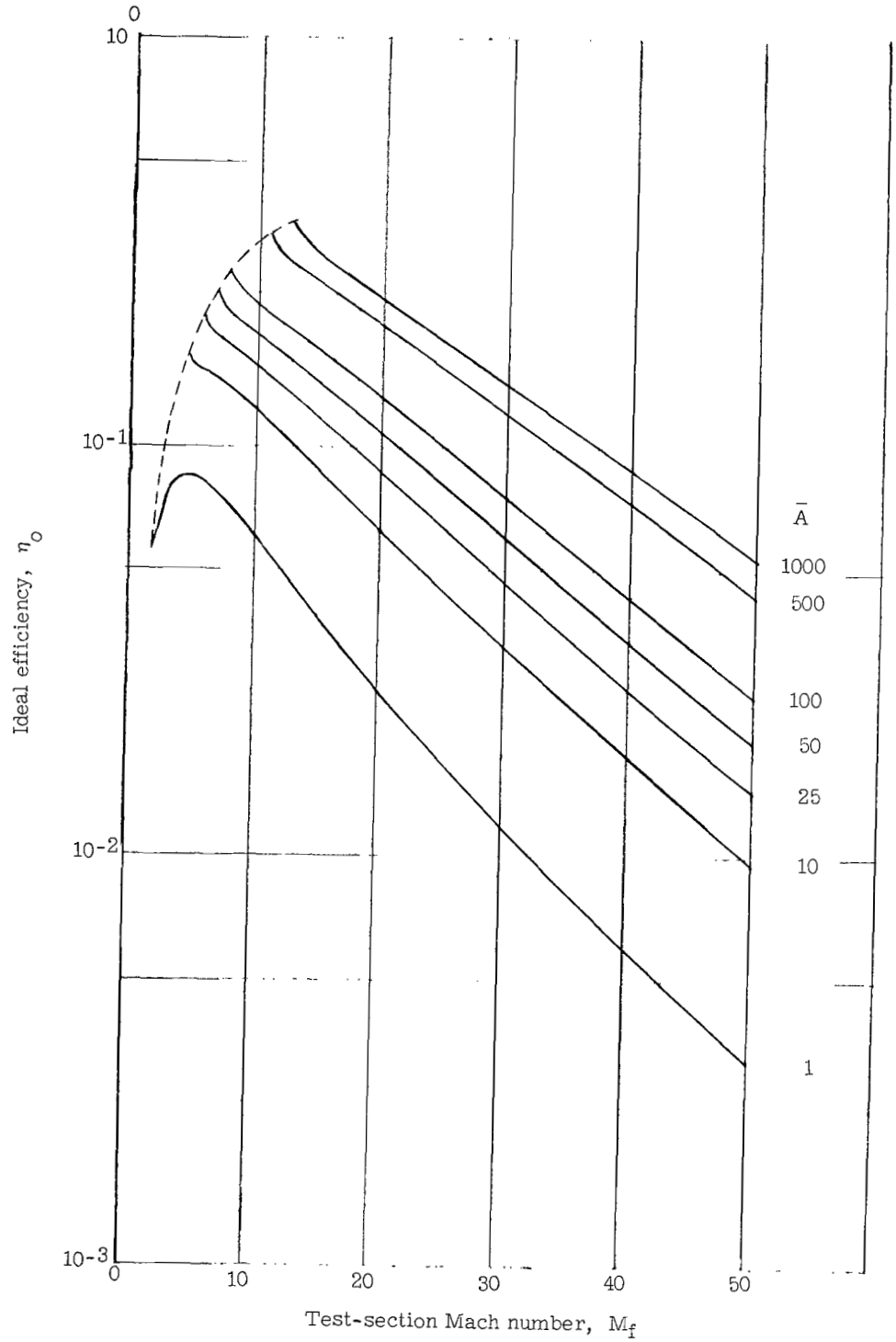

Figure 24.- Ideal efficiency of helium-driven expansion tunnels. $\frac{T_4}{T_f} = 25$.

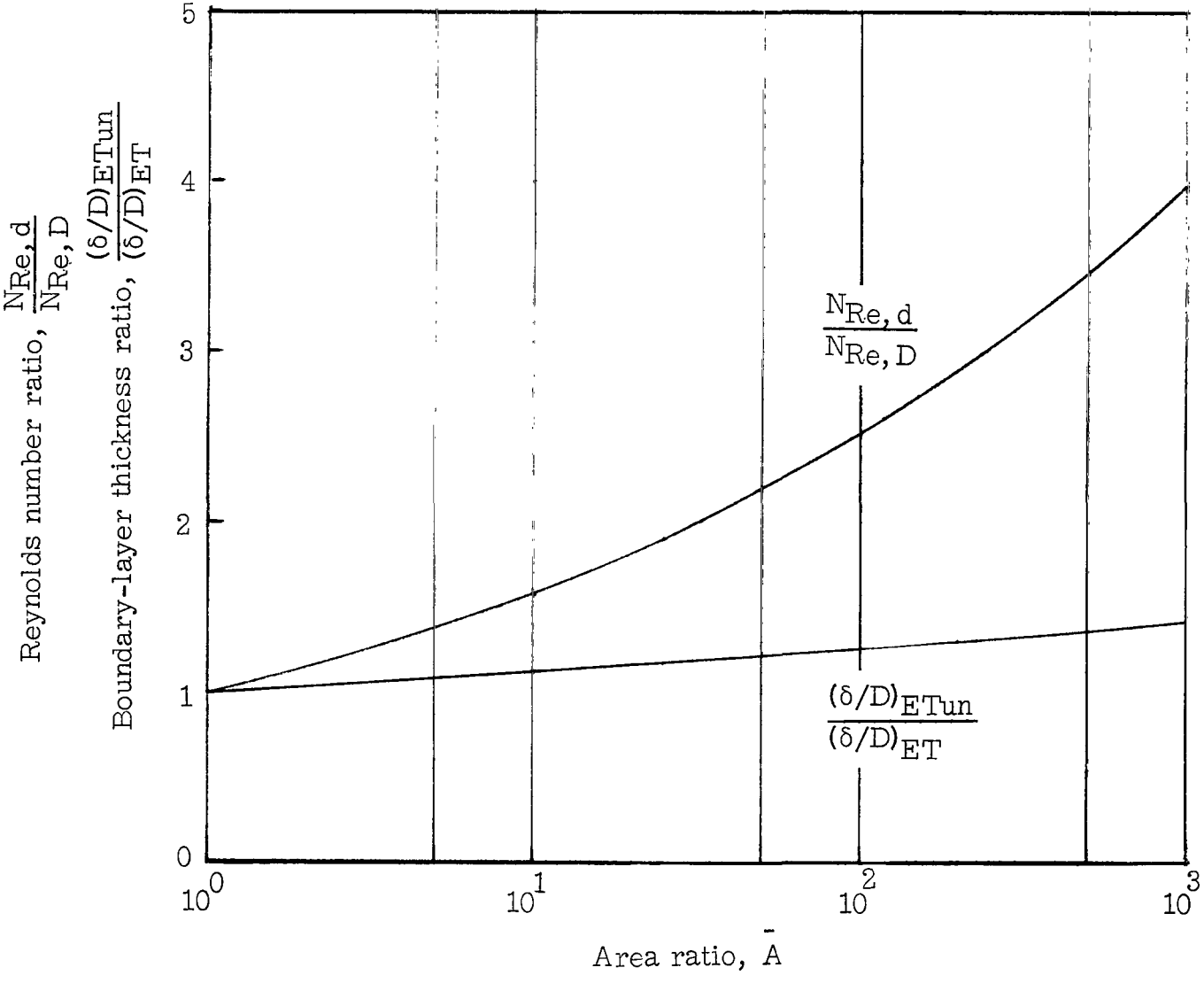

Figure 25. - Ratios of Reynolds numbers and nondimensional boundary-layer thicknesses in accelerating and test chambers for case d' = d.

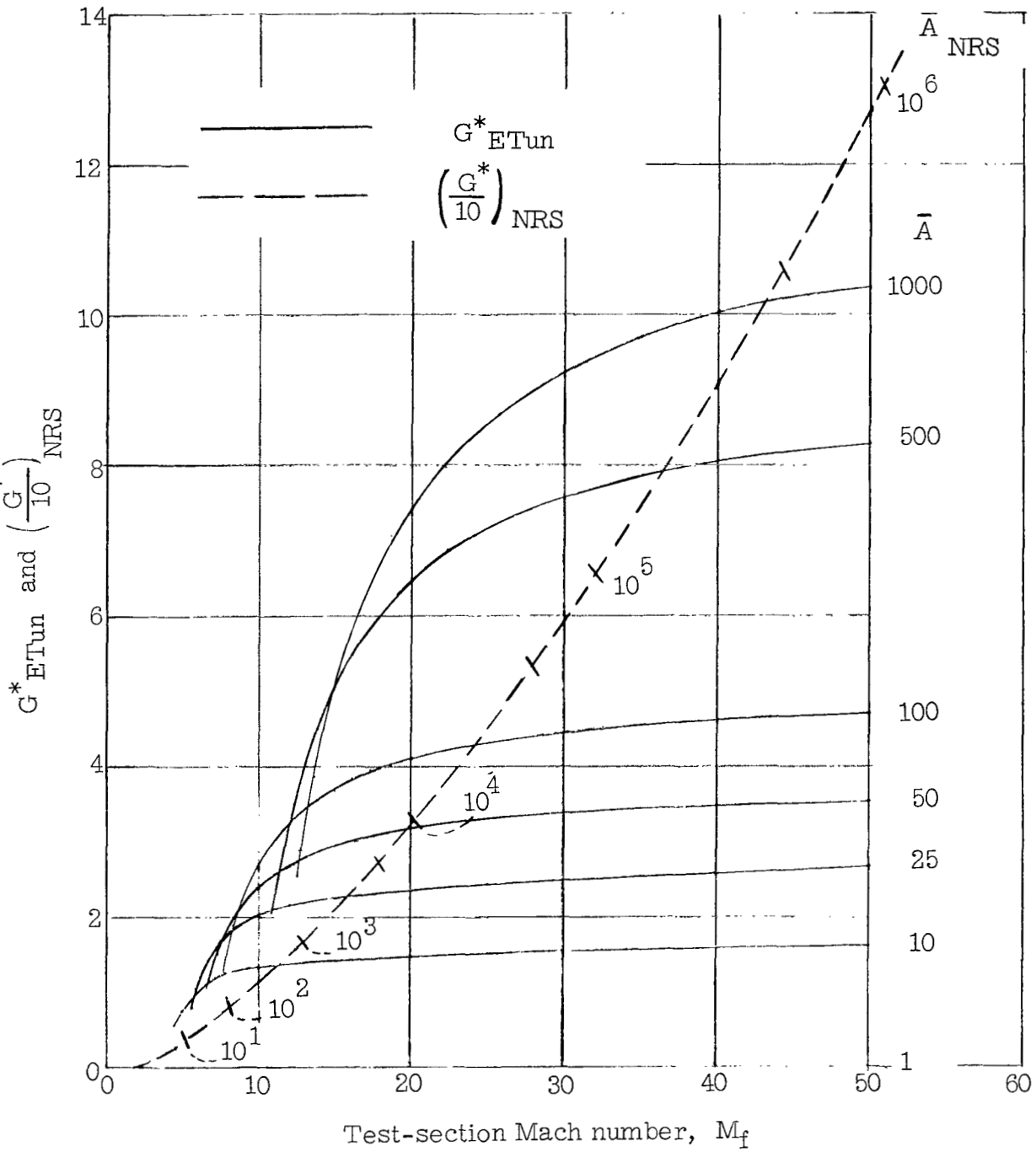

(a) With Mach number.

Figure 26.- Variation of values of parameter G^* for conical nozzles.

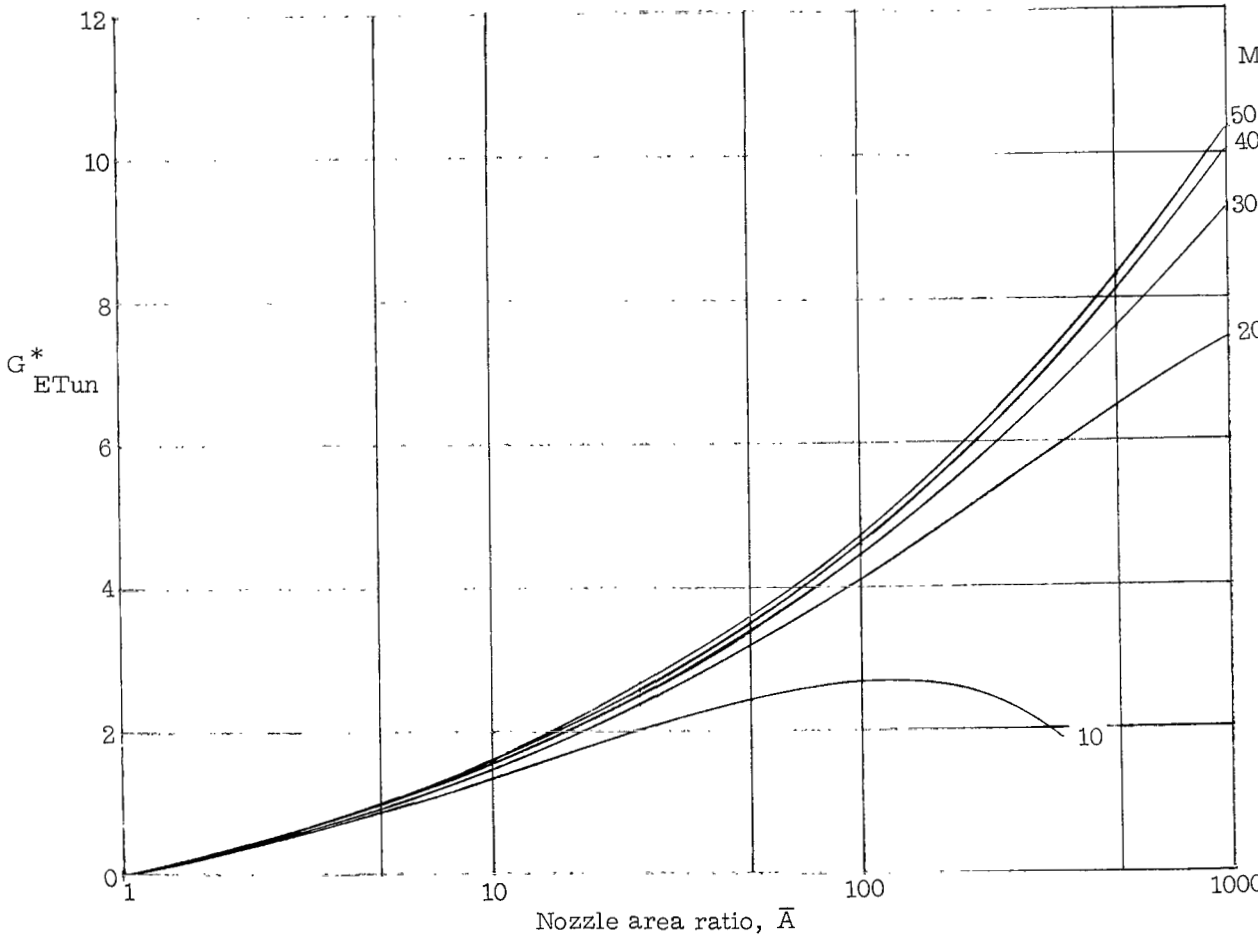

(b) With area ratio.

Figure 26.- Concluded.

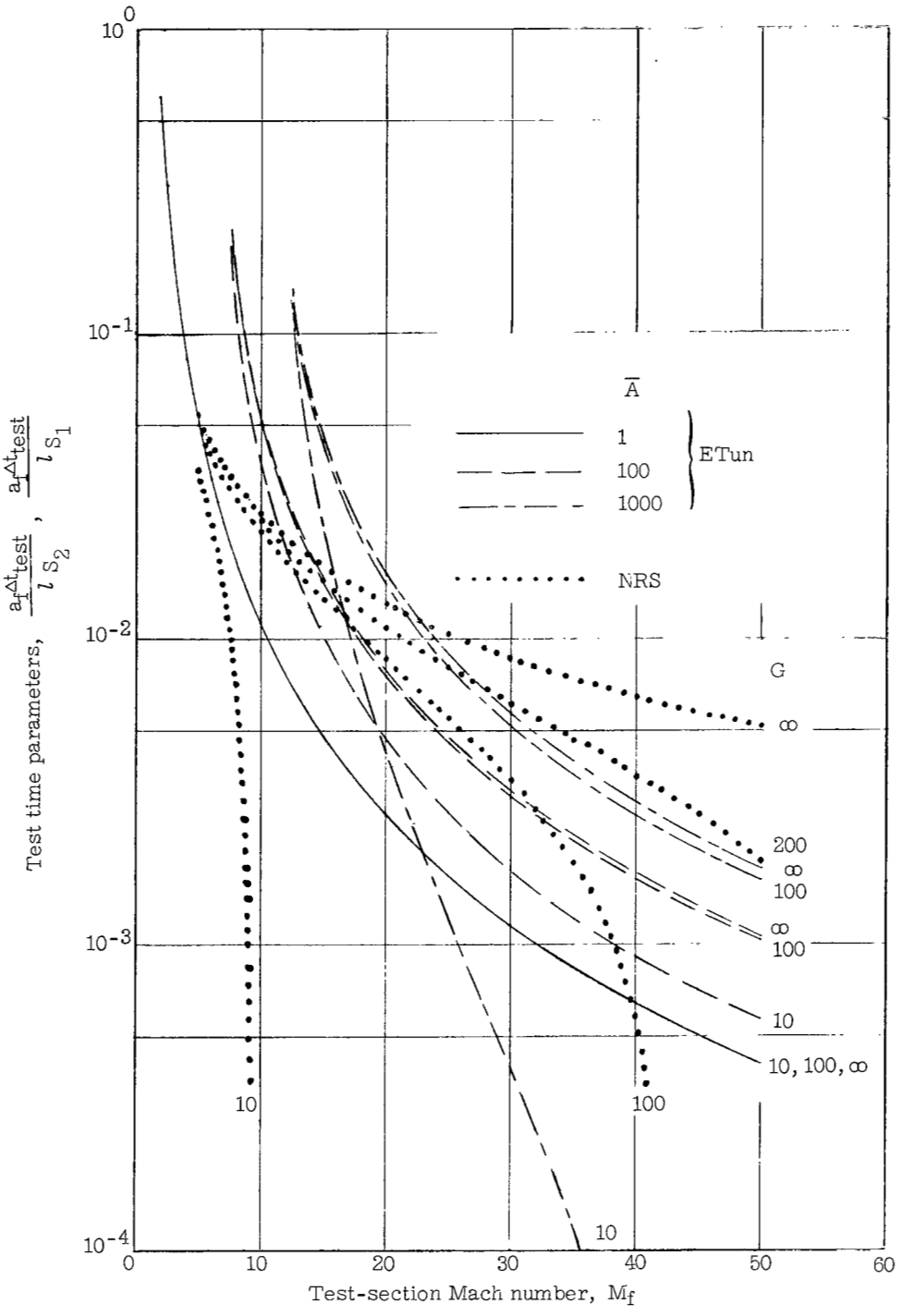

Figure 27.- Effect of G on test time parameter $\frac{a_f \Delta t_{test}}{l_S}$.

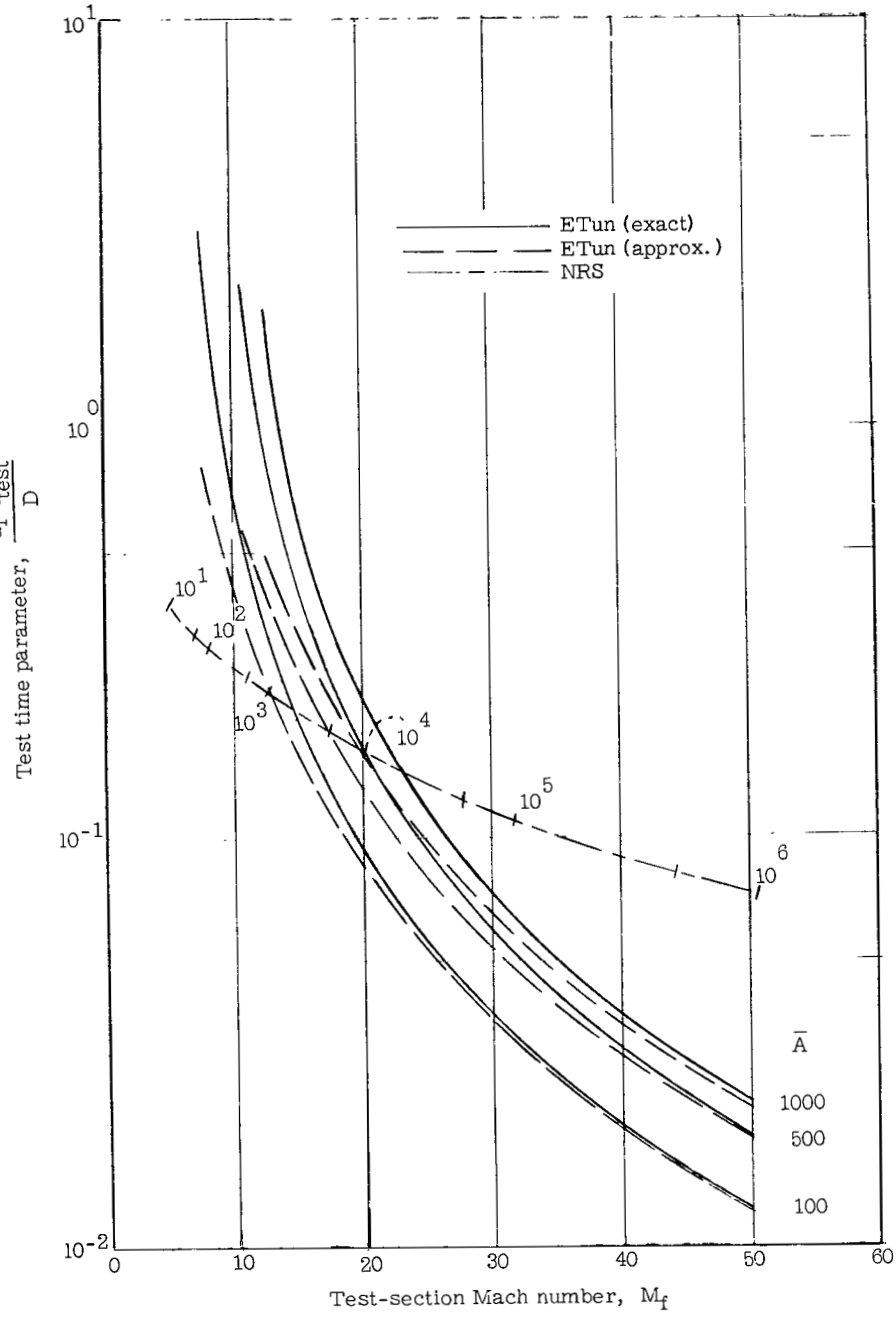

Figure 28.- Variation of test time parameter $\frac{a_f \Delta t_{test}}{D}$ with test-section Mach number for numerical example. Conical nozzle; $\frac{d}{D} = \frac{1}{10}$, $\frac{l_{S_2}}{d} = 150$; $G_o = 20$.

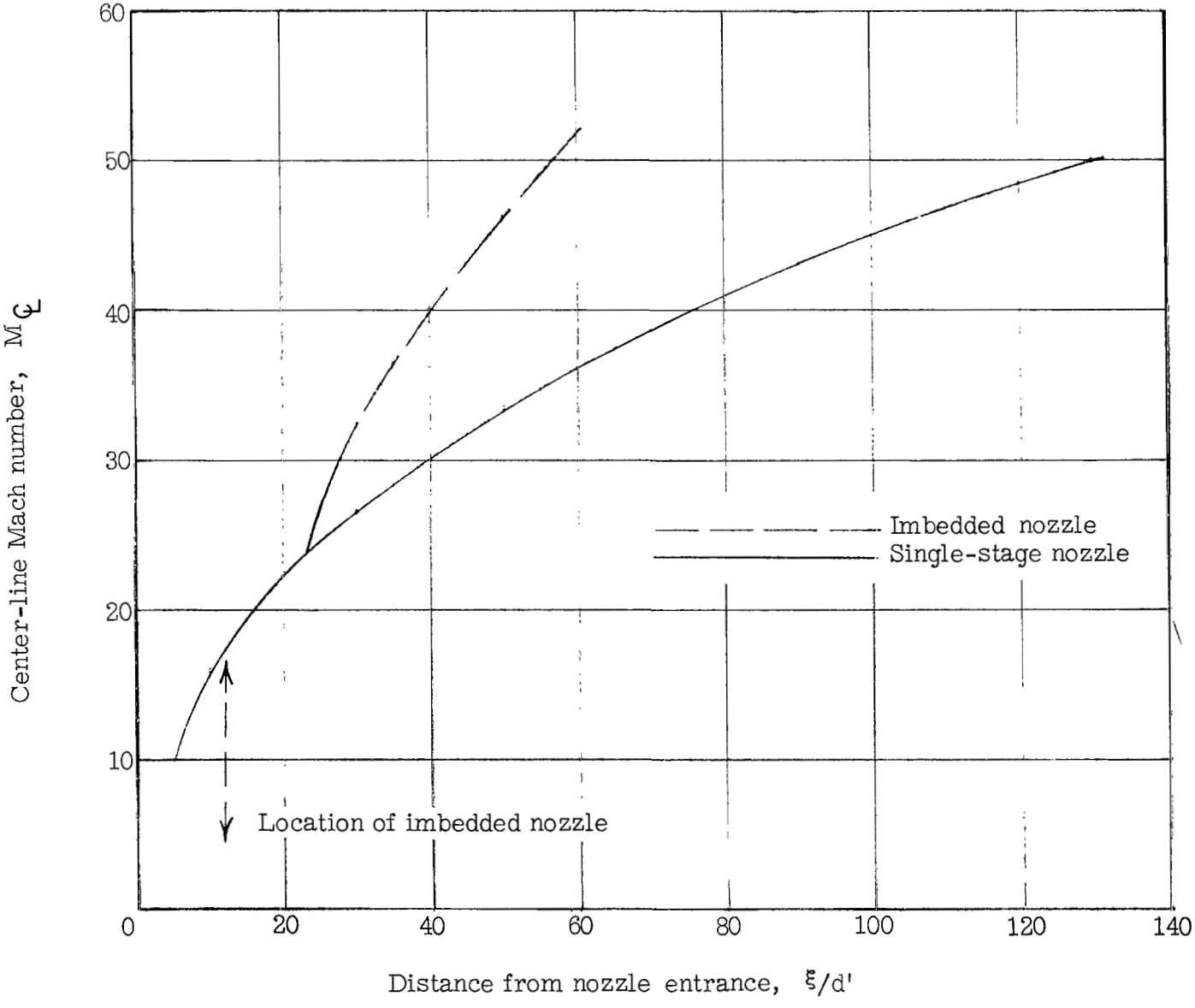

Figure 29.- Mach number variation along center line of simple conical nozzle and compound conical nozzle. $M_e = 10$; $\theta_w = 5.3^0$.

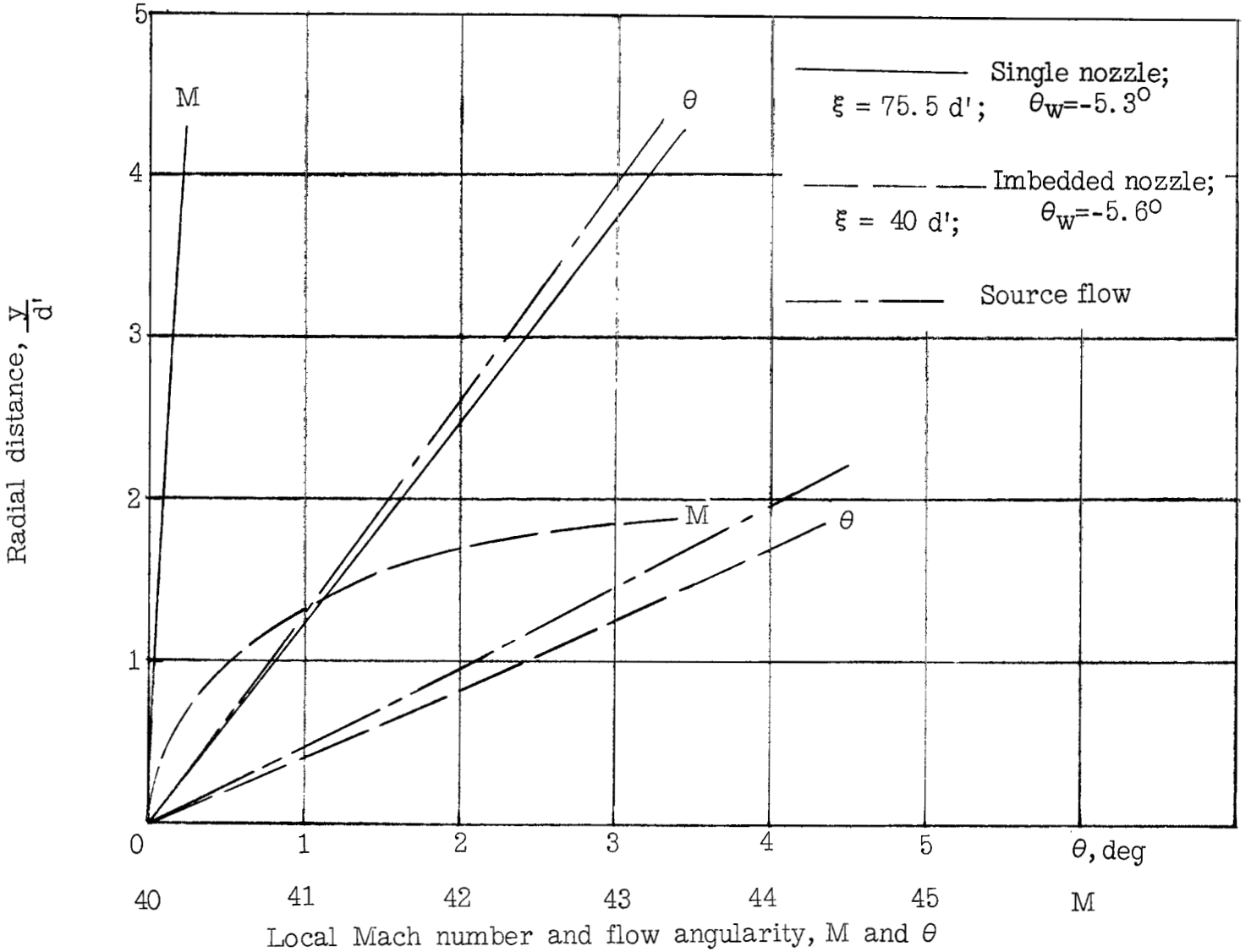

Figure 30.- Radial variation of flow Mach number and inclination.

"The aeronautical and space activities of the United States shall be conducted so as to contribute . . . to the expansion of human knowledge of phenomena in the atmosphere and space. The Administration shall provide for the widest practicable and appropriate dissemination of information concerning its activities and the results thereof."

—NATIONAL AERONAUTICS AND SPACE ACT OF 1958

NASA SCIENTIFIC AND TECHNICAL PUBLICATIONS

TECHNICAL REPORTS: Scientific and technical information considered important, complete, and a lasting contribution to existing knowledge.

TECHNICAL NOTES: Information less broad in scope but nevertheless of importance as a contribution to existing knowledge.

TECHNICAL MEMORANDUMS: Information receiving limited distribution because of preliminary data, security classification, or other reasons.

CONTRACTOR REPORTS: Technical information generated in connection with a NASA contract or grant and released under NASA auspices.

TECHNICAL TRANSLATIONS: Information published in a foreign language considered to merit NASA distribution in English.

TECHNICAL REPRINTS: Information derived from NASA activities and initially published in the form of journal articles.

SPECIAL PUBLICATIONS: Information derived from or of value to NASA activities but not necessarily reporting the results of individual NASA-programmed scientific efforts. Publications include conference proceedings, monographs, data compilations, handbooks, sourcebooks, and special bibliographies.

Details on the availability of these publications may be obtained from:

SCIENTIFIC AND TECHNICAL INFORMATION DIVISION

NATIONAL AERONAUTICS AND SPACE ADMINISTRATION

Washington, D.C. 20546